CHALMERS

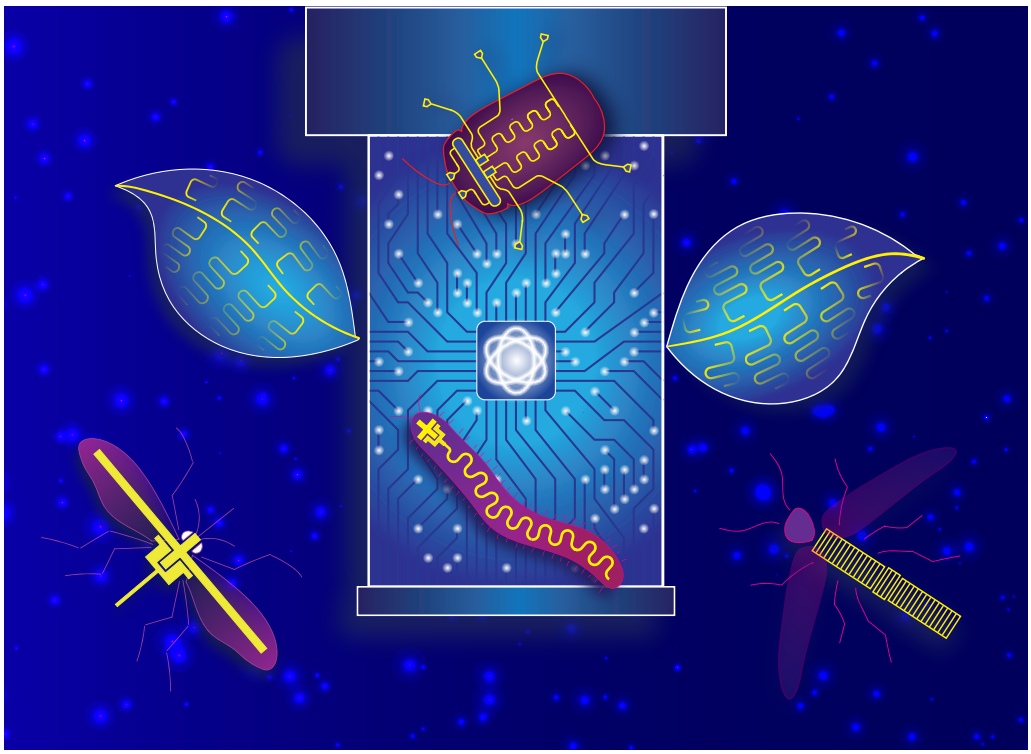

Effects of the environment on quantum systems

Decoherence, bound states and high impedance in superconducting circuits

MARCO SCIGLIUZZO

Department of Microtechnology and Nanoscience (MC2)
CHALMERS UNIVERSITY OF TECHNOLOGY
Göteborg, Sweden 2021

THESIS FOR THE DEGREE OF DOCTOR OF PHILOSOPHY

Effects of the environment on quantum systems

Decoherence, bound states and high impedance in superconducting circuits

MARCO SCIGLIUZZO

Quantum Technology Laboratory
Department of Microtechnology and Nanoscience (MC2)
CHALMERS UNIVERSITY OF TECHNOLOGY

Göteborg, Sweden 2021

Effects of the environment on quantum systems
Decoherence, bound states and high impedance in superconducting circuits
MARCO SCIGLIUZZO
ISBN 978-91-7905-534-9

Doktorsavhandlingar vid Chalmers tekniska högskola
Ny serie nr. 5001
ISSN 0346-718X

Quantum Technology Laboratory
Department of Microtechnology and Nanoscience (MC2)
Chalmers University of Technology
SE-412 96 Göteborg
Sweden
Telephone: +46 (0)31-772 1000

Cover:
Artistic interpretation of the environment incorporating the circuits studied in this thesis. Quantum insects and leaves (the circuits) that live and wander on a futuristic tree (the cryostat).

Chalmers Digitaltryck
Göteborg, Sweden 2021

Effects of the environment on quantum systems
Decoherence, bound states and high impedance in superconducting circuits
MARCO SCIGLIUZZO
Quantum Technology Laboratory
Department of Microtechnology and Nanoscience (MC2)
Chalmers University of Technology

Abstract

Superconducting circuits in the quantum regime represent a viable platform for microwave quantum optics, quantum simulations and quantum computing. In the last two decades, a large effort brought this architecture from an academic curiosity to concrete technology.

In this thesis, we study the effects of the environment on superconducting circuits. We consider mainly two types of the environments. On one hand, we study the classical baths inevitably coupled to the circuits, in particular the substrate where they are fabricated and the highly attenuated coaxial lines used for controlling them, which are the main sources for decoherence. On the other hand, we study structured electromagnetic environments that shape the density of states for the circuits, modifying their energy structure and their excitation properties.

Defects on the substrate mechanically and electrically coupled to superconducting circuits, behave as a bath of two-level systems. We investigate the effects of the bath on qubits fabricated on silicon. From a time trace with more than 2000 measurements of T1 and T2 (every 3 min for 60 h), we statistically infer a Lorentzian resonance signature of the bath. Moreover, measuring the residual population of the first excited state of the qubit, and tuning the photonic population in the line, we assess the thermal state of the bath, measuring a temperature of 42 mK. Furthermore, we investigate the mechanical coupling of the bath, saturating its state, strongly pumping neighbouring modes in a high finesse mechanical resonator. On a piezoelectric substrate, the travelling phonons, carry an electric component together with a lattice deformation. Therefore, superconducting circuits can be coupled to a phononic waveguide through which they release part of their energy. We design, fabricate and measure superconducting resonators on gallium arsenide, demonstrating the electromechanical coupling as the main source of decoherence.

Concentrating on the effects of the photonic bath in the coaxial line, we design a qubit with a very large coupling to this bath compared to the bath of two-level systems. In this limit, the scattering of a coherent photon by the qubit linearly depends on the photonic bath population. In this regime, the qubit can be used as a primary thermometer; we measured the photon occupation of our input lines both at different temperatures and injecting calibrated noise.

Finally, we implemented a slow-waveguide made of a linear chain of high impedance resonators. The excitation of two transmon qubits coupled to the waveguide is dressed with a photonic component, generating the hybrid excitation of an atom-photon bound state. We spectroscopically investigated the first and second excitation subspaces of the system, and we demonstrated full frequency and time domain control, of these bound states.

These results may help to improve the performance of superconducting circuits and their setups. Moreover, we hope that our experiments can provide tools for quantum thermodynamics, quantum simulation and quantum computing.

Keywords: circuit QED, superconducting circuits, quantum thermodynamics, atom photon bound state, surface acoustic wave, high impedance, two-level systems, TLS, SAW

List of publications

This thesis is based on the work contained in the following appended papers:

Paper A J. J. Burnett, A. Bengtsson, M. Scigliuzzo, D. Niepce, M. Kudra, P. Delsing, and J. Bylander, "Decoherence benchmarking of superconducting qubits", npj Quantum Information **5**, 54 (2019)

Paper B M. Scigliuzzo, L. E. Bruhat, A. Bengtsson, J. J. Burnett, A. F. Roudsari, and P. Delsing, "Phononic loss in superconducting resonators on piezoelectric substrates", New Journal of Physics **22**, 053027 (2020)

Paper C G. Andersson, A. L. O. Bilobran, M. Scigliuzzo, M. M. de Lima, J. H. Cole, and P. Delsing, "Acoustic spectral hole-burning in a two-level system ensemble", npj Quantum Information **7**, 1–5 (2021)

Paper D M. Scigliuzzo, A. Bengtsson, J.-C. Besse, A. Wallraff, P. Delsing, and S. Gasparinetti, "Primary thermometry of propagating microwaves in the quantum regime", Physical Review X **10**, 041054 (2020)

Paper E M. Scigliuzzo, A. Bengtsson, J. Burnett, S. Gasparinetti, and P. Delsing, "Measuring the temperature of a superconducting qubit and its surrounding two-level systems", To be submitted (2021)

Paper F M. Scigliuzzo, G. Calajò, F. Ciccarello, D. P. Lozano, A. Bengtsson, P. Scarlino, A. Wallraff, D. Chang, P. Delsing, and S. Gasparinetti, "Extensible quantum simulation architecture based on atom-photon bound states in an array of high-impedance resonators", arXiv:2107.06852 [quant-ph] (2021)

Other papers that are outside the scope of this thesis:

Paper I A. Osman, J. Simon, A. Bengtsson, S. Kosen, P. Krantz, D. P. Lozano, M. Scigliuzzo, P. Delsing, J. Bylander, and A. Fadavi Roudsari, "Simplified Josephson-junction fabrication process for reproducibly high-performance superconducting qubits", Applied Physics Letters **118**, 064002 (2021)

Paper II G. Andersson, S. W. Jolin, M. Scigliuzzo, R. Borgani, M. O. Tholén, D. B. Haviland, and P. Delsing, "Squeezing and correlations of multiple modes in a parametric acoustic cavity", arXiv:2007.05826 [quant-ph] (2020)

Paper III

Y. Lu, A. Bengtsson, J. J. Burnett, B. Suri, S. R. Sathyamoorthy, H. R. Nilsson, M. Scigliuzzo, J. Bylander, G. Johansson, and P. Delsing, "Quantum efficiency, purity and stability of a tunable, narrowband microwave single-photon source", arXiv:2105.11234 [quant-ph] (2021)

Contents

To my father,
who taught me Science (and science fiction) before anyone else
A mio papà,
che mi ha insegnato la Scienza (e la fantascienza) prima di tutti

Acknowledgements

I remember how happy I was when my supervisor, Per, invited me here for an interview and later offered me the PhD position. I want to thank him for believing in me and giving me the possibility to add my contributions to this field (and also for reading my thesis during his vacation, not everyone would have done that). A particular thanks to my co-supervisor Simone, who showed me the importance of the professional way in doing even the smallest tasks. I really enjoyed the physics discussions with my examiner, Avgust, and, in the same spirit, I greatly appreciated Andreas B and Laure's help, showing me how to collect data methodically and write down everything I did. At the same time, I am grateful to Pasquale and Gabriele, both for the cool time when we were undergrads in Lecce and for the academic discussions we keep having now. I would also like to thank all my co-authors, Andreas W, Darrick, Francesco, Giuseppe and Jean-Claude for their help and valuable feedback. A special thanks to my opponent, prof. Johannes Fink, that accepted to examine my thesis and read my articles. I hope you found them interesting.

The second hardest time during my PhD was at the beginning, so I am happy I started together with Jonathan, Anita and Yong. We all find our path, in a way or another, also thanks to the guidance of the "senior" ones, Thomas, Bala, David, Gustav, Ida Maria and Ben. At the same time, I am grateful to my friends Sobhan and Hans, for helping me navigate through MC2 first and the "Swedish way" later. And thanks to Marina and EdUardo for all the trips, hiking, night games, dog walking, and a (very short) cycling experiment.

I was lucky to meet many scientists during my PhD with whom I could exchange ideas and experiences: thanks Amr, Chris, Christian, Daniel, Daryoush, Giovanna, Janka, Marti, Miroslav, Sandoko, Selim, Sushanth. I am grateful to Thilo, Witlef, Dag, Serguei and Jonas for trusting me with laboratories or exercise sessions for master and bachelor courses. I was also happy to transfer a bit of knowledge to Aamir, Clair and Claudia almost at the end of my PhD. Thank you for paying attention to what I had to say or show. I really enjoyed my time initially at QDP and then QT. Thanks to all friends and colleagues that make a pleasant experience to spend the week (and the weekend) at work. And thanks to the staff for maintaining the best Cleanroom I have used, in particular Marcus, Niclas and Johan for the EBL and laser writer tips. Finally, all the measurements I did would have not been possible without having a place where to bond the samples: thanks Lars, for realizing all strange cryogenic pieces or sample holders I came up with!

Even if we tend to forget it, we are people before scientists. I express my gratitude to my friends for reminding me of it! In particular Isabel, Andrea and Cecilia, Pierpaolo and Silvia. The same is true for all my friends from Massaglia (hopefully I will get in shape for the Spartan in three months) and from ISUFI. I apologize if I did not mention all of you directly, or if I missed some colleagues. The list would probably go on for many pages.

I have to admit that I would not have been able to be here, without the constant support of my parents, that have always tried to satisfy my interests in science, with books, experiment kits for children and tickets for travels and museums. And the cover of this thesis will literally not be so cool without my brother. Thank you.

Before concluding, I admit I have a large debt with Sweden; not only I had the possibility to work in a competitive (and expensive to run) field that I love, but also I

found Zozan. Thank you, for the constant help in my last three years of PhD, for not getting angry when I came home late and left early, for not being mad when I did not fix stuff I said I would, and many many other things. You know how hard it was and I am glad we can celebrate this achievement as ours.

Marco Scigliuzzo, Göteborg, August 2021

Abbreviations

SQUID	Superconducting quantum interference device
cQED	Circuit quantum electrodynamics
cQAD	Circuit quantum acoustodynamics
CPW	Coplanar waveguide
TLS	Two-level system

Constants

$e = 1.6 \cdot 10^{-19}\,\mathrm{C}$	Electron charge
$\hbar = 1.054 \cdot 10^{-34}\,\mathrm{Kg\,m^2/s}$	Reduced Planck constant
$k_\mathrm{B} = 1.38 \cdot 10^{-23}\,\mathrm{m^2\,kg/\,s^2\,K}$	Boltzmann constant
$c = 2.998 \cdot 10^{8}\,\mathrm{m/s}$	Speed of light
$\alpha \approx 1/137$	Fine structure constant

Superconductivity

ϕ	Phase difference across Josephson junction
I_c	Critical current of a Josephson junction
Φ	Magnetic flux
Φ_0	Magnetic flux quantum

Resonator parameters

S_{11}	Reflection coefficient
S_{21}	Transmission coefficient
Z_0	Characteristic impedance of the transmission line
v_p	Phase velocity
v_g	Group velocity
d	Lattice constant in distributed waveguides
k_n	Wave number of mode n
ω_r	Resonator fundamental frequency
ω_n	Resonant frequency of mode n
Q	Total quality factor
κ	Total resonator-waveguide rate
κ_r	Radiative coupling
κ_nr	Non-radiative rate
n_c	Critical photon number
δ_t	TLS loss tangent
J	Inter-cavity coupling

Qubit parameters

E_J	Josephson energy
E_C	Charging energy
ω_q	Qubit frequency
ω_{BS}	Bound state frequency
Δ	Qubit–resonator detuning
g	Qubit–resonator coupling
$\hat{H}$	Hamiltonian
$\hat{b}$	Bosonic annihilation operator
$\hat{\sigma}_{x,y,z}$	Pauli X, Y, and Z operators
$\hat{\sigma}^{\pm}$	Raising and lowering operators for the qubit
$\lvert g, e, f, ...\rangle$	ground, first excited, second excited, ... qubit levels
χ	Dispersive shift
T_1	Qubit relaxation time
γ	Qubit relaxation rate
T_ϕ	Dephasing time
T_2	Coherence time
T_2^*	Free-induction decay (Ramsey) time

Other

T	Temperature
ω	Angular frequency
V	Voltage
I	Current

Thesis

–Do you guys just put the word "quantum" in front of everything?

Ant-Man and the Wasp, Marvel Studios (2018)

1

Circuit quantum electro- and acousto-dynamics

In a bit more than a century, human kind went from ignoring the existence of quantum systems to building and controlling an artificial molecule of 53 artificial atoms, rearranging and exciting its energy levels, fast enough to use the molecule dynamics to accomplish a calculation[1]. Physicist invented quantum mechanics at the beginning of the 20^{th} century, to have a theory that reproduces experimental observations regarding **light-matter interaction**. In particular the electromagnetic spectrum of black body radiation and the emission of the electrons from a metal irradiated with light. In these cases, the systems are macroscopic and warm[1], still the quantum nature of its constituent qualitatively changes the behavior of the system.

Refining experimental techniques and inventing new technologies, allowed to examine smaller and smaller systems, and, at the same time, colder and colder. More formally, reducing the dimensions of the system, decreases its degrees of freedom, while cooling it down limits the external thermal energy and make it possible to reach the ground state of the system. This control led us to unravel the intrinsic quantum mechanical behavior on a single atom scale. But also to discover new effects unexplained by classical physics. For example, certain materials, below a critical temperature, T_c, retain only a single degree of freedom, even for a macroscopic ensemble[2]. Besides the scientific progress, this knowledge boosted a new technological era (usually referred as first quantum revolution)

[1] Large and small do not have a defined meaning, if not taken with a reference. In this thesis macroscopic means a system with many ($\gg 1$) free degrees of freedom. The same is true for hot and cold: they will be used with the reference of a single quantum of energy at the frequency of interest.

[2] H. K. Onnes noticed the resistance drop of quicksilver while cooling it down in liquid helium. Remarkably, he continued to decrease the temperature, observing the helium stop boiling, discovering two examples of this phenomenon, superconductivity and superfluidity in the same day in the same experiment [2]

with the invention tools and devices (for example lasers and transistors) that strongly shaped our society.

A new avenue was opened when we learned how to manipulate individual quantum systems. Initially, the effort in **quantum optics** concentrated on the light-matter interaction of single natural atoms and visible light, achieving exceptional results. Scientists discovered that confining an atom or light between two mirrors, drastically changes the light-matter interaction [3, 4]. This is an example of the effects of the (electromagnetic) environment on the atom: the confinement amplifies the zero-point fluctuations at the cavity resonant frequency, while it attenuates the possible relaxation into forbidden modes. Remarkably, with the invention of artificial superconducting atoms, researchers are able to reproduce this experiment in a different energy regime [5]. In this new field, named circuit quantum electro-dynamic, or **cQED** for short, the atomic transition frequencies and the interaction strengths can be engineered to cover a large portion of the microwave spectrum. Even the atoms dimensions can span the range from deep sub-wavelength to many wavelengths, simply by design choice.

This thesis, entitled "Effects of the environment on quantum systems", enters at this point of the story. The title is easily explained in the scope of cQED: the quantum systems consist of superconductive circuits, cooled down at their quantum-mechanical ground state. They are implemented with transmon qubits, with fermionic degrees of freedom, $\hat{\sigma}_i$, and/or linear and nonlinear resonators, with bosonic degrees of freedom, $\hat{b}$. We call **environment** all the remaining degrees of freedom that have any sort of interaction (i.e. can exchange energy, affect the energy levels) with the system, but are not of particular interest. As clear from this definition, the separation between environment and quantum system is arbitrary, and mainly rely on the focus to some degrees of freedom instead of others. In the thesis, we mainly study two effects of the environment on the quantum system:

- the coupling of the a resonator mode or a qubit with a very large number of degrees of freedom (a bath) that produces an effective drive due to its noise spectral density (chapter 2);
- the coupling of multiple qubits with a nontrivial density of states, that effectively modify transition frequencies and relaxation rates (chapter 3);

This chapter contains an overview of the different systems that have been studied in the thesis, their properties and the general use in cQED.

1.1 Introduction and motivation

Circuit QED focuses on light-matter interaction in the microwave regime, replacing natural atoms with superconducting circuits operating in the microwave regime[3]. These circuits are man-made macroscopic objects composed of many particles and coupled to

[3]The most used frequencies range from 1 to 10 GHz, corresponding to wavelength from 30 to 3 cm in vacuum. Moreover the circuits are usually realized with standard lithography process. Therefore, very fortunately, this field can use many instruments developed for telecommunications and many techniques used for semiconductor processing

many different baths (photons through driving lines, phonons mechanically coupled to the sample box where they are placed, defects on the substrate where they are fabricated). In order to have a system with only few controllable degrees of freedom, we need to get rid of the unwanted and be able to control and read-out their state at any time. In circuit QED we satisfy all these requirements:

- using superconductors we can choose to keep only the degrees of freedom we design in the system;
- using a dilution refrigerator and highly attenuated input lines, we isolate these degrees of freedom from the baths;
- by engineering the circuit levels structure, we make these degrees of freedom more resilient to the environment fluctuations.

1.1.1 Superconductivity and Josephson effect

The electrons in a metal in a superconducting state exhibit an effective phonon-mediated coupling, and consequently form bound states of electrons pairs (Cooper pairs). All the Cooper pairs condense to the ground state and become the effective current carrier [6]. This state can be described by a complex wavefunction $\psi_s = \sqrt{n_s}e^{i\theta}$, where n_s is the Cooper pair density while θ is the phase of the superconducting condensate. There are mainly two reasons to chose superconductors: firstly, the superconductors have very low resistance at the microwave frequencies compared with normal metals[4] (and none with direct currents! [7]), making the restive losses effectively negligible compared to the intrinsic loss due to defects of impurities in the substrate [8]. Secondly, and most importantly, the presence of the Josephson effect that describes the Cooper pair tunneling between two superconductors [9]. Exploiting this effect we can realize a nonlinear inductor, the **Josephson Junction** (JJ), that effectively lets the circuits access the quantum regime. In fact, a purely linear component driven with coherent signals, can be completely described classically [10].

When two superconductors are separated by a thin tunnel or oxide barrier, compared with the coherence length of the superconducting state[5], Cooper pairs can tunnel between the two electrodes without any voltage across them. Josephson discovered that this is true up to a critical current, I_c, and that the tunneling current, I_J directly relates to the phase difference of the two superconductors $\phi = \theta_1 - \theta_2$, Eq. (1.1). If ϕ is not constant in time, a voltage, V, proportional to the phase derivative is built up across the junction, Eq. (1.2).

$$I_J = I_c \sin\phi, \tag{1.1}$$

$$\partial_t \phi = \frac{2e}{\hbar} V. \tag{1.2}$$

[4] Even below the transition temperature T_c, there is a nonzero components of unbound Cooper pair, quasi particles, responsible for this effect and for the kinetic inductance.

[5] The coherence length is the exponential decay constant of ϕ_s outside the superconductor. For example in aluminum is 1.6 μm [6].

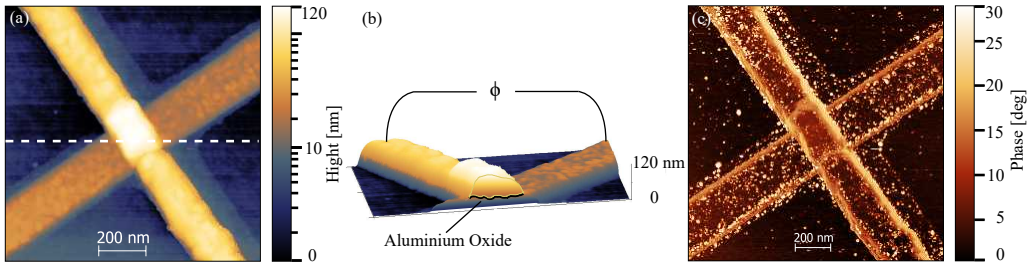

Figure 1.1: *Atom Force Microscopy (AFM) micrographs of a Josephson Junction (JJ). (a) Hight detected for a* $1.1 \times 1.1\,\mu\text{m}^2$ *scan of an aluminum JJ on gallium arsenide. (b) Three dimensional rendering of a the data in (a) with a longitudinal cut in correspondence of the white dashed line in (a). A cartoon of the aluminum oxide layer is depicted in black. The phase* ϕ *refers to the phase difference between the two superconductor electrodes. (c) AFM oscillation phase for the same range of data shown in (a). Phase changes highlight mechanical properties changes, that are due to different materials, most likely resist residues. Notice how this information is completely invisible to the hight sensor in (a), or to Scan Electron microscopy in Fig. 1.2.*

In this thesis, we realize JJs by evaporating a layer of aluminum, letting an oxide layer ($\sim 2\,\text{nm}$) grow in an oxygen atmosphere and completing the sandwich with an additional layer of aluminum, as shown in Fig. 1.1. The junctions fabricated for the devices in this thesis have a square form factor and dimensions ranging from 100×100 to $350 \times 350\,\text{nm}^2$, yielding critical currents between 30 and 300 nA. As we show in **Paper I**, the JJs have a critical current scattering, $\sigma_{Ic} \approx 3\%$, from the design target. This is one important difference between quantum optics implemented in cQED compared to natural quantum systems: while natural atoms are completely identical[6], the quantum systems we fabricate are not exactly identical and their properties may even change with time.

Substituting Eq. (1.2) in the time derivative of Eq. (1.1),

$$\partial_t I_\text{J} = \frac{2e}{\hbar} I_\text{c} \sqrt{1 - \left(\frac{I_\text{J}}{I_\text{c}}\right)^2}\, V, \tag{1.3}$$

and considering the analog voltage drop $V = L\partial_t I$ across an inductance L, we conclude that a JJ behaves as an inductance:

$$L = \frac{\hbar}{2eI_\text{c}} \frac{1}{\sqrt{1 - \left(\frac{I_\text{J}}{I_\text{c}}\right)^2}} \overset{I_\text{J} \ll I_\text{c}}{\approx} L_\text{J} \left(1 + \frac{1}{2}\left(\frac{I_\text{J}}{I_\text{c}}\right)^2\right). \tag{1.4}$$

where $L_\text{J} = \hbar/2eI_\text{c}$. This Josephson inductance is not constant, but increases with the current circulating through it. Therefore the Josephson inductance can be both nonlinear

[6] This is a direct consequence of quantum field theory: elementary particles are an excitation of their field counterpart, so they all are exactly the same, as in cQED all photons in a linear resonator are exactly the same.

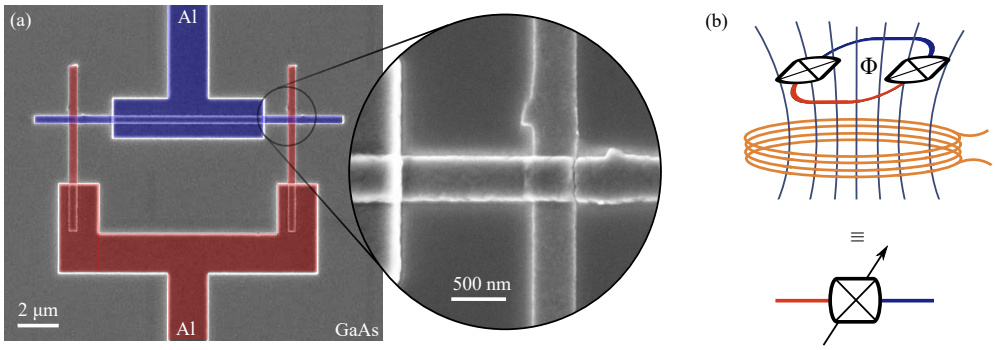

Figure 1.2: *Superconducting QUantum Interference Device (SQUID). (a) Scanning electron microscopy micrograph of an aluminum SQUID (colors) on gallium arsenide (grey). Two junctions in parallel shunts two superconductors electrodes (blue and red). In the zoom one of the two Josephson junctions. (b) A SQUID behaves as a Josephson junction with a tunable critical current, depending on the external magnetic flux in the SQUID loop.*

and parametric. The values of L_J for the junctions fabricated in our experiment goes from 1 nH (for $300 \times 300\,\mathrm{nm}^2$) to 10 nH (for $100 \times 100\,\mathrm{nm}^2$).

Remarkably, when two identical JJs with critical currents I_c, shunt two superconducting electrodes, as shown in Fig. 1.2, they behave as a single junction with an effective critical current I_{SQUID}. Moreover, an external magnetic flux Φ that threads the SQUID loop, induces a supercurrent in the loop[7] and modulates the effective critical current,

$$I_{SQUID} = 2I_c \left| \cos\left(\frac{\pi\Phi}{\Phi_0}\right) \right|, \tag{1.5}$$

where $\Phi_0 = h/2e = 2.068 \cdot 10^{-15}$ Wb is a magnetic flux quantum.

The area of the squid loops fabricated in this thesis (see Fig. 1.2) is on the order of $50\,\mu\mathrm{m}^2$, so we inject a flux quantum with magnetic field of 0.5 Gauss, usually generated with a fluxline or a superconducting coil. The fact that this field is the same of the Earth's magnetic field shows how sensitive the SQUIDs are, and how important it is to have the proper magnetic shielding around the sample (see appendix A).

1.1.2 From classical to quantum microwave circuits

A JJ is a perfect candidate for building a quantum system. In fact, considering two isolated electrodes the total number of Cooper pairs, given by the sum of the ones in each lead, $N_{cp} = N_{cp1} + N_{cp2}$, is constant. We then keep a single degree of freedom, given by the excess Cooper pairs $n_{ex} = (N_{cp2} - N_{cp1})/2$, that arises when a tunneling event happens.

[7] The time necessary to build up the currents is much faster than our instruments, so in this thesis we will consider this change as instantaneous.

Experimentally we need to answer if, in this circuits, a "macroscopic variables obey quantum mechanics". Martinis, Devoret and Clarke positively replied to this question [11], directly exciting and measuring the levels decay rate in a current bias JJ, and starting de facto circuit QED. More than a decade later, Devoret's group exploited the capacitance of a SQUID, as a box where the excess Cooper pairs were stored, obtaining a resonant circuit with transitions in the microwave regime, named Cooper pair box [12]. In the following few years, Nakamura et al. [13] drove oscillations in this quantum circuit while the Cooper pair box relaxation time was measured by Schoelkopf's group [14].

In order to perform these seminal experiments, the circuits are brought to their ground state by passive cooling in a cryostat. This is still true for the experiments shown in this thesis. Whatever small residual coupling with the environment, results in a finite life-time of the excited states. We exploit this feature cooling our samples in a dilution refrigerator. This cryostat is a commercially available (although quite expensive) machine composed of 5 stages with decreasingly lower temperatures. The last stage presents a phonon temperature $T_{\mathrm{MC}} = 10\,\mathrm{mK}$. For a circuit in the microwave regime with a characteristic frequency, ω, the circuit excitation energy is much larger than the thermal fluctuations $\hbar\omega \gg k_{\mathrm{B}} T_{\mathrm{MC}}$. For a more detailed description, read Appendix A. Surprisingly, if we are not concerned about optimizing the quantum system controls, its lifetime, its energy levels, etc. all we need to do to make a circuit behave according to quantum mechanics is to fabricate a weak link and cool it down.

Finally, comparing the physical extension of the JJ to the wavelength, λ, of the electromagnetic wave used, we are in the deep sub-wavelength regime. In other words we can treat it as a lumped element in the circuit. This condition is usual for quantum optics with natural atoms; nevertheless, in cQED it is possible to design distributed components that span over many λ. On top of that, as far the elementary excitation in the system, $\hbar\omega$, obeys quantum mechanics, we do not have to be constrained to microwave photons. For example, we can study circuit quantum acoustodynamics (cQAD) with experiments involving propagating and stationary phonons, intrinsically reducing the wavelength by five orders of magnitude [15].

1.2 Sub-wavelength (lumped) oscillators

Many of the following results (for example the ones involving harmonic oscillators) can be obtained from a semiclassical or completely classical approach. The importance of deploying a full quantum mechanical description relies on mainly two aspects:

- having a comprehensive and single theory is easier to work with in the long run,
- the familiar behavior of semiclassical system can help to bridge some of the difficulties when there is no analogy in classical physics.

1.2.1 LC resonator

Before describing quantitatively a Cooper-pair box, it is instructive to write the Hamiltonian for an isolated LC circuit. This is not just a mere exercise, because many of the

systems we studied in this thesis can be approximated with this circuit. Moreover, the harmonic oscillator is experimentally used as a proxy of more complicated quantum circuits, not only to reduce the overhead in fabrication, but, more importantly to reduce the measurement time and simplify the experimental setup.

Explaining the technique for circuit quantization is out of the scope of this thesis, but fortunately, many reviews have extensively covered this procedure [8, 16, 17]. Consider an isolated LC circuit, with a charge Q in the capacitor, the Lagrangian of the isolated circuit is

$$\mathcal{L} = \frac{1}{2}L\dot{Q}^2 - \frac{1}{2}\frac{Q^2}{C}, \tag{1.6}$$

where C is the capacitance of the resonator L is its inductance[8]. Using the magnetic flux generated by the inductor Φ , which is the variable conjugate to the charge $\partial\mathcal{L}/\partial\dot{Q} = L\dot{Q} = \Phi$, we can derive the Hamiltonian of the circuit

$$H = \dot{Q}\Phi - \mathcal{L} = \frac{1}{2}\frac{\Phi^2}{L} + \frac{1}{2}\frac{Q^2}{C}. \tag{1.7}$$

From Hamilton's equations, we can derive the classical equations of motion:

$$\partial_t\Phi = -\partial H/\partial Q, \tag{1.8}$$

$$\partial_t Q = \partial H/\partial\Phi, \tag{1.9}$$

that combined give $\partial_t^2 Q = -Q/LC$. Both L and C being positive, we retrieve the well known oscillatory behavior with angular frequency:

$$\omega_r = 1/\sqrt{LC}. \tag{1.10}$$

It is important to notice that the energy oscillates between purely in the electric field to being purely in the magnetic field [see Eq. (1.7)]. Consequently, the ratio between the amplitudes of the electric and magnetic fields is:

$$Z_r = \sqrt{L/C}, \tag{1.11}$$

called the characteristic impedance of the oscillator.

We quantize the Hamiltonian promoting the charge and flux dynamical variables to operators that satisfy the commutation relation:

$$\left[\hat{\Phi}, \hat{Q}\right] = i\hbar. \tag{1.12}$$

Finally, rewriting them in terms of the annihilation and creation operators,

$$\hat{\Phi} = \sqrt{\frac{\hbar Z_r}{2}}\left(\hat{b}^\dagger + \hat{b}\right) = \Phi_{\mathrm{ZPF}}\left(\hat{b}^\dagger + \hat{b}\right) \tag{1.13}$$

$$\hat{Q} = i\sqrt{\frac{\hbar}{2Z_r}}\left(\hat{b}^\dagger - \hat{b}\right) = iQ_{\mathrm{ZPF}}\left(\hat{b}^\dagger - \hat{b}\right). \tag{1.14}$$

[8] In the circuits realized in this thesis, the capacitance ranges from 50 to 100 fF, while the inductance spans from 2 to 10 nH.

the harmonic oscillator Hamiltonian then assumes its usual form:

$$H = \hbar\omega_r\left(\hat{b}^\dagger\hat{b} + \frac{1}{2}\right). \tag{1.15}$$

Since we are interested in transition energies, in the following we will omit the zero point energy.

1.2.2 Vacuum fluctuations and impedance

In the following sections we will show that the coupling of two quantum systems is proportional to the number of excitations in the system and to the vacuum fluctuation. Therefore, in the quantum regime, with few excitation our ability to couple systems strongly depends on these quantities, hence the attention we are dedicating to vacuum fluctuations.

We can rewrite the flux and charge vacuum fluctuation, Φ_{ZPF} and Q_{ZPF} respectively, in terms of the elementary charge (a single Cooper pairs, $2e$) and flux (a single flux quantum Φ_0):

$$\Phi_{\mathrm{ZPF}} = \Phi_0\sqrt{\frac{Z_r}{4\pi R_{\mathrm{Q}}}} = \Phi_0\sqrt{\frac{\alpha}{4\pi}}\sqrt{\frac{Z_r}{Z_{\mathrm{vac}}}}, \tag{1.16}$$

$$Q_{\mathrm{ZPF}} = 2e\sqrt{\frac{R_{\mathrm{Q}}}{4\pi Z_r}} = \Phi_0\sqrt{\frac{1}{4\pi\alpha}}\sqrt{\frac{Z_{\mathrm{vac}}}{Z_r}}, \tag{1.17}$$

where we introduced the superconducting quantum resistance $R_{\mathrm{Q}} = h/(2e)^2 \approx 6.45\,k\Omega$, and the fine structure constant $\alpha = Z_{\mathrm{vac}}/8R_{\mathrm{Q}} \approx 1/137$. Interestingly, if we calculate the ratio of the normalized vacuum fluctuations we get

$$\frac{\Phi_{\mathrm{ZPF}}/\Phi_0}{Q_{\mathrm{ZPF}}/2e} = \alpha\frac{Z_r}{Z_{\mathrm{vac}}}. \tag{1.18}$$

Restricting to the geometric inductance, straight wires do not exceed the vacuum impedance, and the small value of α results in an asymmetry toward small flux fluctuations. Nevertheless we can overcome this limitation by designing specific geometries [18], using kinetic inductance [19], or exploiting arrays of JJs or SQUIDs [20–22]. In this thesis we will follow the latter approach.

The ratio between the amplitude of the electric field, proportional to $\hat{\Phi}$ and the magnetic one, proportional to $\hat{Q}$, is Z_r also in the quantum mechanical version of the LC circuit. In this context, this has deeper consequences, in fact the zero point fluctuations of voltage or current in the circuit are given by

$$\Delta\hat{V} = Q_{\mathrm{ZPF}}/C = \omega_r\sqrt{Z_r}\sqrt{\hbar/2} \tag{1.19}$$

$$\Delta\hat{I} = \Phi_{\mathrm{ZPF}}/L = \omega_r\frac{1}{\sqrt{Z_r}}\sqrt{\hbar/2}, \tag{1.20}$$

with the important result

$$\Delta\hat{V}/\Delta\hat{I} = Z_r. \tag{1.21}$$

At this point, it is natural to wonder what values these quantities assume in our circuits and possible natural limitation. We did not realize lumped LC-resonators, but the standard impedance for microwave components is $50\,\Omega$. If the resonator frequency $\omega_r \sim 2\pi 5\,\mathrm{GHz}$, the vacuum fluctuations result in the following expectation values

$$\langle\Delta\hat{V}\rangle \approx 1\,\mu\mathrm{V} \tag{1.22}$$

$$\langle\Delta\hat{I}\rangle \approx 30\,\mathrm{nA}. \tag{1.23}$$

1.2.3 Charge qubit and transmon regime

If we substitute the linear inductance in the LC-resonator with a JJ we obtain a qualitatively different system.

From a topological point of view, we separate the superconductor in two regions (see Fig. 1.3). Usually one of these regions is the large ground plane, while a smaller section is called island. On one hand, it is possible to have both these superconductors floating with respect to the ground plane (as for example used in [23]), while leaving the single qubit Hamiltonian unchanged. On the other hand the coupling Hamiltonian between two qubits will contain different terms depending which of the two approach is used [24, 25]. In this system, the only degree of freedom is the excessive charge on one electrode, hence the name **charge qubit**. Among the others, Nakamura investigated this arrangement, in a regime called Cooper pair box [13]. Other types of qubits can be obtaining with different arrangement of JJs. For example, Martinis used the phase (phase qubit) for the degree of freedom [26], Mooij et al. encoded the information in the flux (flux qubit) [27]. In this thesis, we will only use the charge qubit, and we will not investigate other qubit types any further.

From an energy point of view, also the level structure will be affected. In fact, considering the minimal charge ($2e$, a Cooper pair) tunneling through the junction with a frequency $\omega_\mathrm{q}/2\pi \sim 6\,\mathrm{GHz}$, it generates an effective current of $I \sim 2e\omega_\mathrm{q}/2\pi = 2\,\mathrm{nA}$. This is of the same order of magnitude as the critical current in the JJ, from Eq. (1.4) the nonlinear effects on the inductance are not negligible. We can estimate the energy necessary to build up a phase difference ϕ (see Fig. 1.3(c)) between the two electrodes of the junctions[8]:

$$\begin{aligned} E &= \int V(t)I(t)dt = \frac{\hbar I_c}{2e}\int \partial_t\phi \sin\phi dt \\ &= -E_\mathrm{J}\cos\phi, \end{aligned} \tag{1.24}$$

where we introduced the Josephson energy

$$E_\mathrm{J} = \frac{\hbar I_c}{2e}. \tag{1.25}$$

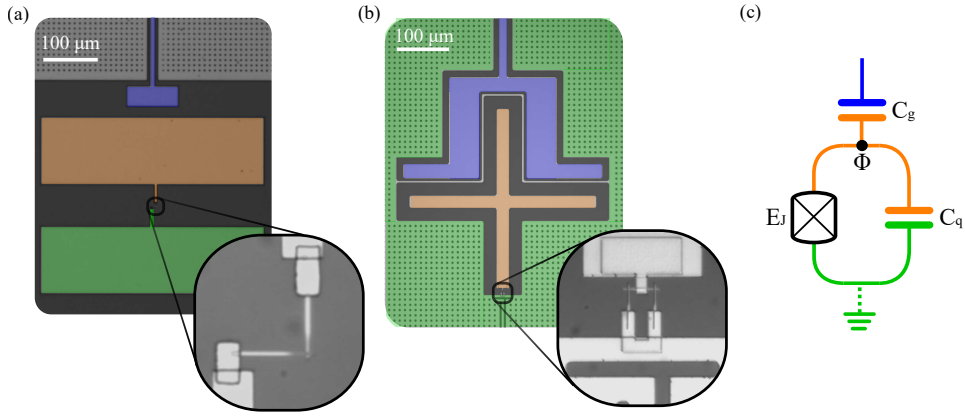

Figure 1.3: *Transmon qubit. (a) Floating transmon qubit fabricated in aluminium on silicon. A single JJ (in the zoom window) separate the two superconducting electrodes (orange and green). (b) A transmon qubit with the island (orange) shunted to the ground plane (green) by a SQUID (in the zoom window). (c) Electrical circuit equivalent of (a) and (b).*

We can write the Lagrangian of the circuit considering that a voltage generator can apply a classical potential $\partial_t \Phi_g$ on the capacitance, and

$$\mathcal{L} = \frac{\left(C_q \partial_t \Phi - C_g \partial_t \Phi_g\right)^2}{2(C_q + C_g)} + E_J \cos\phi. \tag{1.26}$$

As already mentioned, it is common to assume the excessive charge $\hat{n} = \hat{Q}/2e$, as one of the conjugate variables. We can calculate the Hamiltonian

$$\hat{H} = 4E_C(\hat{n} - n_g)^2 - E_J \cos\hat{\phi}, \tag{1.27}$$

where we introduced the charging energy $E_C = e^2/2(C_q + C_g)$, that together with E_J, are the only two energy scales in this circuit. In particular, the regime $E_J/E_C >> 1$, called the **transmon** regime, is the one that we chose in this thesis. Initially investigated in Schoelkopf Laboratory [28], the transmon exponentially suppresses charge noise. In fact, the m-th transition frequency, oscillates with an amplitude ϵ_m, periodically with the charge offset n_g

$$\epsilon_m \approx (-1)^m E_C \frac{2^{4m+5}}{m!}\sqrt{\frac{2}{\pi}}\left(\frac{E_J}{2E_C}\right)^{\frac{m}{2}+\frac{3}{4}} e^{-\sqrt{8E_J/E_C}}. \tag{1.28}$$

In our work, the frequency of the transmon qubit is between 4 and 7 GHz, and the anharmonicity is always below 300 MHz; we can easily estimate the ratio E_J/E_C ~40 to 60.

The characteristic impedance of this circuit is set by

$$Z_{\mathrm{q}} = \sqrt{\frac{L_{\mathrm{J}}}{C_{\mathrm{q}} + C_{\mathrm{g}}}}, \tag{1.29}$$

that for the junctions fabricated in this thesis we obtain $Z_{\mathrm{q}} \approx 300\,\Omega$. For small values of the phase, we can perturbatively expand the potential term in the Hamiltonian Eq. (1.27). Neglecting the charge offset n_g, we have

$$\hat{H} = E_{\mathrm{C}}\hat{n}^2 + E_{\mathrm{J}}\left(\hat{\phi}^2/2 - \hat{\phi}^4/4! - \hat{\phi}^6/6! + ...\right). \tag{1.30}$$

The first two terms correspond to the harmonic oscillator. If we also keep the 4-th power contribution, and we express $\hat{n}$ and $\hat{\phi}$ in terms of the creation and annihilation operators, we obtain

$$\hat{\phi} = \left(\frac{E_{\mathrm{J}}}{2E_{\mathrm{C}}}\right)^{1/4}\left(\hat{b}^\dagger + \hat{b}\right) = \phi_{\mathrm{ZPF}}\left(\hat{b}^\dagger + \hat{b}\right) \tag{1.31}$$

$$\hat{n} = \frac{i}{2}\left(\frac{E_{\mathrm{J}}}{2E_{\mathrm{C}}}\right)^{1/4}\left(\hat{b}^\dagger - \hat{b}\right) = \frac{i}{2}n_{\mathrm{ZPF}}\left(\hat{b}^\dagger - \hat{b}\right) \tag{1.32}$$

the approximated Hamiltonian becomes

$$\hat{H}/\hbar = \omega_{\mathrm{q}}\hat{b}^\dagger\hat{b} - \frac{E_{\mathrm{C}}}{2\hbar}\hat{b}^\dagger\hat{b}^\dagger\hat{b}\hat{b}, \tag{1.33}$$

where we introduced the transmon qubit frequency $\hbar\omega_{\mathrm{q}} = \sqrt{8E_{\mathrm{C}}E_{\mathrm{J}}} - E_{\mathrm{C}}$. For the rest of the thesis, we will express E_{C} in angular frequency. Hence, for many applications, the transmon qubit can be treated as a resonator with a weak Kerr nonlinearity E_{C}.

1.3 Waveguides

Many measurements in this thesis are performed with planar waves. A general form for a planar wave equation propagating in an homogeneous medium with speed v_{p} is

$$(\partial_t - v_p\partial_x)\psi = 0, \tag{1.34}$$

where ψ represents a mechanical, an electromagnetic or an elementary particle degree of freedom. A wave that satisfies this equation, propagates along a straight line. On one hand this may be trivial, since the equation presented is intrinsically in a single dimension, but this statement is true also for the three dimensional wave equation version. By adding boundary conditions to the physical system, and consequently to its mathematical representation, we confine the wave to smaller dimensions (from the three-dimensional space to two or one dimension) and guide its propagation. Such systems are called waveguides. For example, in the optical part of the electromagnetic

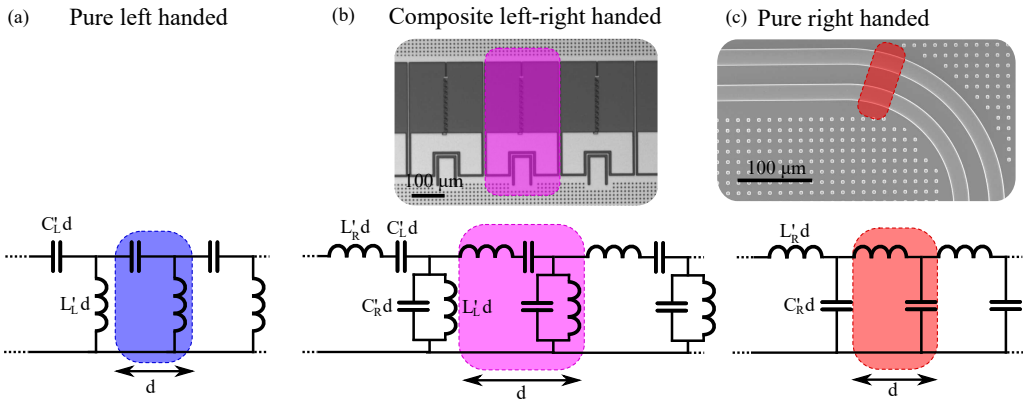

Figure 1.4: *Distributed lumped elements model for transmission line in microwave. (a) Left handed tranmission line. The electrical circuit is the dual of the more common right handed transmission line showed in (c), where the inductor and capacitor swap positions. (b) Composite left right handed trasmission line. Depending on the values of its components, the waveguide can present left or right handed features depending on the traveling wave frequency.*

spectrum, the waves are guided with dielectric transparent wires with large diffraction index (optical fibers). Mechanical waves do not propagate in vacuum so the surfaces of an elastic material confine and guide their propagation.

For microwaves, a single hollow conductor supports propagating modes where only the electric or magnetic components are perpendicular to the propagation direction (TE or TM modes, respectively). In this thesis we did not use TM or TE waveguides, so we will not discuss them further. Instead we concentrate on a transmission line given by two conductors close to each other, one commonly representing ground and the other the signal. In this case, in the propagating mode, both the electric and the magnetic field components are perpendicular to the propagation direction (TEM mode).

1.3.1 Waveguide circuit model

The microwave transmission lines are made out from circuits elements and can be modeled with discrete capacitors and inductors, arranged in different geometries (see Fig. 1.4). We can separate the waveguides used in this thesis in two families. The waveguides with a linear dispersion relation, right handed (RH) waveguides, usually realized with pieces of superconductors, are heavily used in cQED for coupling quantum systems or for transmitting pulses to excite them. The waveguides obtained with a periodic loading or an array structure result in a nontrivial dispersion relation, as the one realized for paper **Paper F**. In this category falls the left handed (LH) and composite right left handed waveguides (CRLH). The latter structures are sometimes called metamaterials, due to their unusual properties compared with naturally occurring materials.

This nomenclature, originally chosen by Veselago that theoretically studied the light transmission in these materials [29], relates the three vectors involved in waves propagation: electric **E** and magnetic **H** fields, and the Poynting vector $\mathbf{P} = \mathbf{E} \times \mathbf{H}$. For the majority of materials, the dielectric coefficient and the magnetic permeability are positive, $\epsilon, \mu > 0$, so that this vector triplet follows the right hand rules. If we instead assume both $\epsilon, \mu < 0$, the scalar product follows the left hand rule.

In order to quantize the transmission line with the same procedure followed for the lumped oscillators, we need to change the discrete index in the flux variable to a continuous variable

$$\Phi_i(t) \to \Phi(x,t). \tag{1.35}$$

Considering the RH transmission line, we can write the Lagrangian density

$$\mathfrak{L} = \frac{C'_{\mathrm{R}}}{2}(\partial_t \Phi)^2 - \frac{1}{2L'_{\mathrm{R}}}(\partial_x \Phi)^2. \tag{1.36}$$

The Euler-Lagrangian equations give the usual plane wave equation in two directions

$$(\partial_t^2 - \frac{1}{C'_{\mathrm{R}} L'_{\mathrm{R}}} \partial_x^2)\Phi = 0 \tag{1.37}$$

with a phase velocity $v_p = 1/\sqrt{C'_{\mathrm{R}} L'_{\mathrm{R}}}$. Considering a section of length d, with total capacitance C, and total inductance L, the phase velocity is

$$v_p = \frac{d}{\sqrt{LC}}. \tag{1.38}$$

This result may look surprising: an artificial waveguide realized with lumped L and C, in a section d long enough, would result in a superluminar propagation! This is, in fact, impossible. When we realize a waveguide with lumped element, we can neglect the propagation delay only if the cell section d is small enough. In this thesis the RH transmission line has a coplanar waveguide geometry. The phase velocity is then given by

$$v_p = c/\sqrt{\epsilon_{\mathrm{eff}}}, \tag{1.39}$$

where ϵ_{eff} is the effective dielectric constant of the transmission line. The exact value is a non analytical combination of the two dielectrics (usually substrate and vacuum[9]), that can be calculated solving Maxwell's equations.

1.3.2 Dispersion relation and density of state

The waveguides are used for coupling a quantum system to the classical world. Importantly, even when no pulses are used, they still modify the electromagnetic environment of the system. The density of states of the quantum system coupled to the waveguide is proportional to the inverse of the group velocity v_{g} [30]. Therefore, it is important to calculate (or measure) the dispersion relation of a waveguide. Following the derivation

[9] A simple rule of thumb gives $\epsilon_{\mathrm{eff}} = (\epsilon_{\mathrm{sub}} + \epsilon_{\mathrm{vac}})/2$

in the general case of a CLRH transmission line [31], we can define the impedance of the signal electrode per unit length

$$Z'(\omega) = i\left(\omega L'_{\mathrm{R}} - \frac{1}{\omega C'_{\mathrm{L}}}\right), \tag{1.40}$$

and the admittance between signal and ground per unit length

$$Y'(\omega) = i\left(\omega C'_{\mathrm{R}} - \frac{1}{\omega L'_{\mathrm{L}}}\right). \tag{1.41}$$

Considering d a section of the transmission line (the lattice constant), the dispersion relation is simply

$$\cos(kd) = 1 + \frac{1}{2}Z'Y'. \tag{1.42}$$

The group velocity can then be calculated

$$v_{\mathrm{g}} = \frac{\partial\omega}{\partial k}. \tag{1.43}$$

1.3.3 Mechanical waves on substrate surface

In a different approach to cQED, mechanical quanta, or phonons, can substitute the photons as the interaction mediator [15]. As the electromagnetic counterpart, in a defect-free lattice, phonons do not interact with other phonons, and propagate with low negligible loss. Remarkably, two features make them qualitatively different from photons:

- their propagation speed, 5 orders of magnitude smaller than that for light, imposes micrometer wavelengths in the GHz range. Except having a minuscule footprint compared with the cQED devices, this regime gives the possibility to explore effect of atoms much larger than the radiation wavelength [32]
- they do not propagate in vacuum. This feature makes it possible to drastically reduce unwanted radiative losses, realizing resonators with extremely high Q-factors $> 10^{10}$ [33]

In this thesis we use waves confined on the surface of the substrate, surface acoustic waves (SAWs) initially investigated by Lord Rayleigh [34]. On one hand, this lets us exploit the usual lithography process already developed for cQED, and on the other hand, it makes the devices really sensitive to surface imperfection. In **Paper C** we use the latter feature for acoustically investigating the two-level systems at the top of the substrate.

Due to the substrate lattice properties, SAW are naturally confined to propagate with small diffraction, so that the substrate itself constitutes our waveguide. Unfortunately, our instruments only generate photons. In this perspective, we use an interdigitate (IDT) transducer that converts electromagnetic waves from the coaxial lines of the cryostat to mechanical ones on the substrate.

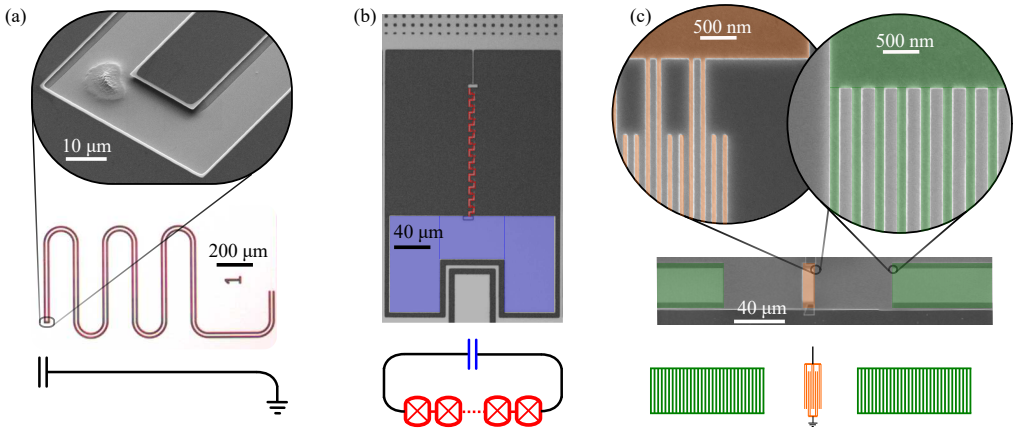

Figure 1.5: *Three types of distributed resonators used in this thesis. (a) Quarter wavelength resonator fabricated in aluminium on gallium arsenide. It consists of a section of a coplanar waveguide shorted to ground at one end, and open (zoomed window) at the other. (b) JJ resonator realized in aluminium on silicon. The circuits consists of a series of 10 JJ (in red) and a large capacitor (in blue). (c) SAW resonator realized in aluminum on gallium arsenide. Two Bragg mirrors (in green) facing each other, effectively creates a multimode cavity for mechanical waves, that can be excited with an IDT (in orange).*

1.4 Distributed resonators

One of the features of the lumped elements is the simplified treatment of their interaction with the electromagnetic or mechanical waves. In fact, we neglect any phase change of the waves. On the other hand, when we spread the circuit elements (capacitor and inductors) to an extent comparable with the photon wavelength, we cannot keep this assumption anymore. The relatively small increase in complexity, is overcome with benefits that these systems bring.

In this thesis we used three of such systems: a CPW quater wave resonator, a JJ array resonator, and finally a Bragg mirror resonator for SAW (see Fig. 1.5). Remarkably, the length scale in (a), (b) and (c) span 3 orders of magnitudes, nevertheless all three of these resonators have a spatial extension comparable with the excitation wavelength. In fact, while the phase velocity in a CPW geometry is only few times smaller than the c, the JJ resonator, depending on its parameters, may slow down light significantly. Finally, the SAW phase velocity, imposes wavelengths 5 orders of magnitude smaller compared to electromagnetic waves at the same frequency. In the rest of the section we will examine these systems more in details.

1.4.1 Coplanar waveguide resonators

Modifying the impedance of a transmission line, Z_0, results in a reflection of a traveling wave [35], with a reflection coefficient

$$S_{11} = \frac{Z - Z_0}{Z + Z_0}. \tag{1.44}$$

In particular, the short or open circuit condition is very efficiently implemented in a coplanar geometry. A segment of a transmission line with two such boundary conditions is called a **coplanar waveguide resonator** (see Fig. 1.5(a)). If the ends of the transmission line, apart from each other a physical length l, are open (shorted), the resonant conditions are met when the microwave field wavelength

$$n\lambda/2 = l, \qquad \text{(half wavelength resonator for } n = 1) \tag{1.45}$$

where n is the mode number. In this case the ends are current (voltage) nodes, and voltage (current) anti-nodes. This information is important to chose the position and type of coupling element when we will couple multiple circuits.

On the other hand, if one of the ends is open while the other is shorted, the resonances appear when

$$\left(n - \frac{1}{2}\right)\lambda/2 = l, \qquad \text{(quarter wavelength resonator for } n = 1). \tag{1.46}$$

Interestingly, for a chosen fundamental mode, the quarter wavelength resonator presents half of length compared with the other resonator, while the free spectral range is the same.

CPW resonators are very versatile in cQED because the large quality factor and the small mode volume that favor coupling with other systems. In fact, the first demonstration of strong coupling between a qubit and a resonator exploited this device [5]. These two features, together with the fabrication simplicity, makes the CPW resonator suitable for investigating loss in superconducting circuits [36–38]. Finally adding a tunable elements to one end, as a SQUID, the resonators can be parametrically driven, make it possible to study, among the others, dynamical Casimir effect, amplification and period multiplication [39–41].

In this thesis we use CPW resonators for direct investigation of losses in piezoelectric substrates (in **Paper B**), and as read-out resonators (in papers **Paper A**, **Paper E** and **Paper F**). We design the frequency of the first harmonic in the 4 to 8 GHz band, and we use an impedance of 50 Ω. With these quantities we can extract the total capacitance of our resonator to be C_r =600 fF and relative inductance L_r = 2 nH.

By imposing the short or the open boundary conditions, to the discrete model of the right-handed waveguide (see Fig. 1.4(c)), we obtain the harmonic oscillator Hamiltonian [8]:

$$\hat{H}/\hbar = \sum_n \omega_n \hat{b}^\dagger \hat{b}, \tag{1.47}$$

where ω_n are the resonant modes expressed in Eq. (1.46).

In this thesis, the total capacitance of the resonator, $C_r \sim 600\,\mathrm{fF}$ is much larger than the coupling capacitance, $C_c \sim 10\,\mathrm{fF}$, so Eq. (1.47) is still valid, while ω_n is obtained from the perturbative treatment around the resonant condition Eq. (1.46).

1.4.2 JJ and SQUID array resonators

In this thesis we use the JJs array resonators. In Fig. 1.6(a) we show the electrical equivalent representation of our devices. If we disregard the capacitance at the end of the circuit, the JJ array is a discrete realization of a section of right hand transmission line, with inductance substituted by JJs. For a case in which we can neglect C_r, it should not surprise that we have similar resonant modes, displayed in Fig. 1.1(b).

In general, each electrode that connects two junctions has a spurious capacitance C_0 to ground. Accounting also for the capacitance of the JJ, in the linearized regime, the Lagrangian for the circuit is

$$\mathcal{L} = \frac{1}{2}C_r(\partial_t\Phi_N)^2 + \sum_n^N \frac{1}{2}C_0(\partial_t\Phi_n)^2 + \frac{1}{2}C_\mathrm{J}\left(\partial_t\Phi_n - \partial_t\Phi_{n+1}\right)^2 - \frac{1}{2L_\mathrm{J}}\left(\Phi_n - \Phi_{n+1}\right)^2 \tag{1.48}$$

$$= \frac{1}{2}\partial_t\mathbf{\Phi}^T\mathbf{C}\partial_t\mathbf{\Phi} - \frac{1}{2}\mathbf{\Phi}^T\tilde{\mathbf{L}}\mathbf{\Phi}, \tag{1.49}$$

with the vector notation $\mathbf{\Phi} = (\Phi_1, ..., \Phi_N)^T$, the tridiagonal capacitance matrix

$$\mathbf{C} = \begin{pmatrix} C_\mathrm{J}+C_0 & -C_\mathrm{J} & 0 & \dots & 0 & 0 & 0 \\ -C_\mathrm{J} & 2C_\mathrm{J}+C_0 & -C_\mathrm{J} & \dots & 0 & 0 & 0 \\ 0 & -C_\mathrm{J} & 2C_\mathrm{J}+C_0 & \ddots & 0 & 0 & 0 \\ \vdots & \vdots & \ddots & \ddots & \ddots & \vdots & \vdots \\ 0 & 0 & 0 & \ddots & 2C_\mathrm{J}+C_0 & -C_\mathrm{J} & 0 \\ 0 & 0 & 0 & \dots & -C_\mathrm{J} & 2C_\mathrm{J}+C_0 & -C_\mathrm{J} \\ 0 & 0 & 0 & \dots & 0 & -C_\mathrm{J} & C_r+C_\mathrm{J}+C_0 \end{pmatrix} \tag{1.50}$$

and the tridiagonal inductance matrix[10]

$$\tilde{\mathbf{L}} = \frac{1}{L_\mathrm{J}}\begin{pmatrix} 1 & -1 & 0 & \dots & 0 & 0 \\ -1 & 2 & -1 & \dots & 0 & 0 \\ 0 & -1 & 2 & \ddots & 0 & 0 \\ \vdots & \vdots & \ddots & \ddots & \ddots & \vdots \\ 0 & 0 & 0 & \ddots & 2 & -1 \\ 0 & 0 & 0 & \dots & -1 & 1 \end{pmatrix}. \tag{1.51}$$

From simple visual inspection of $\mathbf{C}$ (or directly from the circuit) we realize that the capacitance C_r breaks the symmetry of the resonators.

In the case where $C_r \ll C_\mathrm{J}, C_0$, initially studied in [20], we can neglect C_r contribution, obtaining the dispersion relation (or also the normal modes resonances):

$$\omega_k = \omega_\mathrm{p}\sqrt{\frac{1}{1 + \frac{C_0}{2C_\mathrm{J}}\frac{1}{1-\cos(\pi k/N)}}}, \qquad k \in \left[-\frac{N}{2}, \frac{N}{2}\right] \tag{1.52}$$

[10] Notice that the physical dimensions of $\tilde{\mathbf{L}}$ are the inverse of an inductance.

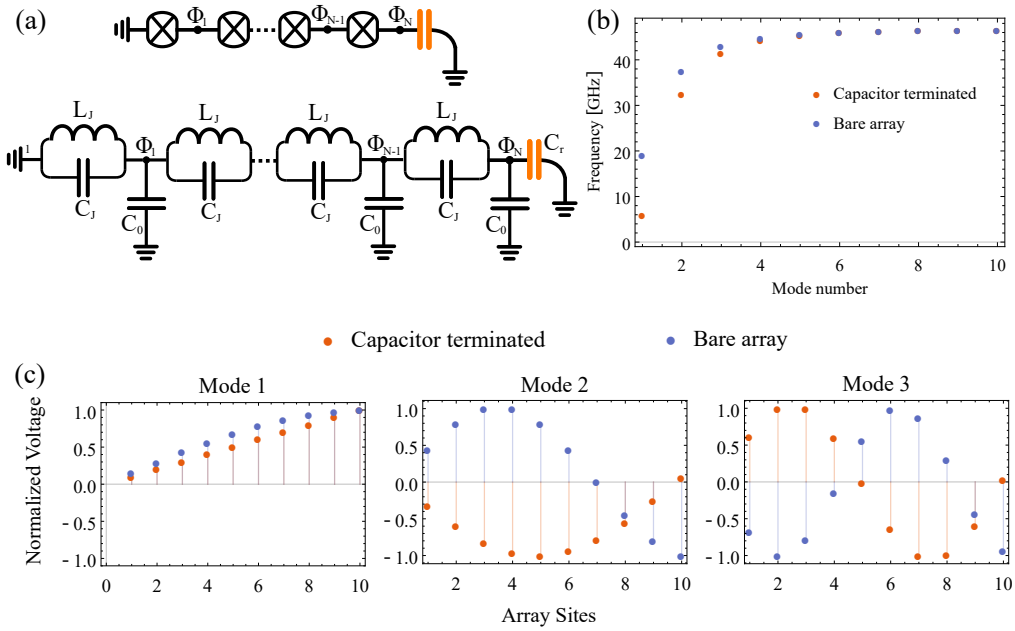

Figure 1.6: *Modes frequency and structure of a Josephson Junction array resonator. (a) In the low excitation regime, a JJ array resonator shunted by a capacitor (upper circuit) can be linearized substituting the junction with the equivalent inductor L_J and capacitor C_J. Moreover we consider also the effective capacitance to ground C_0 (lower circuit). (b) Different modes frequency with and without the large shunted capacitor. (c) Comparison of the voltage at each node for the same JJ array, with and without the shunt capacitor.*

where $\omega_p = 1/\sqrt{L_J C_J}$ is the plasma frequency of the JJ. The modes frequencies are shown in Fig. 1.6. We design our device to be in the opposite regime, $C_r \gg C_J, C_0$, pushing the ground plane far from the junctions array (see Fig. 1.5(b)). Nevertheless, from electrostatic simulations (see appendix C), we cannot completely neglect C_0, and an analytical approach is hard.

The numerical evaluation of the resonant modes of the JJ resonator, with the parameters we used in the experiments is shown in Fig. 1.6(b). The first resonant mode yields at 5.5 GHz, while the second mode is much far detuned, resonating above 30 GHz. This is a consequence of the large shunting capacitor. Also the mode structure is drastically altered by the capacitor. In Fig. 1.6(c) we plot the mode structure for the first three array modes, for the case with (in orange) and without (in blue) the large shunted capacitance. In our experiment we treat the JJ resonator as a single mode, only considering its first array mode.

1.4.3 SAW resonators

Periodically altering the property of the surface, produces a forbidden propagation region for traveling mechanical waves, a phononic bandgap. In particular, we realize an aluminum grating with a lattice constant equal to the wavelength of the SAWs (see Fig. 1.5(c)). This results in a twofold loading of the surface: a mechanical loading, due to a larger stiffness of the metal compared to GaAs and due to an additional periodic mass, and an electrical loading, due to the superconducting properties "shortening" the piezoelectricity of the substrate (see chapter 2). The grating opens stop bands for propagating SAWs when multiples of the wavelength match the pitch of the grating [42]. Two gratings in front of each other produce a Fabri-Perot cavity [43], with resonant frequencies in correspondence of the stop bands. The resonances can be probed by including an IDT transducer between the two mirrors. In this thesis we used only the first stop band.

These devices have been successfully coupled to qubits [44], making it possible to investigate, for example, phonon Fock state [45] or radiation pressure [46]. Interestingly, breaking the mirror in two electrodes and reconnecting them with a SQUID, introduces a nonlinearity in the mechanical modes that can be used for two mode squeezing (see Paper II for details).

1.5 Coupling quantum systems

Two coupled systems can transfer an excitation of one, $\hat{b}$, to another $\hat{c}$,

$$\hat{H} = \hbar\omega_b \hat{b}^\dagger \hat{b} + \hbar\omega_c \hat{c}^\dagger \hat{c} + \hat{H}_{\text{int}}, \tag{1.53}$$

where we introduced the interaction Hamiltonian,

$$\hat{H}_{\text{int}}/\hbar = g(\hat{b}^\dagger + \hat{b})(\hat{c}^\dagger + \hat{c}) = g(\hat{b}^\dagger \hat{c} + \hat{c}^\dagger \hat{b}) + g(\hat{b}^\dagger \hat{c}^\dagger + \hat{b}\hat{c}) \tag{1.54}$$

where g is called coupling or interaction strength, and, in general, it is proportional to the number of excitations in the system, n, and to the vacuum fluctuation, V_{ZPF}. We are

interested in the evolution on a time scale set by g. However, when $g \ll \omega_i$, the terms $\hat{b}^\dagger\hat{c}^\dagger$ and $\hat{b}\hat{c}$ produce an evolution much faster, that averages out on the time scale of interest. Applying a secular approximation, we can drop these terms [47, 48]. With this approximation, called rotating wave approximation (RWA) in quantum optics [49], the total Hamiltonian preserves the number of excitations in the system

$$\left[\hat{H}, \hat{b}^\dagger\hat{b}\right] = \left[\hat{H}, \hat{c}^\dagger\hat{c}\right] = 0. \tag{1.55}$$

At this point many energy scales (or equivalently time scales) are present in the systems: the systems resonances ω_i, their total decay rates, κ, γ, and the interaction strengths g_i. We can identify three different regimes.

Weak coupling: the losses of the systems are larger than the coupling $g \ll \kappa, \gamma$. In time domain, there is no coherent exchange between the two systems, while in frequency space the line width of two resonant systems are not resolved.

Strong coupling: the coupling strength is larger than the decay rates $g \gg \kappa, \gamma$ but it is still a small fraction of the transition frequency of the system $g/\omega_i < 0.1$. In this regime, we can resolve coherent exchange and spectroscopically identify the avoided crossing of the two resonances. All the systems studied in this thesis fit this category.

Ultrastrong coupling: the interaction strength becomes an appreciable fraction of the transition frequency $g/\omega_i > 0.1$. In this regime, only recently experimentally accessible, many of the usual assumption in cQED break down: for example, the rotating wave approximation is not valid [49], or the Purcell effect is modified [50]. Additional information about this regime can be found in [51] .

In naturally occurring quantum systems, the photon is the mediator of the electric interaction. In particular, the fine structure constant, $\alpha = Z_{\mathrm{vac}}/(2R_{\mathrm{Q}}) \approx 1/137$ sets the interaction strength between a charged elementary particle and a photon [52]. The small value of this constant sets the qualitative behavior of light-matter interaction; for example, the spontaneous decay rate γ of an atomic transition ω_{a}, due to the interaction of the atom with the photonic vacuum fluctuation, is

$$\gamma \approx \omega_{\mathrm{a}}\alpha^3, \tag{1.56}$$

i.e. in our universe the atomic linewidths are sharp [53]. We already mentioned that the light-matter interaction can be enhanced by confining the atom in a resonant cavity. In this case the dimensionless coupling

$$\tilde{g}_{\mathrm{cav}} \approx \frac{\alpha^{3/2}}{\sqrt{\tilde{V}}} \approx 10^{-6}, \tag{1.57}$$

where we introduced the dimensionless mode volume $\tilde{V}$ of the cavity. Despite the small value of this coupling, it is possible to achieve strong coupling, in fact the ratio

$$\frac{\tilde{g}_{\mathrm{cav}}}{\gamma/\omega_{\mathrm{a}}} \approx \frac{\alpha^{-3/2}}{\sqrt{\tilde{V}}} \tag{1.58}$$

can be made larger than unity.

In this section, we study this interaction for artificial matter in the frame of cQED and cQAD. Remarkably, designing the interaction with lumped elements and confining it in one dimension can boost the interaction by up to four orders of magnitude. As we will see in this section, the dimensionless transmon-resonator coupling

$$\tilde{g}_{\text{res}} \approx n_{ZPF}\sqrt{\frac{Z_q}{Z_{\text{vac}}}}\frac{C_{\text{c}}}{C_{\text{c}}+C_q}\alpha^{1/2} \approx 10^{-2}, \tag{1.59}$$

where C_{c} is the coupling capacitance between the resonator and the transmon. In this case, the ratio between coupling strengths and losses can be made orders of magnitude larger than 1. This imply that the two system can store and manipulate the quantum information for a long time before losing the excitations.

1.5.1 Coupling of resonant circuits

Relating the coupling coefficient with the circuit parameters, not only gives a direct design tool for the experiments, but also make it possible to estimate the achievable values for these quantities. Experimentally, coupling two resonant circuits is as simple as introducing a mutual capacitance, and in this thesis almost all couplings have a capacitive nature. If we consider two LC-resonators with a coupling capacitance C_{c}, their Lagrangian is

$$\begin{aligned}\mathcal{L} &= \mathcal{L}_1 + \mathcal{L}_2 + \mathcal{L}_{\text{int}} \\ &= \frac{1}{2}C_1(\partial_t\Phi_1)^2 - \frac{1}{2L_1}\Phi_1^2 + \frac{1}{2}C_2(\partial_t\Phi_2)^2 - \frac{1}{2L_2}\Phi_2^2 + \frac{1}{2}C_{\text{c}}(\partial_t\Phi_1 - \partial_t\Phi_2)^2 \\ &= \frac{1}{2}\partial_t\mathbf{\Phi}^T\mathbf{C}\partial_t\mathbf{\Phi} - \frac{1}{2}\mathbf{\Phi}^T\tilde{\mathbf{L}}\mathbf{\Phi},\end{aligned} \tag{1.60}$$

with C_1 and C_2 (L_1 and L_2) the capacitances (inductances) of resonator 1 and 2 respectively. Introducing the conjugate charge variables

$$Q_i = \frac{\partial\mathcal{L}}{\partial(\partial_t\Phi_i)} \qquad i = 1,2 \tag{1.61}$$

the Hamiltonian is given by the Legendre transformation

$$H = \frac{1}{2}\mathbf{Q}^T\mathbf{C}^{-1}\mathbf{Q} + \frac{1}{2}\mathbf{\Phi}^T\tilde{\mathbf{L}}\mathbf{\Phi}. \tag{1.62}$$

Introducing the resonator frequencies $\omega_i = \sqrt{\mathbf{C}_{ii}^{-1}/L_i}$ and the usual commutation relations $\left[\hat{\Phi}_n, \hat{Q}_m\right] = i\hbar\delta_{nm}$, we can express the Hamiltonian as

$$\hat{H}/\hbar = \omega_1\hat{b}^\dagger\hat{b} + \omega_2\hat{c}^\dagger\hat{c} + g(\hat{b}^\dagger - \hat{b})(\hat{c}^\dagger - \hat{c}), \tag{1.63}$$

where we have used

$$\hat{\Phi}_1 = \sqrt{Z_1}\sqrt{\hbar/2}\left(\hat{b}^\dagger + \hat{b}\right) \qquad \hat{Q}_1 = i\frac{1}{\sqrt{Z_1}}\sqrt{\hbar/2}\left(\hat{b}^\dagger - \hat{b}\right), \tag{1.64}$$

$$\hat{\Phi}_2 = \sqrt{Z_2}\sqrt{\hbar/2}\left(\hat{c}^\dagger + \hat{c}\right) \qquad \hat{Q}_2 = i\frac{1}{\sqrt{Z_2}}\sqrt{\hbar/2}\left(\hat{c}^\dagger - \hat{c}\right), \tag{1.65}$$

$$g = \sqrt{\omega_1\omega_2}\frac{C_\mathrm{c}}{2\sqrt{(C_1+C_\mathrm{c})(C_2+Cc)}} = \frac{1}{2}\omega_1\omega_2 C_\mathrm{c}\sqrt{Z_1 Z_2} \tag{1.66}$$

1.5.2 Atom in a cavity and the Jaynes-Cumming Hamiltonian

The interaction between a cavity mode and an atom has a privileged role in cQED and more generally in quantum optics. In a semi-classical approach, Rabi introduced the Hamiltonian of atom and classical field [54]

$$\hat{H}_\mathrm{R}/\hbar = \omega\hat{a}^\dagger\hat{a} + \frac{1}{2}\omega_\mathrm{q}\hat{\sigma}_z + g\hat{\sigma}_x\left(\hat{a}^\dagger + \hat{a}\right). \tag{1.67}$$

Jaynes and Cumming studied the Rabi model when the radiation is a quantized cavity mode with frequency ω_r [55]. In this case, after applying the RWA, they obtained the Hamiltonian

$$\hat{H}_\mathrm{JC}/\hbar = \omega_r\hat{a}^\dagger\hat{a} + \frac{1}{2}\omega_\mathrm{q}\hat{\sigma}_z + g\left(\hat{a}^\dagger\hat{\sigma}^- + \hat{\sigma}^+\hat{a}\right) \tag{1.68}$$

In the **dispersive** regime, $(\omega_\mathrm{r} - \omega_\mathrm{q}) \gg g$, the Hamiltonian can be written as

$$\hat{H}_\mathrm{disp} = (\omega_r + \chi\hat{\sigma}_z)\hat{a}^\dagger\hat{a} + \frac{1}{2}\left(\omega_q + \frac{g^2}{\Delta}\right)\hat{\sigma}_z \tag{1.69}$$

where $\chi = g^2/\Delta$. This is only true for a two level system. For a transmon qubit, which has mode levels, this is modified to[28]

$$\chi = \frac{g^2}{\Delta}\frac{E_\mathrm{C}}{E_\mathrm{C}-\Delta}. \tag{1.70}$$

1.5.3 Coupling to waveguide

In this thesis we couple lumped or distributed elements to waveguides, in three possible geometries depicted in Fig. 1.7, reflection, transmission and notch configuration; for simplicity we will discuss the capacitive coupling case here, while the inductive case is treated on each experiment in the following chapters.

In cQED, a purely microwave engineering approach, or a purely quantum optics one, are effective. Considering that in both theories, the system has an undulatory behavior, this should not leave the reader surprised. Both techniques were, in fact, developed for the study of propagating or stationary waves. Here we will use quantum optics methods.

If we drive a resonator with a coherent tone, different configurations have different responses. As an example we can derive the reflected signal of a resonator coupled at the

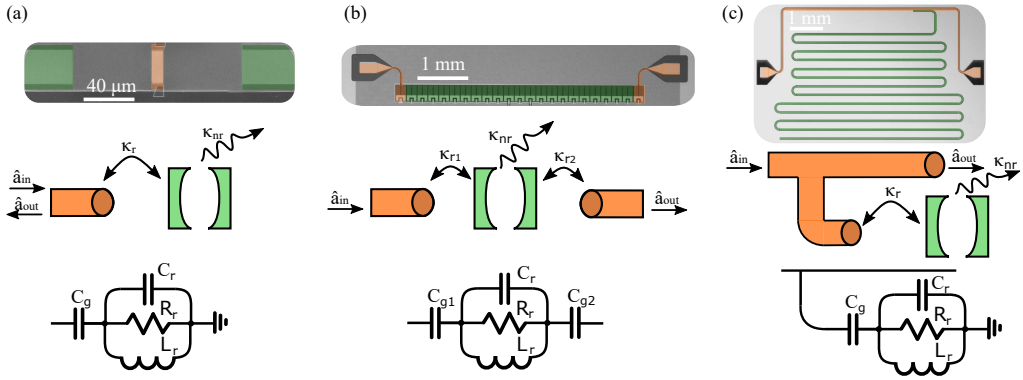

Figure 1.7: *Waveguide coupling topologies. (a) Reflection. The input field $\hat{a}_{\rm in}$ interact with the cavity and the output $\hat{a}_{\rm out}$ propagates back into the waveguide in the opposite direction. (b) Transmission. The field injecting from one waveguide, interacts with the quantum system, propagates into a second waveguide. The reflection in this configuration, is the same as the case shown in (a) where the decay in the second waveguide is incorporated in the nonradiative decay. (c) Notch. The waveguide where the field travels, is not interrupted, so the signal is not scattered by waveguide boundary, but only by the cavity. Even if the SNR reduction in this configuration, may preclude its use in some applications, the possibility to multiplex many system on the same waveguide makes this geometry very appealing.*

end of the waveguide with rate $\kappa_{\rm r}$, with internal loss $\kappa_{\rm nr}$ [see Fig. 1.7(a)]. When we drive the system with an external field $\hat{a}_{\rm in}$, the Heisenberg equation is

$$\partial_t \hat{b}(t) = i\left[\hat{H}, \hat{b}(t)\right] - 1/2\,(\kappa_{\rm r} + \kappa_{\rm nr})\,\hat{b}(t) + \sqrt{\kappa_{\rm r}}\hat{a}_{\rm in}(t) \tag{1.71}$$

If the driving field $\hat{a}_{\rm in}(t) = \hat{a}_{\rm in} e^{-i\omega t}$, confining the time dependence of the intra-cavity field only to its phase, $\hat{b}(t) = \hat{b} e^{-i\omega t}$, the Hilbert equation becomes:

$$i(\omega - \omega_0)\hat{b} - 1/2\,(\kappa_{\rm r} + \kappa_{\rm nr})\,\hat{b} + \sqrt{\kappa_{\rm r}}\hat{a}_{\rm in} = 0 \tag{1.72}$$

Finally using the input-output relation:

$$\langle \hat{a}_{\rm in} \rangle + \langle \hat{a}_{\rm out} \rangle = \sqrt{\kappa_{\rm r}}\hat{b} \tag{1.73}$$

we can calculate the reflection coefficient:

$$S_{11} = \frac{\langle \hat{a}_{\rm in} \rangle}{\langle \hat{a}_{\rm out} \rangle} \tag{1.74}$$

and substituting the

$$S_{11} = \frac{\kappa_{\rm nr} - \kappa_{\rm r} + 2i(\omega - \omega_0)}{\kappa_{\rm nr} + \kappa_{\rm r} + 2i(\omega - \omega_0)}. \tag{1.75}$$

The same procedure can be applied to the transmission configuration, in Fig. 1.7(b),

$$S_{21} = \frac{2\sqrt{\kappa_{r1}\kappa_{r2}}}{\kappa_{r1} + \kappa_{r2} + \kappa_{\rm nr} + 2i(\omega - \omega_0)} \tag{1.76}$$

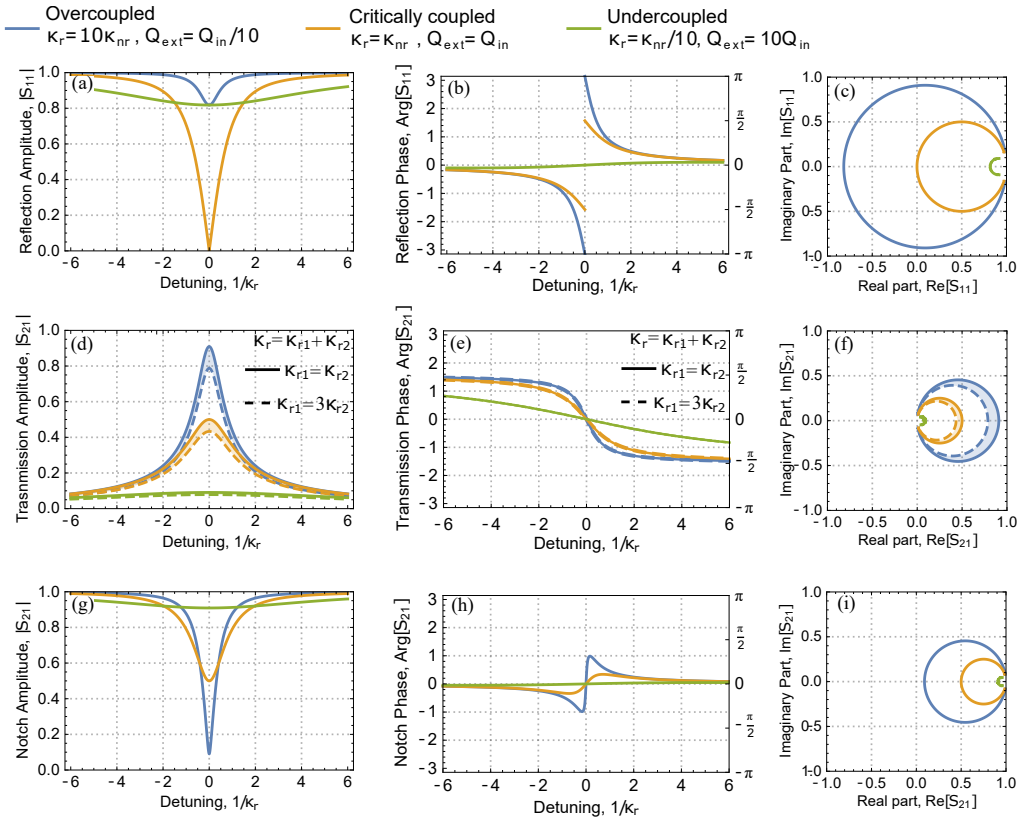

Figure 1.8: *Measurement response of resonators in reflection (a-c), transmission (d-f) and notch configuration (g-i) to a coherent tone. The colors highlight the overcoupled (blue), critically coupled (orange) and undecoupled (green) regime.*

and to the notch one, in Fig. 1.7(c)

$$S_{21} = \frac{\kappa_{\rm nr} + 2i(\omega - \omega_0)}{\kappa_{\rm r} + \kappa_{\rm nr} + 2i(\omega - \omega_0)}. \tag{1.77}$$

The plot of the expected reflection or transmission coefficient is shown in Fig. 1.8. As usual, it is very interesting to link the coupling coefficient to the electric components of the equivalent circuit. The radiative decay can be expressed as

$$\kappa_{\rm r} = \omega_r^2 Z_0 \frac{C_{\rm c}^2}{C_r + C_{\rm c}} = \omega_r \frac{Z_0}{Z_r} \left(\frac{C_{\rm c}}{C_r + C_{\rm c}} \right)^2 \tag{1.78}$$

while the nonradiative decay

$$\kappa_{\rm nr} = \frac{1}{R(C_r + C_c)} \tag{1.79}$$

1.5.4 Quality factor

An important figure of merit for resonators in the quality factor Q, a dimensionless parameter that, roughly speaking, describe how many cycles the resonator finishes, before its energy decays:

$$Q = 2\pi \frac{\text{Energy stored}}{\text{Energy lost per cycle}} = \frac{E_{\text{tot}}}{\Delta E}. \tag{1.80}$$

This quantity comes in handy when we want to compare different loss channels in resonators with different frequencies. In particular if we can factorize the total loss in different channels $\Delta E = \sum_i \Delta E_i$, the total Q-factor

$$\frac{1}{Q} = \frac{\Delta E}{E_{\text{tot}}} = \sum_i \frac{\Delta E_i}{E_{\text{tot}}} = \sum_i \frac{1}{Q_i} \tag{1.81}$$

Remarkably, as for the radiative and nonradiative decay, we can separate the total quality factor in internal quality factor,

$$Q_{\text{i}} = \omega_r / \kappa_{\text{nr}}, \tag{1.82}$$

and external one,

$$Q_{\text{ext}} = \omega_r / \kappa_{\text{r}}. \tag{1.83}$$

The total Q for the resonators and qubits investigated in this thesis, range from 10^3 to 10^6. While Q_{ext} is set by design, many factors limit Q_{i} and in chapter 2 we will identify some of them, quantitatively study them and implement strategies to reduce or eliminate them.

–If we're collapsing right now, I'm gonna collapse on them. I'm not gonna wait for them to collapse on us.

Coherence, Oscilloscope Pictures (2013)

2 Coherence

Coherence is one of the most important properties for a quantum system. It describes the possibility to have quantum interference effects between its degrees of freedom. The evolution of the degrees of freedom, is described by an unitary matrix, independently on how large the system is. However, when we only focus on the few ones of a quantum circuit, we can observe the loss of coherence (or decoherence) due to the interaction with the remaining degrees of freedoms of the environment (or baths).

Representing the state of the circuit with a density matrix, $\hat{\rho}(t)$, the decoherence describes the decay of diagonal and off-diagonal elements to the stationary value, representing the population and coherence respectively. These processes are called relaxation and dephasing.

In this chapter we explore the decoherence caused by defects on the surface of the substrate where the circuits are fabricated or in the interfaces between the superconductors and vacuum. They behave as a bath of two levels systems, electrically or mechanically coupled to the circuit. Moreover, we investigate the effect of the photonic bath in the highly attenuated coaxial line which we use to drive or readout the qubit, and finally we measure the effect of a strong coupling between superconducting resonators and the phonons on the substrate.

2.1 Decoherence sources

The quantum systems we implement in cQED are superconducting circuits cooled to their quantum mechanical ground state and manipulated with microwave signals. In chapter 1 we introduced the ideal case, where the circuits are in vacuum. In a more accurate treatment, many baths weakly coupled to the quantum system, alter its spectrum and influence its behavior.

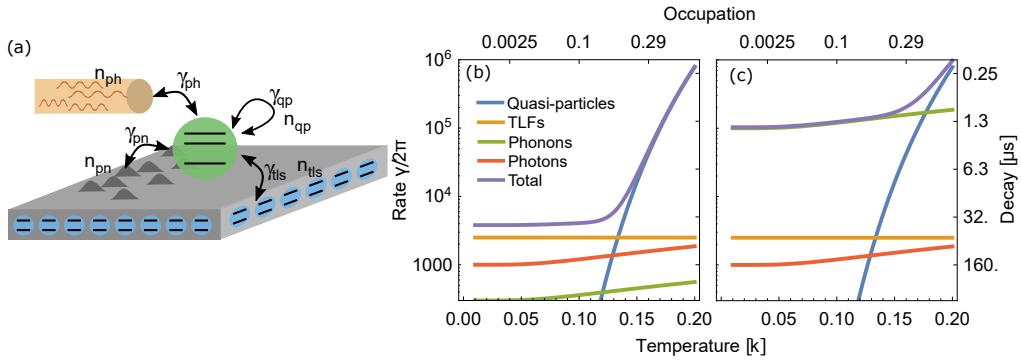

Figure 2.1: *Decay rate of the qubit due to unwanted coupling to thermal baths. (a) Sketch of an artificial atom coupled to the photons in the waveguide, to phonons in the substrate, to two-level systems on the surfaces of the superconductors and substrate, and to quasiparticles in the metal. (b) When all the baths are in thermal equilibrium with the mixing chamber plate, we can plot the individual baths contribution to the relaxation of the atom. In particular we plot the loss rate of the atom using the common values we obtain in the fabrication on silicon (b), or on gallium arsenide (c).*

In Fig. 2.1(a) we sketch an artificial atom and the surrounding baths with the largest coupling strengths, $\gamma_{\rm ph}, \gamma_{\rm pn}, \gamma_{\rm TLS}, \gamma_{\rm qp}$ that refer to the photonic, phononic, two-level systems and quasi-particles baths, respectively. By restricting to the single excitation subspace (or equivalently considering a perfect two level system), we can calculate the evolution of the system solving the master equation [8, 56]

$$\partial_t \hat{\rho} = \frac{i}{\hbar}\left[\hat{\rho}, \hat{H}_0\right] + \left(\sum_k \gamma_k (1+n_k)\right) D[\hat{\sigma}^-]\hat{\rho} + \left(\sum_k \gamma_k n_k\right) D[\hat{\sigma}^+]\hat{\rho}, \tag{2.1}$$

where the k-index runs over different baths, n_k is the average occupation number of the baths, $\hat{H}_0 = \hbar\omega_{\rm q}\hat{\sigma}_z/2$ is the atom Hamiltonian and finally we define the Lindblad superoperator (dissipator)

$$D[\hat{O}]\hat{\rho} = \hat{O}\hat{\rho}\hat{O}^\dagger - \frac{1}{2}(\hat{O}^\dagger\hat{O}\hat{\rho} + \hat{\rho}\hat{O}^\dagger\hat{O}). \tag{2.2}$$

By solving for the population ρ_{11} and ρ_{22}, we obtain an exponential relaxation with a characteristic time T_1, given by

$$1/T_1 = \gamma = \gamma_{\rm ph}(1+2n_{\rm ph}) + \gamma_{\rm pn}(1+2n_{\rm pn}) + \gamma_{\rm tls}(1+2n_{\rm tls}) + \gamma_{qp}(1+2n_{\rm qp}). \tag{2.3}$$

The phonons in the substrate are cooled to $T = 10\,\text{mK}$. Using the Bose-Einstein distribution for microwave phonons at $\omega/2\pi = 5\,\text{GHz}$ gives

$$n = \frac{1}{e^{\frac{\hbar\omega}{k_{\rm B}T}} - 1} \approx 4\cdot 10^{-11}. \tag{2.4}$$

At these temperatures, the baths are usually out of thermal equilibrium, with an average occupation many orders of magnitude larger than the one calculated with Eq. (2.4). In **Paper D** and in **Paper E** we measure the population of the photons and TLSs, respectively. This knowledge can be used to benchmark setups with optimized thermalization and, more importantly, for experiments of bath engineering. For example, the microwave modes in a waveguide can be used as a thermal bath in quantum thermodynamics experiments[57–59], where the bath temperature needs to be probed accurately.

One way to mitigate the total relaxation rate of the atom is to limit the population of these baths. A large effort, over the past two decades, improved the lifetime of the transmon qubits up to a few hundreds of microseconds[60]. In particular, the quasi-particles population can be reduced by shielding from stray radiation [61], engineering metallic traps [62], or actively cooling them down [63]. The photonic population can be lowered by improving attenuators thermalization [64] or by embedding the system in a detuned cavity [65–67]. Single TLSs coupled to a qubit have been spectroscopically measured as a function of their frequency [68]. A similar experiment [69] located their presence on the substrate and metal surfaces. Nevertheless the nature of the TLS bath is still under investigation, and further research is necessary to understand how to reduce their density and temperature. In appendix A we present the general setup used in the experiments, where we implemented many of the aforementioned strategies.

The complementary approach consists in reducing the coupling of the baths. The quasi-particles decay rate is given by [61] is

$$\gamma_{\mathrm{qp}} = \frac{\omega_r}{\pi}\beta_{\mathrm{k}}\sqrt{4\pi\frac{k_{\mathrm{B}}T}{\hbar\omega_r}}e^{-\frac{\Delta_{\mathrm{s}}}{k_{\mathrm{B}}T}}, \tag{2.5}$$

where β_{k} is the kinetic inductance ratio (a function of geometry), and the only free parameter is the superconducting energy gap, Δ_{s}. While many superconductors have been investigated [70, 71], this research is still active.

When the driving power of the circuits is smaller than a critical photon number (depending on the substrate and geometry), the TLSs coupling [72]

$$\gamma_{\mathrm{tls}} = \omega_r F\delta_{\mathrm{t}}\tanh\left(\frac{\hbar\omega_r}{2k_BT}\right), \tag{2.6}$$

where δ_{t} is the intrinsic loss tangent of the substrate [35], and F is the filling factor (the ratio of the electric field produced by the circuits that thread the substrate). In this case, reducing F [73, 74] or choosing low loss substrate [75] effectively reduces the coupling of the qubit with the TLSs. In our devices the value $F\delta \approx 10^{-6}$ for both silicon and gallium arsenide.

The coupling to the photonic environment depends on the system geometry. If the circuit is directly coupled to the waveguide, $\gamma_{\mathrm{ph}} = \kappa_{\mathrm{r}}$. In case a resonator Purcell protects the atomic system then

$$\gamma_{\mathrm{ph}} = \kappa_{\mathrm{r}}\frac{g^2}{\Delta^2}\frac{\omega_q}{\omega_r}. \tag{2.7}$$

The design choice also needs to consider the readout time (see appendix B for more details).

Finally the phononic coupling can span over many orders of magnitude depending on the substrate nature. For piezoelectric substrates, γ_{pn} is directly related to the electromechanical coupling K^2 (see section 2.4). On nonpiezoelectric substrates, this coupling is negligible. In **Paper B** we measure this quantity for superconducting resonators realized on gallium arsenide.

When we plot the total decay rate Eq. (2.3) with parameters in our experiments, and assuming all baths in thermal equilibrium, we obtain the curves in Fig. 2.1(b) for circuits fabricated on silicon and Fig. 2.1(c) for the one on gallium arsenide. Identifying and quantifying accurately the main source of loss is then necessary for sample and experiment design.

Finally, the model used in Eq. (2.1) assumes the constituents of the baths being independent. A more detailed treatment may include interacting two-level systems [76], or correlated noise in the coaxial cables. We did not use these refinements in the data analysis of our experiments.

2.2 Two levels systems

In this section we present the effects of the TLS baths on the circuits we fabricated, describing the main finding in **Paper A**, **Paper C** and **Paper E**.

2.2.1 Qubit decoherence statistic

In **Paper A** we investigate the decoherence in two fixed frequency transmon qubits dispersively coupled to a read-out resonator. These qubits are fabricated on silicon (see appendix C for more details on the fabrication process), bonded with aluminum wires in two separated sample boxes and measured at the same time. The qubits, with frequencies $\omega_a/2\pi = 4.437\,\mathrm{GHz}$ and $\omega_b/2\pi = 3.759\,\mathrm{GHz}$, are driven through their resonators by applying the pulse schemes showed in appendix B. By measuring the decay and dephasing rates for many hours we obtain significant statistics of the fluctuations.

We noticed that 5% of the decay measurements presented a revival, and, in fewer instances, the relaxation rate switched between two separate values while being measured. It has been shown also in other papers that the frequency of the TLSs fluctuates [77, 78], and we believe that in this case we observe a resonant interaction with a single TLS. From the resonant oscillations, we can extract the coupling with the single TLS, $\gamma_{\mathrm{tls}}/2\pi = 4.8\,\mathrm{kHz}$.

In Fig. 2.2(a) we report the decay rates from level $|e\rangle$ and $|f\rangle$ as a function of time for one of the two qubits measured in the paper. While in Fig. 2.2(b) we display the free induction decay rate, T_2^*, measured with a Ramsey sequence. The fluctuations of the decay rates affects the performance of any device; for example, in **Paper III** it directly affects the stability of the single photon source. Therefore, we usually quote the average values with their variances. In Fig. 2.2(c) and (d) we build the histograms of the series reported in (a) and (b), respectively. With our fabrication process, the qubit realized on silicon have a lifetime of $\bar{T}_1 = 50\,\mu\mathrm{s}$, while $\bar{T}_2^* = 95\,\mu\mathrm{s}$.

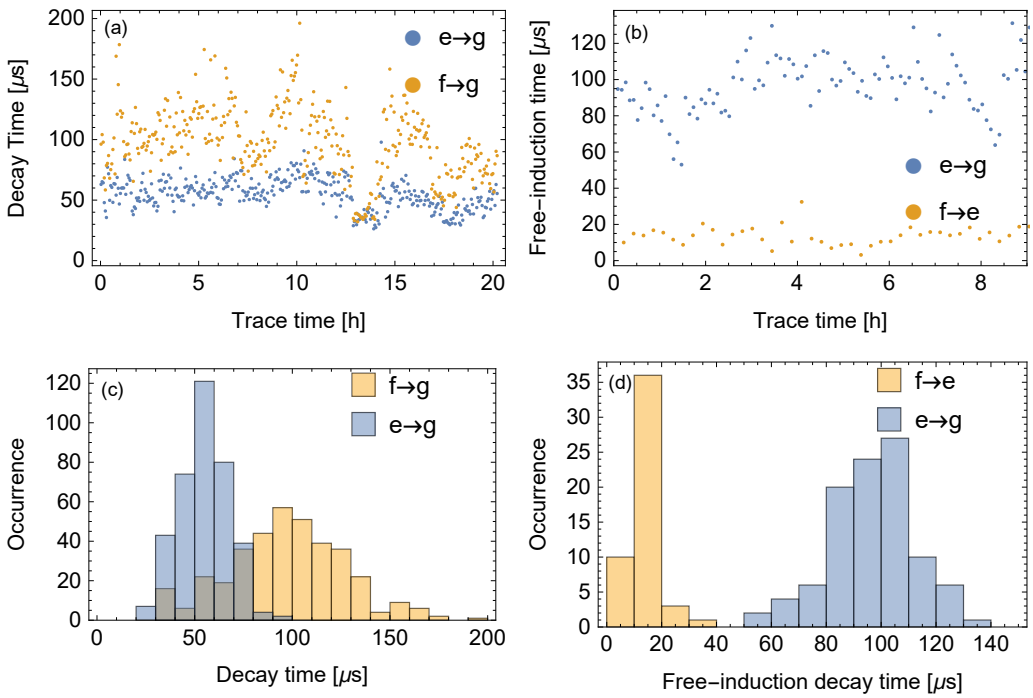

Figure 2.2: *Decoherence statistics. (a) Total decay rate of the qubit, from the level $|e\rangle$ and $|f\rangle$. (b) Free induction decay measured with a Ramsey sequence, for the qubit first and second excited state. (c) and (d) Histograms of the decay rate measured in (a) and (b), respectively.*

The Allan deviation [79] of the temporal series of the decay rates, shows a peak that cannot be obtained by any noise with a power law spectrum, while it can be generated by Lorentzian noise. Adding this component, and fitting the data, we found a switching time between 16 min and 3.7 hours.

Finally, we do not measure any significant correlation between the fluctuation of decoherence of the two qubits, ruling out the measurement setup as a possible source of this Lorentian noise.

2.2.2 Qubit population

Calculating the steady state in Eq. (2.1), the population of the first excited state of the qubit is given by the average of the populations of its surrounding baths weighed by their coupling rates

$$P_e = \frac{\gamma_{\mathrm{ph}} n_{\mathrm{ph}} + \gamma_{\mathrm{pn}} n_{\mathrm{pn}} + \gamma_{\mathrm{tls}} n_{\mathrm{tls}} + \gamma_{qp} n_{\mathrm{qp}}}{\gamma}. \tag{2.8}$$

For qubits fabricated on silicon the phononic component does not have an appreciable contribution. Moreover, at 10 mK the quasiparticles population is negligible. If we also ignore nonequilibrium quasiparticles, the qubit population is

$$P_e = \frac{\gamma_{\mathrm{ph}} n_{\mathrm{ph}} + \gamma_{\mathrm{tls}} n_{\mathrm{tls}}}{\gamma}. \tag{2.9}$$

As we already mentioned, the photonic and TLS baths are not in thermal equilibrium with the thermometer on the mixing chamber plate. In fact, measuring the population of P_e as a function of the mixing chamber plate temperature [see Fig. 2.3(a)] shows the present of a heat source that warms up the qubit.

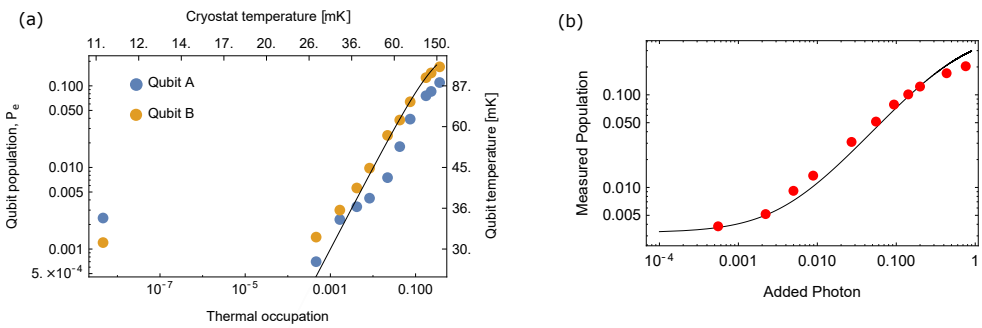

Figure 2.3: *Qubit population. (a) Population of qubit A and B (see paper A) as a function of the mixing chamber plate temperature. The black solid line represents the population of the transmon (with 4 levels included in the calculation). (b) Population of qubit A as a function of added photon in the coaxial line. The black solid line represents the best fit of Eq.* (2.9) *to the data.*

In the draft of **Paper E** we study the effects of different input set-ups on the population

P_e and the decay rate γ of the qubit for five different configurations, with different total attenuation, filtering and connector types.

Moreover we use calibrated white noise to increase the photon occupation in the line n_{ph}. From the population and decay measurement, we extract the coupling with the TLS bath, with the preliminary value of $\gamma_{\mathrm{tls}}/2\pi = 2\,\mathrm{kHz}$ comparable with the one measured in **Paper A**. At the same time we extract the occupation of the TLS bath, $n_{\mathrm{tls}} = 0.65\,\%$, corresponding to a temperature 42 mK for the qubit A. Although additional investigations are necessary to identify and possibly remove the source(s) of the heating, the full characterization of the qubit environments can help design future experiments and improve the understanding of the present ones.

2.2.3 Saturating TLSs bath

For a coherent drive with $n \gg 1$, Eq. (2.6) becomes [80]

$$\gamma_{\mathrm{tls}} = \omega_r F \delta_{\mathrm{t}} \frac{\tanh\left(\frac{hf_r}{2k_B T}\right)}{\sqrt{1+\left(\frac{n}{n_c}\right)^{\beta}}}, \tag{2.10}$$

where n_c is the critical photon number and β is a phenomenological parameter[1]. The loss due to TLSs vanishes when they are saturated.

In **Paper C** we exploit the high finesse of a SAW resonator (described in section 1.4.3) to saturate the TLSs bath with a coherent tone (pump) while probing the internal quality factor of a neighboring mode. The variation $\delta(1/Q_{\mathrm{tls}})$ of TLSs contribution to the quality factor for a pump with strength Ω and detuned by Δ from the probe mode with frequency ω_r, depends on the ratio [81]

$$\xi = \frac{\Delta^2}{\Omega^2} \tag{2.11}$$

and is given by

$$\delta\left(\frac{1}{Q_{\mathrm{tls}}}\right) = -F\delta_{\mathrm{t}} \tanh\left(\frac{hf_r}{2k_B T}\right)\left\{1+\xi\left[6+3\sqrt{1+2\xi}\,\ln\left(1+\xi\left(1-\sqrt{1+2\xi}\right)\right)\right]\right\}. \tag{2.12}$$

We observe a reduced loss from TLSs up to 90% for pump powers with $n \approx 10^5$ photons. This result opens a new direction in reducing losses from TLSs. Realizing devices that saturate the TLSs bath with mechanical excitation could be used on nonpiezoelectric substrate, to mitigate the energy loss of superconducting resonators limited by TLSs.

2.3 Photons

The expected occupation of microwave modes in the coaxial lines in our cryostat can be estimated by knowing their attenuation profile and filtering (see appendix A). Nevertheless the presence imperfections, high-frequency leakages or nonperfect thermalization of

[1] In the Standard Tunelling Model (STM) for two-level systems $\beta = 1$.

the microwave components may alter the average photon occupation by many orders of magnitude.

In **Paper D** we probe the average photon number of the input lines using a superconducting qubit. The qubit is directly coupled at the end of the waveguide line [see Fig. 2.1(a)]. The reflected signal of a coherent driving with strength Ω is shown in Fig. 2.4(a).

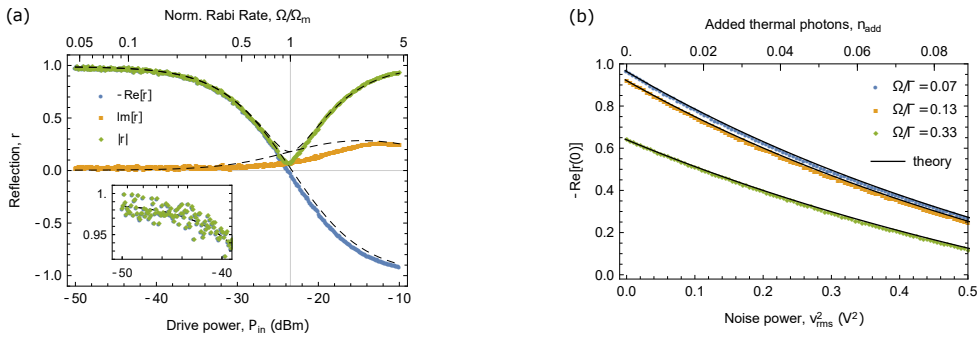

Figure 2.4: *Coherent scattering from the thermometer. (a) Real (blue), imaginary (orange) and absolute value (green) of the reflection coefficient as a function of the coherent probe power. (b) Real part of the reflection coefficient as a function of added thermal photons for three probe powers.*

In order to calculate the scattering property, we modify the master equation Eq. (2.1), considering a driven three level atom, so that Eq. (1.33) in the rotating frame with the driving frequency ω_d reads

$$\hat{H}/\hbar = -\delta\hat{b}^\dagger\hat{b} - \frac{E_C}{2}\hat{b}^\dagger\hat{b}^\dagger\hat{b}\hat{b} + i\frac{\Omega}{2}(\hat{b} - \hat{b}^\dagger). \tag{2.13}$$

Moreover we neglect the phononic and quasi-particles contribution, as well as TLSs bath population. Solving for the steady state and applying the input-output relation, we obtain the reflection coefficient for resonant driving (see Paper D for the calculation details)

$$r(0) = -1 + \frac{8n_{\mathrm{ph}}^{ge} + 4n_{\mathrm{ph}}^{ef}}{1 + 3i\gamma_{\mathrm{ph}}/(2E_C)} + 4\frac{\gamma_\phi}{\gamma_{\mathrm{ph}}} + 2\frac{\gamma_{\mathrm{tls}}}{\gamma_{\mathrm{ph}}} + \frac{4(\Omega/\gamma_{\mathrm{ph}})^2}{1 + i\gamma_{\mathrm{ph}}/E_C} \tag{2.14}$$

In order to use the qubit as a thermometer, we mitigate the effect of the TLSs designing a large photonic coupling: $\gamma_{\mathrm{ph}} \gg \gamma_{\mathrm{tls}}$. In this regime, considering that $n_{\mathrm{ph}}^{ge} \approx n_{\mathrm{ph}}^{ef}$, the reflection coefficient becomes

$$r(0) = -1 + \frac{12}{1 + 3i\gamma_{\mathrm{ph}}/(2E_C)}n_{\mathrm{ph}} + \frac{4(\Omega/\gamma_{\mathrm{ph}})^2}{1 + i\gamma_{\mathrm{ph}}/E_C}. \tag{2.15}$$

Eq. (2.15) shows that the reflection coefficient at low driving strength, is linear with the thermal photons in the line. Moreover this thermometer does not need to be calibrated against another one.

In Fig. 2.4(b) we measure calibrated white noise to artificially increase the photonic thermal bath in the waveguide for three driving strengths. We have a perfect agreement between data and theory.

In the follow-up experiment, we show a time resolved measurement of the photon number with a response in less than 7 ns. The sensitivity for our thermometer, estimated to be $4 \cdot 10^{-4}$ photons/$\sqrt{\text{Hz}}$, can be further improved with a better amplification chain.

2.4 Phonons

Eq. (2.8) shows that the phononic bath effectively cools the qubit. The better the cooling the smaller is the error in resetting the qubit that we implement by simply waiting longer than the qubit decoherence times[2]. Unfortunately, a large coupling may degrade the performance of the circuits. In fact, when the superconducting circuits are fabricated on a piezoelectric substrate, their electromagnetic excitation can be directly converted in a mechanical one due to the electromechanical coupling. The phonon coupling γ_{pn} cannot be calulated analytically, but can be estimated numerically for each specific geometry.

2.4.1 Piezoelectric effect

On a piezoelectric material, any time dependent electric field generates mechanical waves. The energy flows away from the superconducting circuits at the speed of sound, and the amount depends on the material (by the electromechanical coupling), on the frequency and on the geometry of the device. The geometry of some devices, for example SAW filters [42], is designed to achieve the largest conversion efficiency possible.

Hooke's law for a nonisotropic material linearly relates the stress σ_{ij} and the strain s_{kl}

$$\sigma_{ij} = c_{ijkl} s_{kl}, \tag{2.16}$$

where c_{ijkl} is the elastic constant, and we used Einstein notation of the sum over the indices. Piezoelectric materials generate an electric field when subject to strain, due to the lack of symmetry for inversion respect to the center of the crystal unit cell [82]. In the same way, an electric field E_k produce a strain in the material. In this case, we can rewrite Eq. (2.16) and add the effect of the strain on the electric field [83]

$$\sigma_{ij} = c_{ijkl} s_{kl} - e^T_{ijk} E_k, \tag{2.17}$$

$$D_i = e_{ijk} s_{jk} + \epsilon_{ij} E_j \tag{2.18}$$

where we introduced the piezoelectric coefficient e_{ijk} and the material permittivity ϵ_{ij}.

The wave equation for the deformation u_i and for the electric potential V are given by [84]

$$d_{\text{m}} \partial_t^2 u_i - c_{ijkl} \partial_j \partial_l u_k = e_{kij} \partial_j \partial_k \phi, \tag{2.19}$$

$$\epsilon_{ij} \partial_i \partial_j V = e_{ijk} \partial_i \partial_k u_j. \tag{2.20}$$

[2] As we saw, this introduces a small systematic error on the qubit state, because the qubit relaxes to the mixture $\hat{\rho} = P_g |g\rangle\langle g| + P_e |e\rangle\langle e|$

where d_{m} is the density of the piezoelectric material. Planar waves are solutions of the Eq. (2.19) and Eq. (2.20). For each direction of propagation, the voltage wave is completely determined by the coefficients of the mechanical ones. In particular the effective elastic coefficient becomes

$$c'_{ijkl} = c_{ijkl}(1 + K^2_{ijkl}), \tag{2.21}$$

where we introduced the electromechanical coupling for a wave propagating in direction (x_1, x_2, x_3) [84]

$$K^2_{ijkl} = \frac{e_{mij} e_{nkl} x_m x_n}{c_{ijkl} \epsilon_{pq} x_p x_q}. \tag{2.22}$$

The positive value of the electromechanical coupling, implies that a piezoelectric material is "stiffer" than it would be without the piezoelectric effect.

In **Paper B** we fabricated superconducting coplanar waveguide resonators on gallium arsenide, whose crystal presents a cubic lattice. With this symmetry there are only three independent elements in the elastic tensor [82]. In general, the elastic tensor in the Voigt notation is

$$c_{ij} = \begin{pmatrix} c_{11} & c_{12} & c_{12} & 0 & 0 & 0 \\ c_{12} & c_{11} & c_{12} & 0 & 0 & 0 \\ c_{12} & c_{12} & c_{11} & 0 & 0 & 0 \\ 0 & 0 & 0 & c_{44} & 0 & 0 \\ 0 & 0 & 0 & 0 & c_{44} & 0 \\ 0 & 0 & 0 & 0 & 0 & c_{44} \end{pmatrix}, \tag{2.23}$$

the piezoelectric tensor

$$e_{ij} = \begin{pmatrix} 0 & 0 & 0 & e_{14} & 0 & 0 \\ 0 & 0 & 0 & 0 & e_{14} & 0 \\ 0 & 0 & 0 & 0 & 0 & e_{14} \end{pmatrix}, \tag{2.24}$$

and the dielectric tensor

$$\epsilon_{ij} = \begin{pmatrix} \epsilon_{11} & 0 & 0 \\ 0 & \epsilon_{11} & 0 \\ 0 & 0 & \epsilon_{11} \end{pmatrix}. \tag{2.25}$$

The deformation produced by an electric field on such anisotropic substrate is difficult to visualize using the tensor formalism. In Fig. 2.5 we report the effect 1 V potential applied to opposite faces of a 1 μm cube of gallium arsenide, oriented in different directions.

For the orientation used in Fig. 2.5(b), we notice that the angles are not preserved. SAW resonators with an orientation parallel to the faces of this cube do not work. For our fabrication process we always orient the devices parallel to the faces shown in Fig. 2.5(c). In this case the deformation is perpendicular to the direction of the applied electric field. Unfortunately, our alignment relies on the wafer cut (see appendix C), so our device suffers from beam steering losses [42, 85].

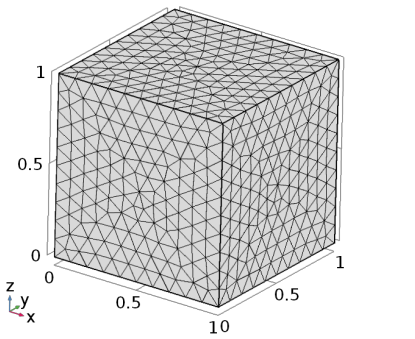

(a) *No electric field applied, cube faces: (100), (010) and (001)*

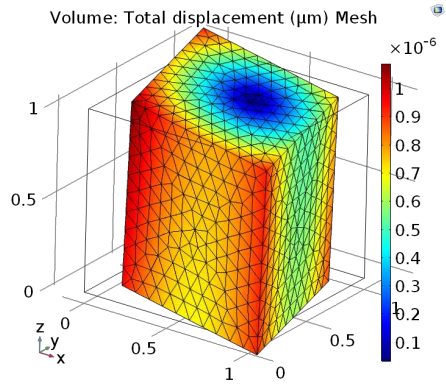

(b) *Electric field applied*

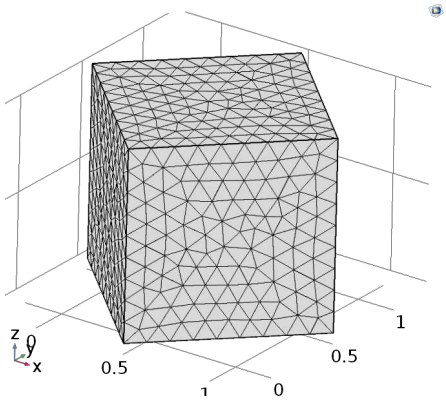

(c) *No electric field applied, cube faces (110), ($\bar{1}$10) and (001)*

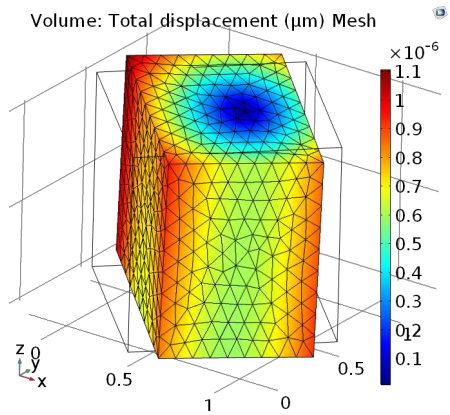

(d) *Electric field applied*

Figure 2.5: *Numerical calculation of equilibrium solution for a GaAs cube of 1μm side subject to electric field. An electric potential of 1V is applied to the top face with respect of the bottom one; this produces an electric field along the z direction, that induces a mechanical deformation. Because of the symmetry a voltage of -1V generates a displacement with opposite sign. The color scale shows the total displacement from the original position. The deformation has been amplified 10^6 times to make it visible.*

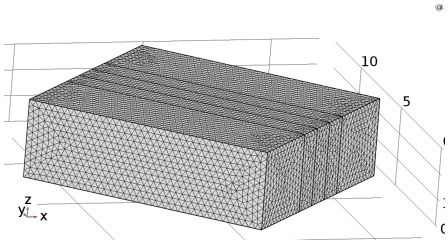

(a) *No electric field applied, center conductor direction (110)*

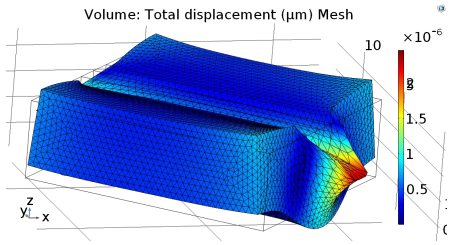

(b) *Electric field applied*

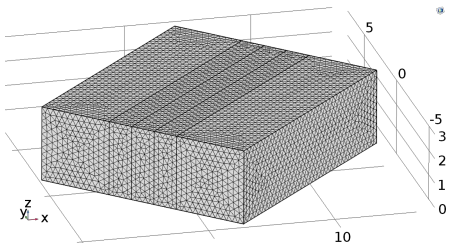

(c) *No electric field applied, center condutor direction ($\bar{1}10$)*

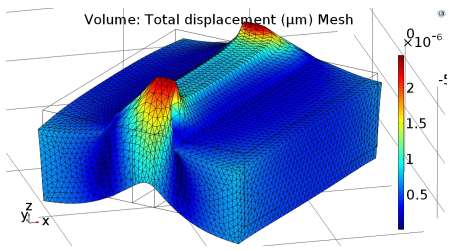

(d) *Electric field applied*

Figure 2.6: *Numerical calculation of equilibrium solution for a coplanar waveguide structure on a GaAs substrate subject to electric field. The electric differential of potential applied on the central conductor and on the ground plane produces an electric field confined in the XY plane far away from the edge. The mechanical deformation is amplified 10^6 times to make the effect visible. The colorscale shows the total displacement from the original position.*

2.4.2 2D simulations

In **Paper B** we numerically solve the system of piezoelectric and electrostatic equations with a finite element solver (COMSOL, piezolectric module).

In Fig. 2.6 we see the effect of a static potential between inner conductor and the ground plane on a coplanar waveguide structure. The waveguide is oriented in the directions (110) or ($\bar{1}$10), the same followed in the fabrication of our device. In order to simulate the intra-resonator electric field at different frequencies, we apply an oscillating potential.

The phase velocity of mechanical waves on the surface and in the bulk of GaAs goes from 3 to 6 km/s, implying a wavelength between 500 nm and 1 μm for microwave frequencies. Unfortunately, only a fraction of the total geometry, as the one shown in Fig. 2.6 can be simulated in the GHz regime, because of the fine meshing needed for a correct discretization of the mechanical wave. We restrict our simulation to a two-dimensional layer of gallium arsenide, and we rotate the elastic and piezoelectric tensor to reproduce the material orientation used in the experiment[86].

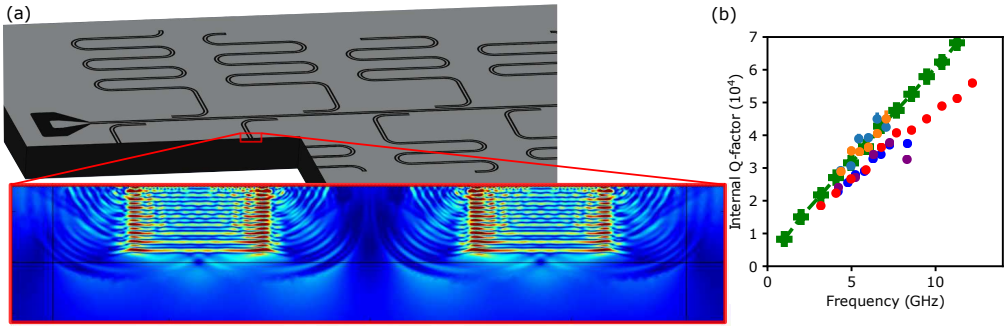

Figure 2.7: *Simulation of the internal Q-factor of resonators. (a) Two-dimensional geometry simulated. The color scale represents the displacement of the GaAs from its resting position. (b) Simulated value of the internal quality factor (green crosses) compared with the one measured in the experiment (red, orange and blue indicate different samples).*

The simulation shows the generation of mechanical waves (with more than 95% corresponding to bulk acoustic modes) when an oscillating field is applied between the two electrodes. The displacement, represented by the color scale in Fig. 2.7(a) and the velocity of the gallium arsenide are used to estimate the fraction ΔU of the total energy U, converted in mechanical waves within one oscillation period. We extract the internal quality factor as

$$Q_i = 2\pi \frac{U}{\Delta U}, \tag{2.26}$$

reported in Fig. 2.7(b) in green. This agrees well with the measured resonators Q-factors covering a range of 10 GHz.

Varying the probe power and the temperature of the mixing chamber plate, we measure the TLS and quasiparticle contribution to the total loss. We determine that the average TLS loss account for 14% of the total loss on the substrate, while the quasiparticles loss is negligible at 10 mK (see **Paper B** for more details).

–You Shall Not Pass!

Gandalf, The Fellowship of the Ring (2001)

3

Quantum emitters in structured electromagnetic environment

In chapter 2 we presented the effects of different baths on superconducting resonators and qubits. In those experiments, the degrees of freedom of the environment are treated as an ensemble, characterized by only two global parameters (its effective coupling to the system and its population). Moreover, in chapter 1, we saw that placing a quantum emitter in a cavity alters the density of state of the environment affecting its energy (Lamb shift) and its decay rate (Purcell effect). Also in this case, these effects can be treated perturbatively [87].

The introduction of a more structured electromagnetic environment, such as finite band pass or band gap, alters the energy structure and the dynamics of a quantum emitter [88] beyond any perturbative approximation. In this chapter we concentrate on these effects of such an environment.

3.1 Metamaterials in circuits QED

One dimensional metamaterials realized with superconducting circuits are ideal for engineering on-chip dispersion relation [89]. In many cases, pass and stop bands can be realized exploiting the collective response of a periodic structure. In reference [90], a photonic crystal is obtained modulating the impedance of a coplanar waveguide with a pitch p comparable to the wavelength. In reference [91], a transmission line is periodically loaded, drastically reducing the foot print for the waveguide.

A versatile approach, that combines a reduced footprint and access to full connectivity, is to realize an array of coupled resonators [92] or even qubits [93]. These structures open

a pass band in the photonic spectrum where the propagation of light is much slower compared to the usual CPW geometry, and at the edge of the band, the group velocity vanishes. When an artificial atom is coupled to this localized light [94], its excitation is dressed with a photonic component [95, 96], named an atom-photon bound state[1].

3.1.1 Coupled cavity array

In **Paper F** we realized a slow light waveguide with an array of capacitively coupled high impedance JJ resonators (see section 1.4.2 for more details regarding the resonators). Initially, we fabricate the array without any qubit. In Fig. 3.1(a) we show a micrograph of a sample realized to test the bare array, where 21 resonators are capacitively coupled with their neighbors and at the edges with coplanar waveguides. In order to test the full structure, we leave the "ghost" electrodes for the qubits and their control. Importantly, once the qubits are fully fabricated, the electromagnetic environment and ground plane will not be perturbed. In Fig. 3.1(b) we display the details of these floating structures. The $7 \times 5\,\mathrm{mm}^2$ chip is wire-bonded in a 4-port sample holder (see appenix A for details).

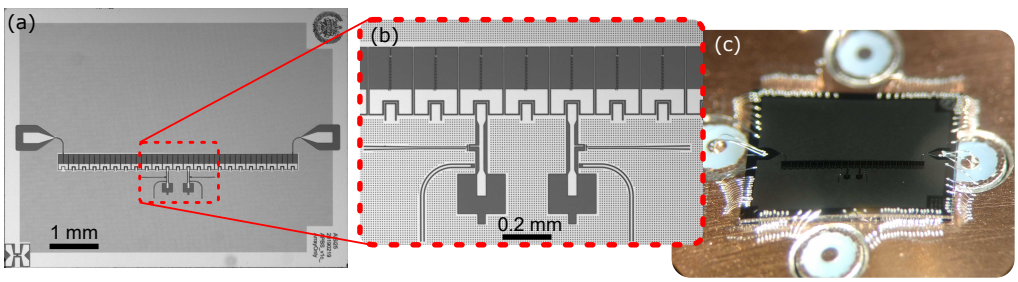

Figure 3.1: *Couple cavity array. (a) The slow light waveguide is realized with 21 resonators capacitively coupled. The sample is realized in aluminum (light color) on silicon (darker color). (b) Micrograph of the "ghost" electrodes of the qubits and their control lines. (C) Sample wirebonded in a 4-port sample holder.*

3.1.2 Array modes and band pass

In Fig. 3.2(a) we report the full circuit model where the JJ resonator has 10 junctions each. The first array mode for an individual resonator has a frequency $\omega_r/2\pi \approx 5.7\,\mathrm{GHz}$, while the second mode is pushed above 30 GHz by the large capacitance (see section 1.6). Restricting the excitation frequency in the system below this threshold, we can simplify our model, substituting the JJ array with a single equivalent inductor, as shown in Fig. 3.2(b).

The values of the capacitances showed in the circuits are simulated solving the Poisson equation in a FEM solver (COMSOL, electrostatic module). The Lagrangian of the circuit

[1] This phenomenon is analogous to the presence of a localized electronic state, seeded by an impurity, between two conduction bands in a semiconductor[30].

$$\mathcal{L} = \frac{1}{2}\dot{\mathbf{\Phi}}^T \mathcal{C}\dot{\mathbf{\Phi}} - V \tag{3.1}$$

where $\dot{\mathbf{\Phi}}^T = (\dot{\Phi}_{q1}, \dot{\Phi}_{q2}, \dot{\Phi}_1, ..., \dot{\Phi}_N)$ and

$$V = \sum_i \frac{\Phi_i^2}{2L_i}, \tag{3.2}$$

and $\mathcal{C}$ is the tridiagonal capacity matrix, with C_r on the main diagonal and $-C_J$ for the first off diagonal elements. From the Lagrangian we can calculate the Hamiltonian

$$\hat{H}_{\mathrm{CCA}}/\hbar = \omega_r \sum_{l=1}^{N} \hat{a}_l^\dagger \hat{a}_l + J \sum_{l=1}^{N-1} \left(\hat{a}_{l+1}^\dagger \hat{a}_l + \hat{a}_l^\dagger \hat{a}_{l+1} \right) \tag{3.3}$$

where $\omega_r = 1/\sqrt{L_r(C_r + 2C_J)}$ and $J = \omega_r \frac{C_J}{2(C_r+2C_J)}$.

The eigenvalues of $\hat{H}_{\mathrm{CCA}}$ in the single excitation subspace are reported in Fig. 3.2(c). Their frequency distribution becomes denser at the edge of the band, while the modes are more spaced at the center of the band.

Solving the Heisenberg equation with input-output theory to the resonators at the edge of the array, we can calculate the expected transmission of the waveguide. The results of this calculation are reported in Fig. 3.2(c). Each peak in the transmittance, corresponds to one of the modes. In Fig. 3.2 (Mode 1), we report the mode structure for the first (lowest frequency) array mode. The y-value in the plot represents the voltage distribution at the resonator nodes. Note, that this mode is the mode with the largest k vector (or equivalently with the shortest wavelength). On the opposite extreme, in Fig. 3.2 (Mode 21), the last mode at the highest frequency, presents the longest wavelength. This behavior is a property of the Left-handed metamaterial [89]. As we mentioned in section 1.3, our waveguide is a composite left-right handed metamaterial.

The coupled cavity array can carry more than a single excitation. Fig. 3.3(a) shows the bands beyond the single excitation subspace.

With the parameters used in our design, a photon in the first three bands does not excite the second array mode of the individual resonators. The band can be probed measuring the transmission of a coherent tone. Comparing Fig. 3.2(c) and 3.3(b), we notice a nonzero transmission outside the band. This behavior (even more pronounced in the sample bonded in the 8-port sample holder) is attributed to cross talk (as described in the appendix of **Paper F**).

3.2 Quantum emitters in slow-light waveguide

In **Paper F** we capacitively couple two frequency tunable transmon qubits to site 10 and 12 of the resonator chain. Each qubit has a charge and a flux line, and an individual read-out resonator.

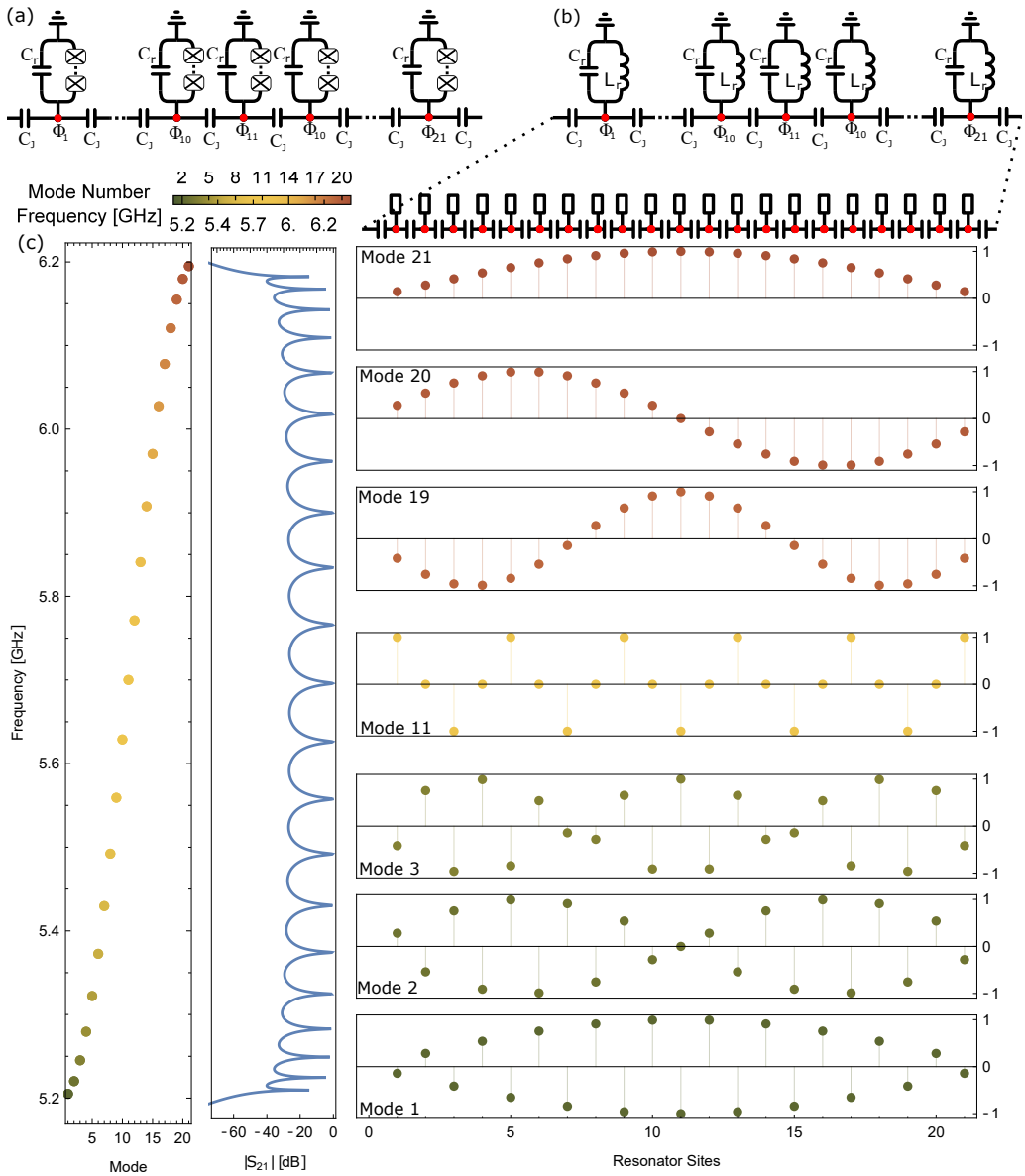

Figure 3.2: *Electric model, transmission and mode structure of the coupled cavity array. (a) Complete electrical model including the 10 JJs for each resonator. (b) Simplified electrical model with a single equivalent inductor that substitute the JJs arrays. (c) The coupled resonators hybridize in 21 modes with different frequencies. They can be probed by coherent spectrocopy. The left hand metamaterial produces modes with lower frequency at larger wavenumbers.*

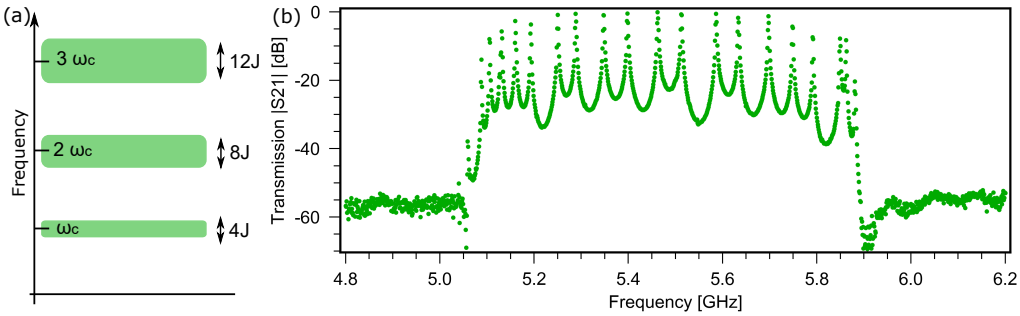

Figure 3.3: *Band structure. (a) Energy diagram for the first three excitation subspaces of the coupled cavity array. (b) Coherent transmission through the waveguide in the first excitation subspace.*

3.2.1 Hamiltonian of the system

Fig. 3.4(a) shows the complete device realized for the experiment. Comparing it with the sample shown in Fig. 3.2, we added JJ to the qubits and connected their control lines. Moreover the chip has a slightly increased area of $6.6 \times 6.6\,\mathrm{mm}^2$. The increased number of ports results in longer wirebonds [see Fig. 3.4(b)] with an effective larger cross talk that needs to be taken into account to describe the data accurately.

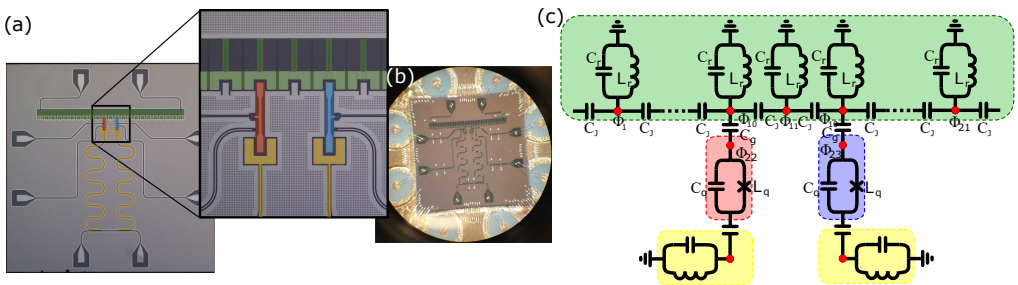

Figure 3.4: *Two artificial atoms in a waveguide. (a) Micrograph of the sample in false colors. The two transmons (in blue and red), the resonator array (in green) and the read-out resonators (in yellow) are highlighted in the zoomed region. (b) The sample is wirebonded in an 8-port sample box. (c) Equivalent circuit model with the same color code for each component.*

Fig. 3.4(c) shows the full circuit model including transmon qubits and read-out resonators. From the Lagrangian of the circuits we can derive the Hamiltonian

$$
\begin{aligned}
H/\hbar = &\sum_{l=1}^{N} \omega_r \hat{a}_l^\dagger \hat{a}_l + \sum_{l=1}^{N-1} J\left(\hat{a}_l^\dagger \hat{a}_{l+1} + \hat{a}_{l+1}^\dagger \hat{a}_l\right) \\
&+ \sum_{i=1}^{2} \omega_{qi} \hat{b}_i^\dagger \hat{b}_i + \frac{1}{2}\beta_i \hat{b}_i^\dagger \hat{b}_i^\dagger \hat{b}_i \hat{b}_i + g_i\left(\hat{a}_{l_i}^\dagger \hat{b}_i + \hat{b}_i^\dagger \hat{a}_{l_i}\right),
\end{aligned}
\tag{3.4}
$$

where the cavity-atom interaction is given by

$$g_i = \langle 1|Q_{qi}|0\rangle \frac{C_{gi}}{V_{qi}} \sqrt{\frac{\omega_r}{2(C_r + 2C_J)}}, \qquad i \in \{1, 2\} \tag{3.5}$$

where $Q_{qi} = \sqrt{\hbar(C_q + C_g)\omega_q/2}\left(\hat{b}^\dagger + \hat{b}\right)$.

3.2.2 Atom photon bound state

If we consider only one bound state, and we approximate the semicontinuum of modes to a band with the same dispersion relation, the energy of the bound state $\hbar\omega_{BS}$ can be analytically determined by the roots of the algebraic equation

$$\omega_{BS} - \omega_q = \frac{g^2}{(\omega_{BS} - \omega_r)\sqrt{1 - \frac{4J^2}{(\omega_{BS} - \omega_r)^2}}} \tag{3.6}$$

The spectroscopy of the bound state for a single qubit is shown in Fig. 3.5(a). The bound state asymptotically approaches the band edge, becoming the last band mode when the bare qubit frequency crosses the pass band. In fact, Eq. (3.6) admits two solutions, two bound states, one above and one below the pass band. Nevertheless, the total number of modes in the system will not exceed the number of resonators plus the qubit. So when the lower bound state emerges from the band, the upper one, becomes the last mode of the bare array.

The photonic cloud seeded by the atom coupled to position 10 is displayed in Fig. 3.5(b). It shows the population in each resonator as a function of the bare qubit frequency. The logarithmic scale used for the population highlights the exponential localization already present when the qubit is well outside the band. The closer the qubit becomes to the center of the band, the larger the extension of the cloud becomes.

In **Paper F** we also access the two-excitation bound state, measuring its frequency as a function of the bare qubit frequency.

3.2.3 Two bound states interacting

When two bound states are present, their photonic clouds overlap. In this case, the interaction is mediated by the resonators array. Compared with the dispersive interaction obtained in a resonators, where the residual interaction decreases algebraically $\sim g^2/\Delta$ with the qubit detuning (infinite range interaction), the exponential decay of the clouds suppresses the residual interaction (finite range interaction).

In our experiment, we measure the interaction of the two bound states mediated by the photonic excitation in the resonators. The accurate description of this interaction accounts for next-nearest neighbor coupling for inter-cavity and cavity-qubit. We measure interaction strength up to 52 MHz.

Finally we use the bound state interaction, to implement a SWAP-operation of their excitation. The swap time varies with the cloud overlap; we measured a complete SWAP in 18 ns.

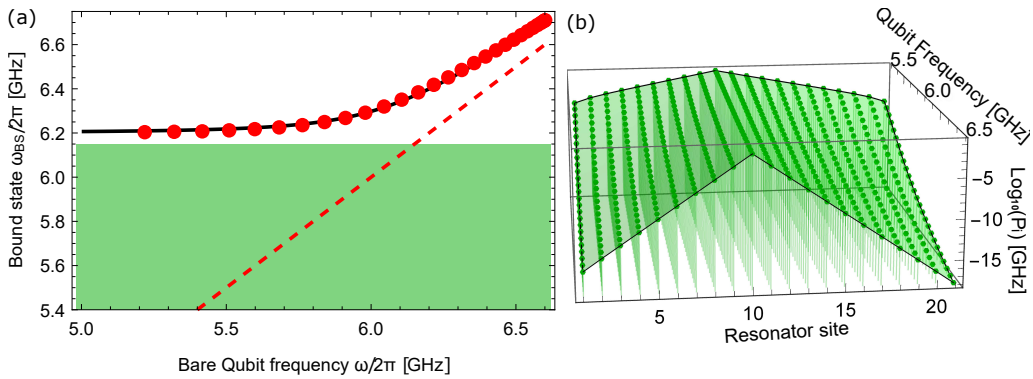

Figure 3.5: *Single atom-photon bound state. (a) Frequency of the bound state as a function of the bare qubit frequency. The data (red dots) agree very well with the theoretical prediction (solid black line). The green region represents the passband and the dashed red line is the qubit bare frequency. (b) Expected population of the resonators as a function of bare qubit frequency.*

This work, or many of its parts, can have applications in cQED. The slow-light waveguide can be a useful tool in bath engineering: it presents a small nonlinearity that can be tuned by design. Moreover, modifying the parameters of the resonators, the second array mode can enrich the band structure. The full architecture can be used for experiments in nonlinear photon transport [97], or quantum simulation of spin.

–"Yo, Adrian, we did it. We did it."
Rocky Balboa, Rocky II (1979)

4 Summary

In this thesis we discussed the effects of the environment on quantum systems implemented with superconducting circuits.

In the first chapter, we introduced the circuit quantum electrodynamics, deriving the Lagrangian and the Hamiltonian of the elementary circuits later used in the thesis.

In the second chapter, we investigated the effects of different baths on a superconducting circuit. We showed that the coherence of the qubits we fabricated is mainly limited by a bath of two-level systems. We studied the thermal properties of the photonic bath in highly attenuated coaxial lines in the cryostat, showing how a qubit strongly coupled to this photonic bath, can be used as a primary thermometer. Moreover we investigate the spurious coupling of superconducting resonators with mechanical loss channel.

In the third chapter we introduced a metamaterial for cQED, that opens a passband in the photonic spectrum. Moreover, we showed how this colored vacuum affects the energy structure of a quantum emitter. Finally we describe the experiments with two bound states.

These experiments demonstrate important effects of the environment in cQED, from a simple perturbation of the expected behavior of the system to a completely new treatment. Our results can have application in cryogenic setup optimization, as well as bath engineering and quantum simulation.

In **Paper A**, the relaxation and dephasing mechanisms in superconducting qubits are studied. Two qubits (A and B) are mounted in two different box enclosures and the decoherence times T1 and T2 are measured every three minutes for 60 hours. This is repeated in multiple cooldowns. The variation of the decoherence is statistically analyzed. The decoherence is attributed to two-level systems on the substrate surface.

In **Paper B**, coplanar waveguide resonators are used as proxies for superconducting devices on gallium arsenide. The losses are investigated by measuring the internal quality factor from 3 to 12 GHz. A linear increase of the quality factor is found as a function of frequency. This behavior is quantitatively explained with the electromechanical conversion of photons in the resonators into mechanical waves in the substrate. By measuring the two-level system and quasiparticle contributions to decoherence, it is shown that the main loss channel is electromechanical conversion into acoustic phonons and that bulk phonons dominate over surface phonons.

In **Paper C**, a high-finesse, surface-acoustic-wave resonator is used to study and saturate two-level systems. In particular, it is shown that the quality factor of a probe mode measured at low power ($n \approx 1$) strongly depends on the pump power of a neighboring mode. The two modes, interact with the same TLS bath, saturating the bath and causing the increase in quality factor.

In **Paper D**, we demonstrate how a superconducting qubit, directly coupled to a waveguide, can perform primary thermometry of the thermal population of propagating photons. The thermal photons disrupt the scattering of a coherent tone to the qubit; from the continuous measurement of the reflection coefficient, the temperature of the waveguide can be extracted. The population of the wave guide is set either by artificial calibrated noise or by heating the mixing chamber plate.

In **Paper E**, the population of the first excited level, the decay and dephasing rates of a superconducting qubit are measured with a variable thermal photon population in its driving line. Assuming that the two-level system bath is not affected by the photon population, the temperature of the TLS bath and its coupling to the qubit is extracted.

In **Paper F**, the potential of the atom-photon bound states for quantum simulations is demonstrated. The architecture consists of a coupled cavity array implemented with high impedance Josephson junction resonators and two transmon qubits capacitively coupled to the array. The first and second excitation subspace of the system is explored spectroscopically, and a time resolved energy SWAP operating between the two bound states is demonstrated.

–Roads? Where We're Going, We Don't Need Roads
Dr. Emmett Brown, Back to the future part II (1989)

A

Room temperature and cryogenic setup

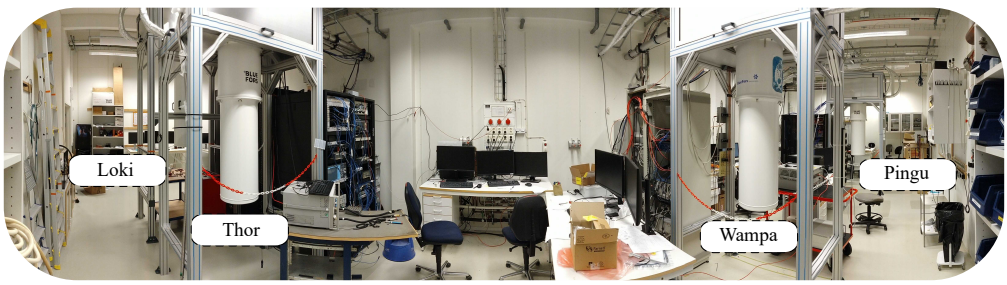

Figure A.1: *Low temperature laboratory where parts of the measurements were performed. In the figure we can recognize four Blue Fors LD 250 with their nicknames highlighted in the tags.*

The experiments reported in this thesis are carried out in quantum regime, i.e. the thermal excitation of the systems is much smaller than one quantum. As mentioned in the introduction we use commercially available dilution refrigerators (similar to the four ones displayed in Fig. A.1) to maintain the devices in this regime. In this appendix we describe in detail the room temperature and cryogenic setup used for the different experiments. Doing so, we will follow the same path the microwave pulses follow to reach the samples. In particular we describe the pulses generation, we describe the environment in the waveguides where they travel and finally the sample boxes in which the sample is situated.

A.1 Up-down conversion of microwave pulses

The devices used in this thesis are controlled with microwave tones, with frequencies between 3 and 12 GHz. At the time of writing, instruments capable to direct syntheses of amplitude modulated pulses in this frequency range are very expensive. A solution to generate such pulses is mixing a carrier signal generated by a local oscillator (LO) with frequency ω_{LO} with an amplitude modulated envelope signal at an intermediate frequency (IF) ω_{if}. The same is true for Digital to Analog Converter (DAC) in the GHz regime, where we downconvert the signal and digitize with an intermediate sampling rate (around hundreds of MHz).

A.1.1 Mixers

A mixer is a microwave device that "mix" two frequencies. In particular the local oscillator frequency behaves as a switch that does or does not let the signal at the intermediate frequency go through. This double side conversion can be described in Fourier space for a single IF tone:

$$S_{\mathrm{up}} = \cos(\omega_{\mathrm{LO}} t)\cos(\omega_{\mathrm{IF}}) = \frac{1}{2}\cos\left[(\omega_{\mathrm{LO}} + \omega_{\mathrm{IF}})t\right] + \frac{1}{2}\cos\left[(\omega_{\mathrm{LO}} - \omega_{\mathrm{IF}})t\right]. \tag{A.1}$$

Filtering out one of the sideband can be very demanding especially since our devices are frequency tunable and we want to drive in a broad frequency range[1].

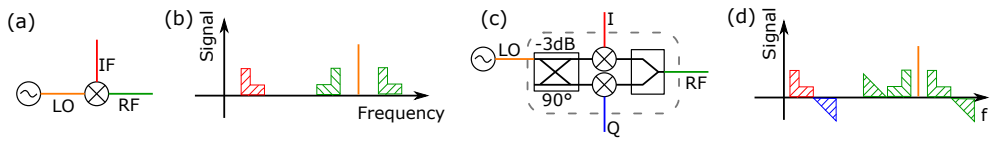

Figure A.2: *Mixer up-conversion. (a) A mixer is a three port passive component. (b) The signal injected at intermediate frequency (IF) port is up-converted by a local oscillator (LO) producing two side bands at the radio frequency (RF) port. (c) An IQ mixer is a 4 ports passive microwave device that can be considered as combination of two mixers driven in quadrature. (d) When the intermediate frequency is applied in quadrature (to I and Q,) one of the low frequency side band is in phase while the high frequency ones destructively interfere.*

In order to eliminate these inconveniences, we use IQ mixers. An IQ mixer is the combination of two mixers driven in quadrature, i.e. with the two LO frequencies shifted

[1] When failing to filter one of the sideband out, the downconverted signal is affect by the interference between two sidebands. Moreover, one of the sideband can drive transitions of the system that were not targeted.

by $\pi/2$, as showed in Fig. A.2(c). Adding the output from the two mixers we get

$$S_{\text{up}} = \cos(\omega_{\text{LO}}t)\cos(\omega_{\text{I}}) + \sin(\omega_{\text{LO}}t)\cos(\omega_{\text{Q}}) = \frac{1}{2}\cos\left[(\omega_{\text{LO}}+\omega_{\text{I}})t\right] + \frac{1}{2}\cos\left[(\omega_{\text{LO}}-\omega_{\text{I}})t\right] + \frac{1}{2}\sin\Big[(\omega_{\text{LO}}+\omega_{\text{Q}})t\Big] + \frac{1}{2}\sin\Big[(\omega_{\text{LO}}-\omega_{\text{Q}})t\Big] \tag{A.2}$$

The I and Q ports are driven by the signal produced by an arbitrary waveform generator (AWG). We usually generate I and Q to be in quadrature. In this case, $\cos(\omega_{\text{Q}}) = \sin(\omega_{\text{I}})$ and the upconverted signal becomes

$$S_{\text{up}} = \cos(\omega_{\text{LO}}t)\cos(\omega_{\text{I}}) + \sin(\omega_{\text{LO}}t)\sin(\omega_{\text{I}}) = \frac{1}{2}\cos\left[(\omega_{\text{LO}}-\omega_{\text{I}})t\right] \tag{A.3}$$

where we only have a single side band (SSB). In principle, we could use only SSB mixers, that would require only a single port of the AWG and digitizer for up- and down-converting our pulses. However that will come at the cost of half of the signal, and loosing the possibility to transmit both sidebands. In addittion it would not be possible to apply DRAG correction (see section B.1.3). For this reason, in our experiments we used IQ mixers.

A.1.2 Downconversion and integration

Without loss of generality, we can focus on the read-out pulse of a qubit coupled to a resonator. The purpose of the experiment is to drive the resonator for a short time (with respect to the lifetime of the qubit) and detect both the in-phase (I) and quadrature (Q) signals. As we mentioned above, in the experiments performed in this thesis we used IQ mixers with IF ports driven in quadrature.

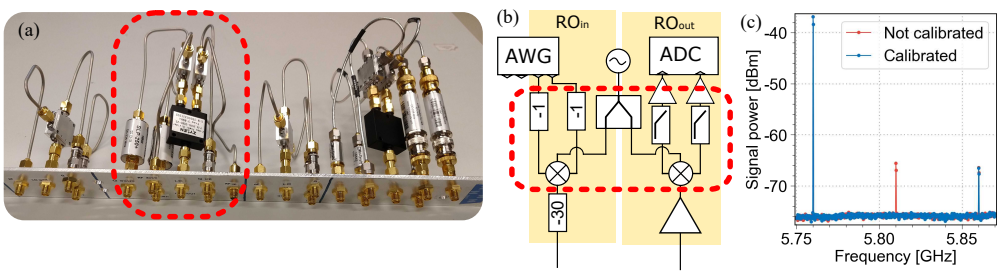

Figure A.3: *Up-down conversion setup. (a) Rack-mounted conversion board realized for a two-qubit setup. The components for qubit read-out are highlighted in the red dashed rectangle. (b) Scheme of the readout components, including an arbitrary waveform generator (AWG) that produces the IF tone and a digitizer (ADC) that records the signal after down-conversion. (c) An example of the up-converted spectrum with IQ mixers calibrated (blue trace) and unbiased (red trace).*

Fig. A.3(a) shows the setup realized in this thesis for the qubit driving, tuning and readout. The aluminum plate ensures a common ground with all the SMA connectors, while the rigid stainless steal coaxial cables, avoid any phase fluctuation induced by involuntary deformation or vibration (touching the cable during the operation). The electrical scheme is shown in Fig. A.3(b).

The demodulated time trace (recorded by the digitizer) consists in a low frequency signal that is digitally processed in the computer. In particular, considering the signal

$$S = \underbrace{I\cos(\omega_0 t)}_{V_1} + \underbrace{Q\sin(\omega_0 t)}_{V_2}, \tag{A.4}$$

we digitally downconvert each trace to DC using $\omega_{\mathrm{IF}} = \omega_0$ and applying a digital low-pass filter

$$X_i = \mathrm{LPFilter}[V_i \cos(\omega_{\mathrm{IF}} t)], \tag{A.5}$$

$$P_i = \mathrm{LPFilter}[V_i \sin(\omega_{\mathrm{IF}} t)]. \tag{A.6}$$

Finally, we recombine the traces

$$A_i = X_i + iP_i, \tag{A.7}$$

and separate the real and imaginary components:

$$A_{\mathrm{tot}} = A_1 + A_2 = X_1 + P_2 + i(X_2 - P_1). \tag{A.8}$$

A.2 Cryostat microwave wiring, filtering and shielding

The coaxial lines that control and read out the superconducting devices realized for this thesis can be summarized in four groups (see Fig. A.4): driving (or charge) lines, they terminate with a direct capacitive coupling to the qubit and they are used for exciting the qubit; flux lines, inductively coupled to the a SQUID, they are used to inject static flux for tuning the frequency of the device, and/or to apply RF signals for parametrically modulating the SQUID; the input/output lines, usually coupled to a secondary device (a resonator), they are used for exciting and measuring the scattered signal. Finally superconducting twisted pairs with low pass RC filters at the 3 K stage (see Fig. A.4) are used for driving superconducting coils at the mixing chamber stage.

A.2.1 Nonthermal photon distribution in the coaxial line

The specific measurement setup used in each experiment is reported in the appended papers. Here we describe the general structure of these lines in terms of attenuation profile and filtering (see Fig. A.4). Moreover, we report the photon occupation distribution profile for the most attenuated line compared with the thermal distribution of the relative stages (solid and dashed lines respectively).

Comparing the thermal photonic distribution at the different stages as a function of photon frequency (dashed lines in Fig. 1.4), and the expected photon occupation[98] in

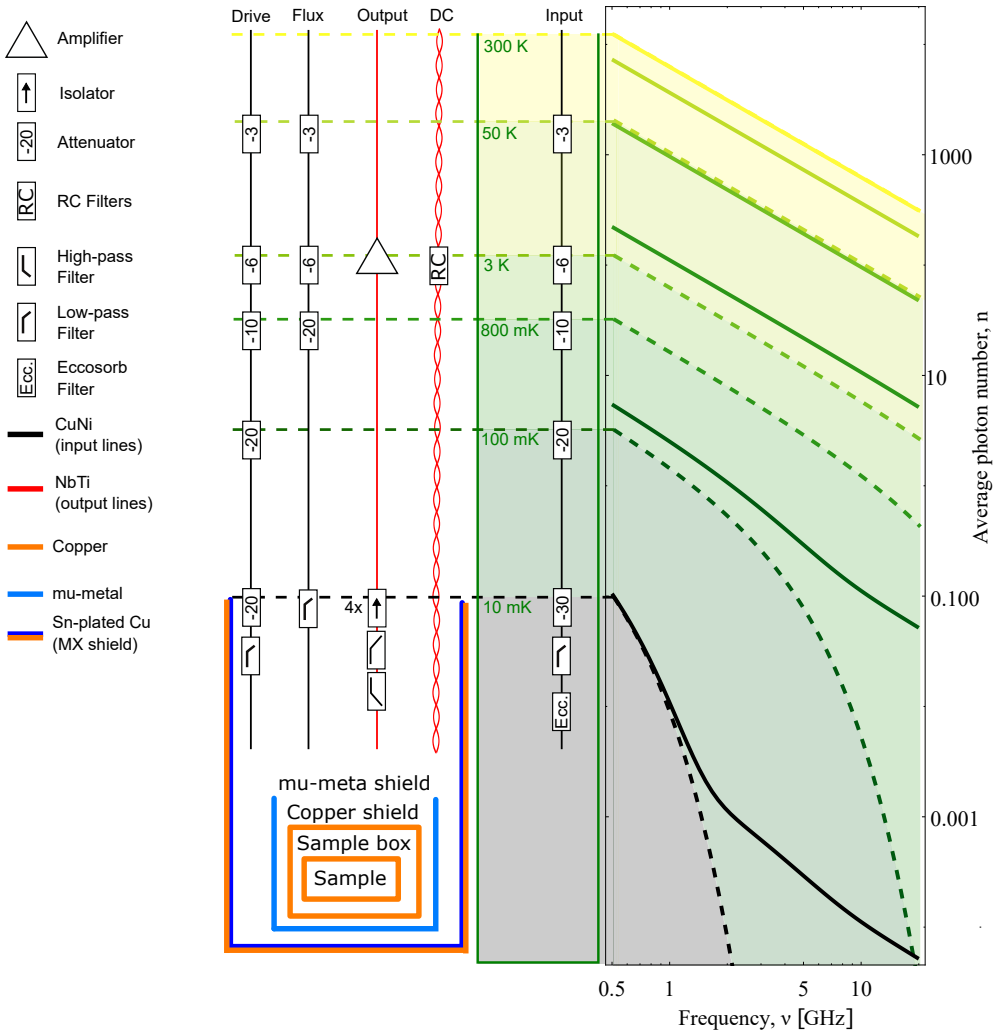

Figure A.4: *Coaxial lines in the cryogenic setup and their photon distribution. On the left, a list of the components and materials found in the cryostat. The four microwave lines and the direct current (DC) twisted pairs used in the experiments. On the right, the thermal photon distribution of the cryostat stage (dashed lines) can differ of many orders of magnitude compared to the one in the input line (solid line).*

the coaxials line (solid lines), we conclude that the photon distribution in the coaxial lines is nonthermal. The choice of the attenuation profile is due to a balance between not generating too much heat, exceeding the cooling power of the cryostat at 10 mK (few μW) and maintaining the transmission line photonic population small enough. In papers **Paper D** and **Paper E** we injected calibrated white noise to artificially warm up the photonic temperature in these lines, while not altering the state of other thermal baths in the cryostat. In the same experiments we used Eccosorb (CR 117) home made filters, to prevent high frequency (above 50 GHz) stray radiation from higher stages to reach the sample.

For the output lines a different approach is necessary. The signal, in some cases, can be in average smaller than a single photon. So we use superconductive materials (CuNi) for realizing the lines, and we isolated the sample from the HEMT amplifiers noise, with isolators.

A.3 Mixing chamber plate thermal distribution

In **Paper D** we measure the photonic occupation number in the waveguide directly coupled to the qubit in steady state and as function of time. As we see in Fig. A.4 the sample is embedded in a number of different shields, that inevitably increases its distance from the rubidium oxide thermometer. In this section we show that the temperature gradient across the last stage of the cryostat is negligible even in milliKelvin environments.

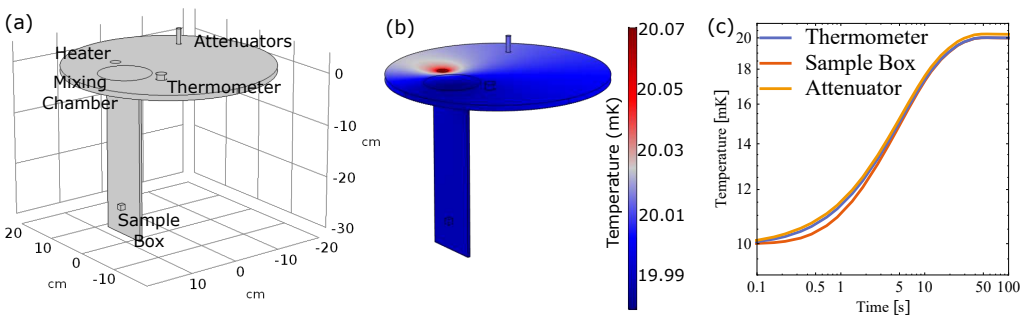

Figure A.5: *Thermalization at the mixing chamber stage. (a) Geometry of the mixing chamber state: the cooling power is applied on the footprint of the mixing chamber. Diametrically opposed to it, there are the heater and the thermometer. We place the sample at the end of a vertical copper tail. (b) Steady state solution of the heat equation. (c) Averaged (by volume) temperatures for the thermometer, the sample box and the attenuator, when a heating load perturbs the initial condition at 10 mK.*

Fig. A.5(a) shows a 3D model of the mixing chamber stage, with the main cryogenic elements. These parts are realized in gold-plated oxygen-free copper. We simulate the heat transport, by considering the electronic degrees of freedom [99]. In particular, the heat capacity is given by $C = \gamma T$, with $\gamma = 0.011 \frac{J}{KgK^2}$, while the heat conductivity of

electrons is calculated from the Wiedemann–Franz law $\kappa = \sigma LT$, with $L = 1 \cdot 10^{-8} \frac{W\Omega}{K^2}$ and the electric conductivity σ obtained for RRR coefficients equal to 1000.

We manually add the cooling power, that scales quadratically with temperature, while the heating power is fixed during the simulation. In Fig. A.5(b) we report the stationary solution of the heat equation for the mixing chamber stage. As already mentioned, there is no appreciable thermal gradient at 20 mK.

When we solve the heat equation in the time domain [see Fig. A.5(c)] for the entire geometry, we can calculate the average temperature in the vicinity of the thermometer, for the attenuators and for the sample. Also in this case, their temperature evolution is very similar. Moreover this simulation agrees with the time scale measured in the fridge in **Paper D**.

A.4 Sample box

A superconducting device is composed by many different parts. The sample box encloses the sample and delivers the electromagnetic signal to it. It assures a structural support and a good thermal contact.

A.4.1 Electromagnetic modes simulations

We build the sample holder to prevent the decay of the circuit excitation in the box. The box behaves as a 3D cavity, and we design it such that the first mode has a frequency very detuned from the measurement frequency.

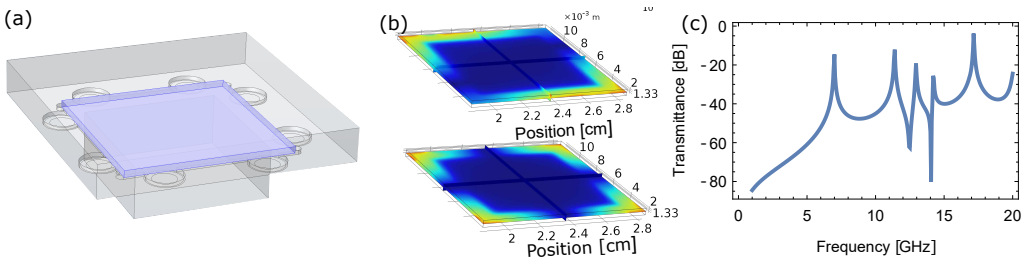

Figure A.6: *Electromagnetic environment in the sample box. (a) Vacuum region inside the 8-port (spyder) sample box (grey) and 1x1 cm sample (blue). (b) Electric field distribution for the first two chip-modes at 7 and 11 GHz respectively.(c) Transmittance between two ports of the sample box.*

Fig. A.6(a) shows the internal area of a sample box with a chip inside. When a microwave tone is injected in this space, the box resonates at its normal frequency. Moreover the dielectric of the chip reduces the frequency of these modes. We dilute the electric field in the chip, milling a pocket beneath the sample. In Fig. A.6(b) we display the electric field distribution for the first two chip modes, that correspond to transmission maximum between two ports of the box [see Fig. A.6(c)]. The measurement of transmission can be performed at room temperature to confirm the prediction of the

simulation.

A.4.2 Bonding of the sample

The last step before cooling down a device and measuring its performance, is the wire-bonding of the aluminum ground plane to the copper body of the sample box, and the inner conductor to the launcher on chip. Each single wire bond acts as an inductor, so a high density of wirebonds is beneficial in maintaining a good ground plane [100] .

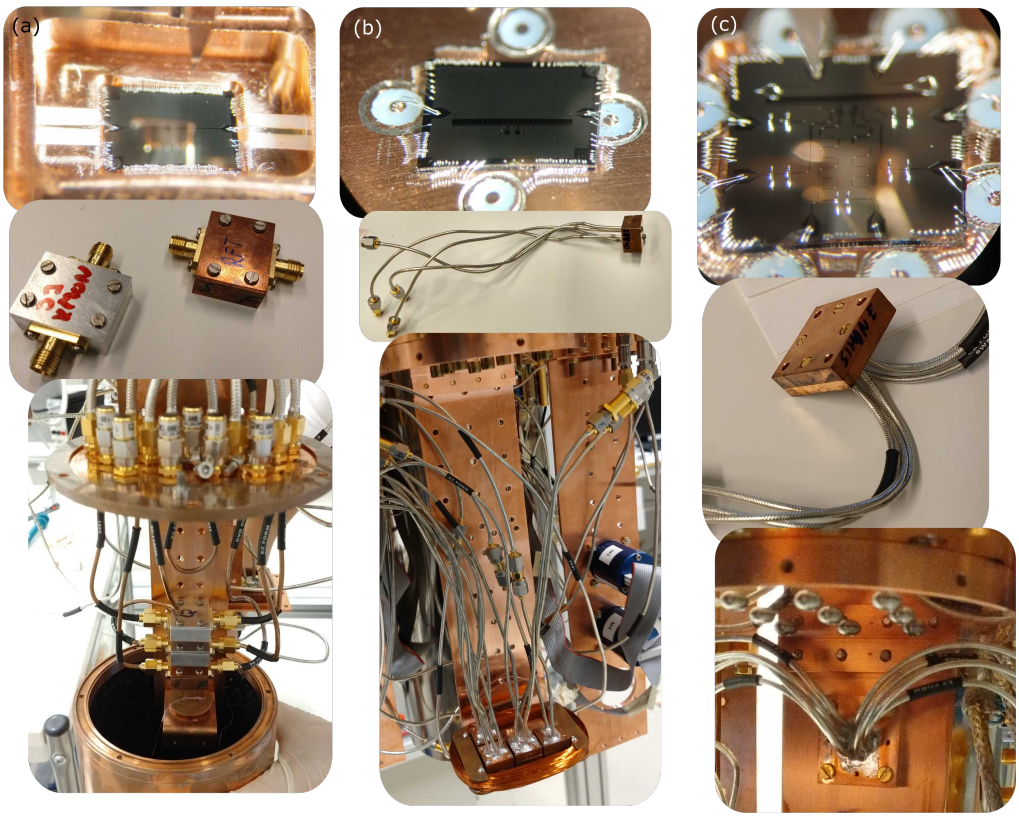

Figure A.7: *Sample boxes, bonding and cryogenic installation. (a) Two-port sample boxes, realized in copper or aluminum. They use SMA connectors where we directly apply the bonds. (b) 4-port sample box. We use coaxial cables perpendicular to the sample. This box is integrated in a superconducting coil. (c) 8-port sample box. Using the same geometry of the 4-port one, we can connect the sample directly to the coaxial cable.*

Fig. A.7 shows the three kind of sample boxes used in the experiment in this thesis. In **Paper A**, **Paper D** and **Paper E** we use the 2-port sample holders, **Paper B** and **Paper C** used the holder shown in Fig. A.7(b) and the experiment in **Paper F** use the spider sample holder, shown in Fig. A.7(b). Depending on the bonding conditions, and the sample

dimensions, we apply two or three bonds to connect the launching pads on the chip, while 50-100 bonds are used for the ground plane. Moreover, in some occasions, we reconnect the ground with bonds on the chip (this practice has been successively avoided with the introduction of air bridges).

–Say it with me: "I don't know."
Dr Edward Brazelton, The Core (2003)

B Measurements

We excite the energy levels of a qubit or we tune its transition frequencies by sending microwave pulses to the qubit coupling ports. An accurate state preparation requires a careful calibration of these pulses. Once the calibration its concluded, we characterize the qubit, measuring its decay and dephasing rate or its excited state population.

B.1 State preparation

The transmon Hamiltonian Eq. (1.33) in presence of a coherent drive with frequency ω_d is

$$\hat{H}/\hbar = \omega_q \hat{b}^\dagger \hat{b} - \frac{E_C}{2}\hat{b}^\dagger \hat{b}^\dagger \hat{b}\hat{b} + \frac{\Omega(t)}{2}(\hat{b}^\dagger + \hat{b}), \tag{B.1}$$

where $\Omega(t) = \Omega e^{i\omega_d t}$ is called Rabi rate and depends on the coupling of the atom with the driving line as well as the driving amplitude. When restricted to the subspace spanned by the state vectors $\{|g\rangle, |e\rangle\}$, the Hamiltonian can be written with Pauli operators [49] as

$$\hat{H}/\hbar = \frac{\omega_q}{2}\hat{\sigma_z} + \Omega(\hat{\sigma}^+ + \hat{\sigma}^-) \tag{B.2}$$

Writing the amplitude of the driving field proportional to the voltage source [101] as

$$\Omega = CV = I(t)\cos(\omega_d t) + Q(t)\sin(\omega_d t), \tag{B.3}$$

and applying the rotating wave approximation at the driving frequency ω_d, we can rewrite the Hamiltonian as

$$\hat{H}/\hbar = \frac{\delta}{2}\hat{\sigma_z} + \frac{C}{2}I(t)\hat{\sigma_x} + \frac{C}{2}Q(t)\hat{\sigma_y}, \tag{B.4}$$

where $\delta = \omega_q - \omega_d$.

Representing the two-dimensional subspace of the state of the qubit as the Bloch Sphere [102], the part $I(t)$ drives rotations along the x-axsis, while $Q(t)$ along the y-axis. We generate the signals $I(t)$ and $Q(t)$ with an arbitrary waveform generator and we up-convert with the carrier frequency ω_d (see Fig. A.3 for more details).

In **Paper E** and in **Paper F**, we excite the transmon to its third level. In the subspace spanned by$\{|e\rangle, |f\rangle\}$, the Hamiltonian Eq. (B.4) is valid, and when the qubit remains in this subspace we can calibrate the pulses in the same way we do in the subspace spanned by $\{|g\rangle, |e\rangle\}$.

B.1.1 Qubit frequency and read-out

In an open waveguide geometry the qubit can be directly excited by a coherent microwave tone or a pulse. At low input power ($n \ll 1$), the scattering properties of the qubit are the same as that of a linear oscillator, because the probability to excite the $|f\rangle$ state is negligible. In **Paper D** we directly probe the qubit frequency measuring the scattering.

In **Paper A**, **Paper E** and **Paper F** the qubit is coupled to a readout resonator, that we use to measure the population of the qubit. In the dispersive regime, the system Hamiltonian Eq. (1.69) shows that the frequency of the resonator depends on the state of the qubit [see Fig. B.1(b)].

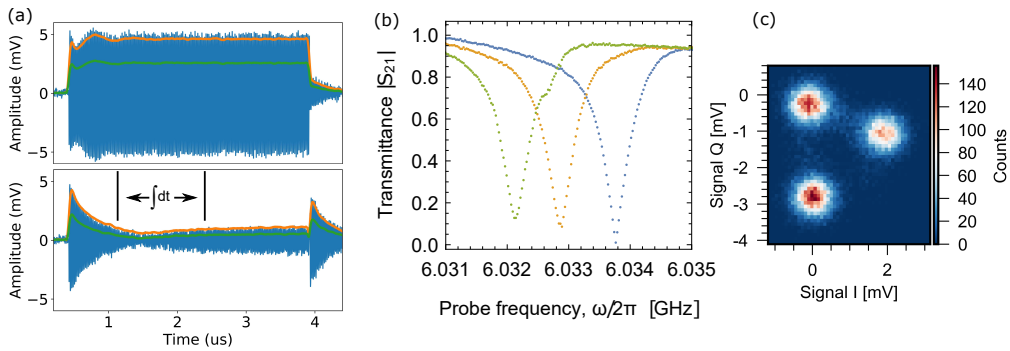

Figure B.1: *Qubit read-out of a qubit as in paper A and paper E. (a) Demodulated signal (blue) for the resonator for a driving probe detuned and on resonance (top and bottom panels, respectively). The signal is demodulated to DC with only the I quadrature, ot using both I and Q quadratures (green and orange solid line respectively) (b) Dispersive shift of the resonator for the qubit in the ground, first and second excited state (blue, orange and green respectively). (c) Quadrature histograms of the resonator for the qubit in the ground, first and second excited state.*

As we saw in chapter 2, the state prepared in a qubit has a finite lifetime, that constrains the time necessary[1] for read-out $t \approx 1/\kappa_r$. By design, we choose κ_r as a trade off between a fast read-out and the Purcell decay rate sowed in Eq. (2.7) [103].

[1] This is true for a pulse of constant amplitude. A pulse with an initial section of larger amplitude can load the desired amount of photons in the resonators faster than this limit.

In this thesis, we used a square pulse to read out the qubit, generated with the setup shown in Fig. A.3(b). The two quadratures I_r and Q_r are integrated after after the steady state is reached, as indicated in the lower panel of in Fig. B.1(a). Varying the carrier frequency ω_d, we measure the resonator dispersive shift for the different states of the qubit [see Fig. B.1(b)] and we can find the frequency that gives the best contrast. By building the histogram of integrated signal (without averaging) we can measure our accuracy in assessing the qubit state (read-out fidelity). In Fig. B.1(c) we display the histogram for a ternary read-out.

One of the advantages of the dispersive read-out is the possibility to determine the state of the qubit using many photons. This improves the signal to noise ratio by many orders of magnitude, compared to measurements with single photons. However, the approximations introduced to obtain the Hamiltonian Eq. (1.69) are valid only below a critical photon number [104]:

$$n_c = \frac{\Delta^2}{4g^2}. \tag{B.5}$$

Once we are able to read out the frequency of the resonator, we can drive the qubit in a mixed state with a long (with respect to its lifetime) pulse, and as soon as we stop the driving, measure the resonators state. Once, the rough frequency of the qubit is known, it can be accurately measured by extracting the period of a Ramsey sequence.

In these pulse schemes, implemented in the experiments, the read-out pulse is unaltered with respect to the trigger during the sequence, while the timing of the driving pulses is adjusted according to the scheme. In this way the demodulation window and consequently phase of the down-converted IF of the read-out pulse is maintained during the full experiment.

B.1.2 Pulse amplitude calibrations

In order to prepare the state of the qubit accurately, we need to calibrate the quadrature $I(t)$ and $Q(t)$ of the driving pulse in Eq. (B.3). Initially we can run a Rabi sequence, exciting the qubit with a resonant pulse of increasing amplitude. The pulse that completely swap the population P_e and P_g is usually named π-pulse. In order to measure a more accurate value for the amplitude of this pulse we can repeat this sequance adding an odd number of pulses, as shown in Fig. B.2(a). Using this error amplification [105], we can measure a precise value for the amplitude of the π-pulse [see black arrow in Fig. B.2(b)].

B.1.3 Derivative Removal by Adiabatic Gate (DRAG)

Driving the transition $|g\rangle \leftrightarrow |e\rangle$ on the qubits used in our experiments, there is a nonzero probability to excite the state $|f\rangle$ due to a finite anharmonicity $E_C \approx 200\,\text{MHz}$. By implementing the "derivative removal by adiabatic gate"[106] (DRAG), we modify the $Q(t)$ quadrature such that

$$Q(t) = \frac{\tau_d}{E_C}\partial_t I(t), \tag{B.6}$$

where τ_d is the DRAG scaling coefficient. In order to experimentally determine τ_d, we use the pulse scheme showed in Fig. B.2(e), where an even number of positive and negative

π-pulses drive the qubit. After 80 pulses the qubit is excited when the DRAG is not implemented ($\tau_d = 0$), as shown in Fig. B.2(f).

Once we calibrate the π-pulse for transition $|g\rangle \leftrightarrow |e\rangle$, we can bring the qubit in the excited state and calibrate the π-pulse for the higher excitation subspace as shown in Fig. B.2(c), (d), (g) and (h).

B.2 Common pulse schemes

As we saw in chapter 2, when the qubit is coupled to an unwanted bath, the resulting noise drives the qubit, causing decoherence increasing the qubit population. In this section we describe the pulse scheme we used for measuring these effects.

B.2.1 Decay rate, T_1

In order to measure the decay rate (longitudinal relaxation, or T_1) we apply the pulse scheme showed in Fig. B.3(a). An initial pulse excite the qubit and a read-out pulse assesses the qubit state after incrementally larger waiting time τ. The results of this measurement is shown in Fig. B.3(b). As expected [see Eq. (2.1)], the population of the qubit exponentially decays as a function of read-out delay τ.

B.2.2 Dephasing, T_2

Representing the state of the qubit on a Bloch sphere, during the longitudinal decay the state is always on the z-axis, therefore it is affected only by transverse noise [107]. In order to have the best sensitivity to longitudinal noise, and measure the dephasing that produces, we prepare the state of the qubit along the equator of the Bloch sphere with a $\pi/2$-pulse. After a waiting time τ, a second $\pi/2$-pulse is applied, and the qubit population is read out.

The pulse sequence for measuring

During the free evolution, the qubit is also affected by longitudinal noise. The characteristic time of the decay is in fact a combination of the pure dephasing T_ϕ and the relaxation time T_1:

$$\frac{1}{T_2^*} = \frac{2}{T_1} + \frac{1}{T_\phi}. \tag{B.7}$$

Fig. B.4(b) and (d) show the population in $|e\rangle$ and $|f\rangle$ for a Ramsey pulse sequence. As we mentioned, after the first spectroscopy of the qubit, we use this measurement for measuring accurately the qubit frequency and its anharmonicity.

B.2.3 Population

Following the method in [108] we can measure the population in the first excited state of the qubit. Fig. B.5(a) shows the pulse scheme used in the experiments: the qubit is prepared in $|e\rangle$ and after a coherent driving of Rabi oscillations between $|e\rangle$ and $|f\rangle$, the population of $|e\rangle$ and $|g\rangle$ is swapped. The Rabi oscillations between the states $|g\rangle$ and $|e\rangle$

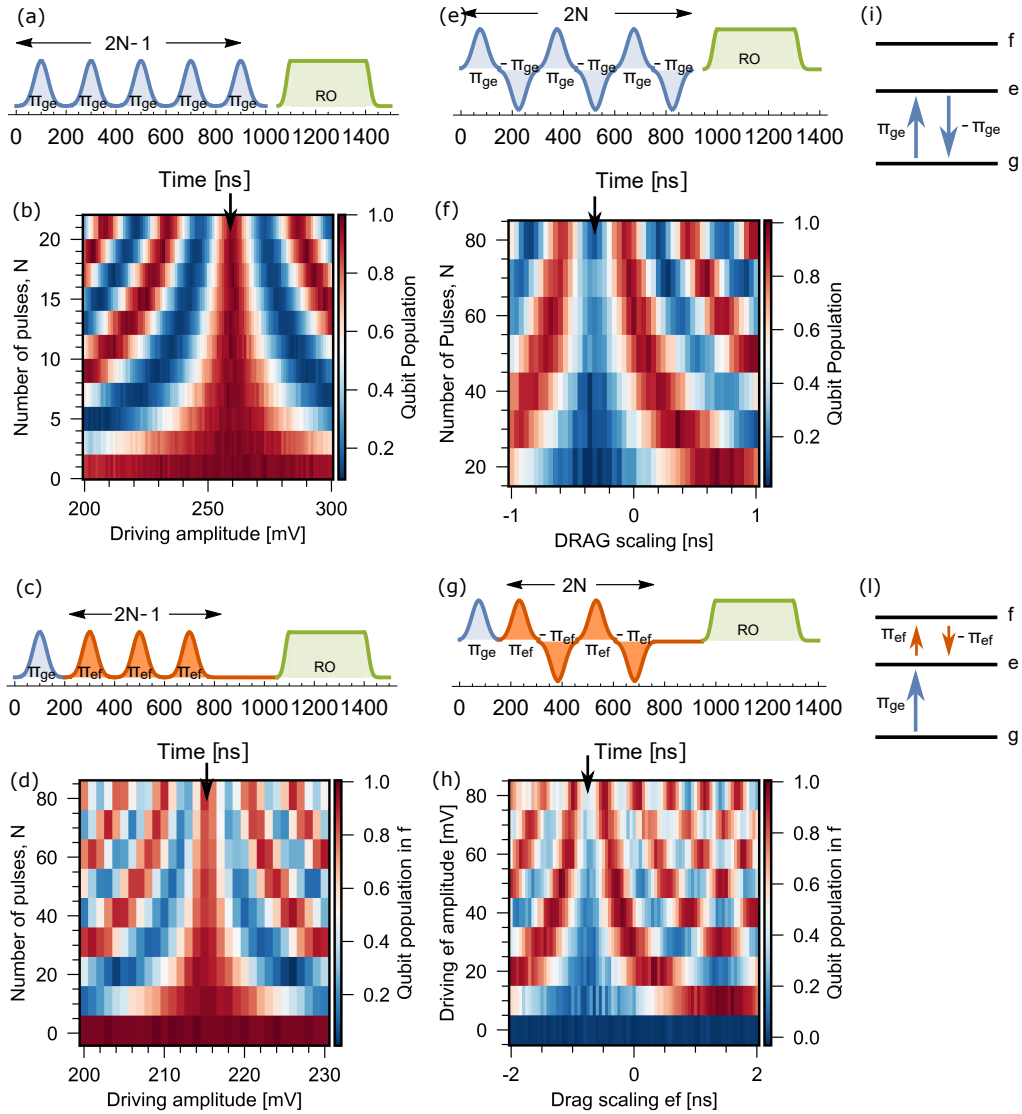

Figure B.2: *Driving pulse tune-up. (a) An odd repetition of π_{ge}-pulses amplifies the driving error. (b) Readout of the population in $|e\rangle$ as a function of the driving amplitude and number of pulses. (c) π_{ef}-pulse amplitude calibration sequence. (d) Population of the state $|f\rangle$ as a function of number of pulses and their amplitude (the black arrrow indicate the optimal value). (e) DRAG calibration sequence. (f) Population in $|e\rangle$ as a function of pulses and their DRAG coefficient. (g) Calibration of DRAG for the transition $|e\rangle \leftrightarrow |f\rangle$. (h) Population in $|f\rangle$ as a function of the number of pulses and their DRAG coefficient. (i) and (j) Energy structure and driven transitions.*

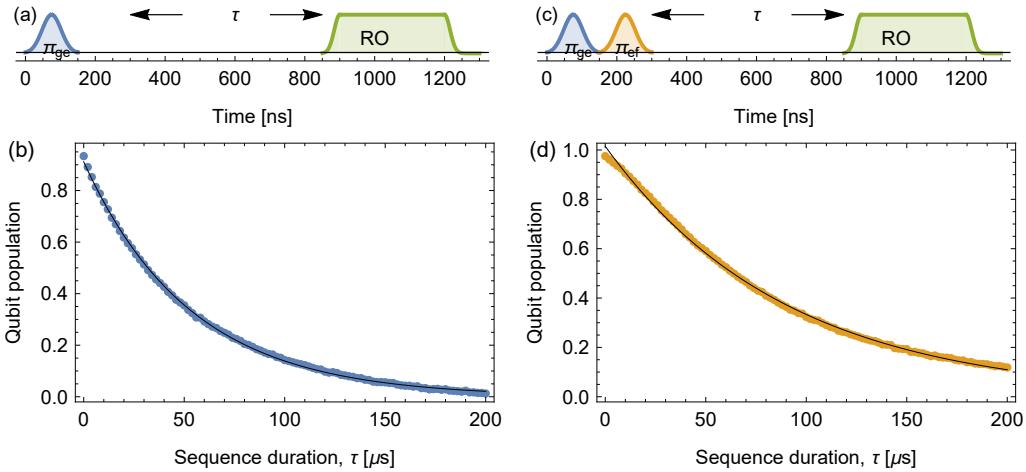

Figure B.3: *Measurement of decay rate. (a) The pulse scheme consists in exciting the qubit and reading-out its population after increasingly larger waiting time. (b) The population P_e of the qubit as a function of time. (c) A π_{ge}-pulse excite the qubit, and a following π_{ef}-pulse prepare the qubit in $|f\rangle$. The read-out pulse measure the population of the qubit. (d) Population decay from $|f\rangle$ as a function of time.*

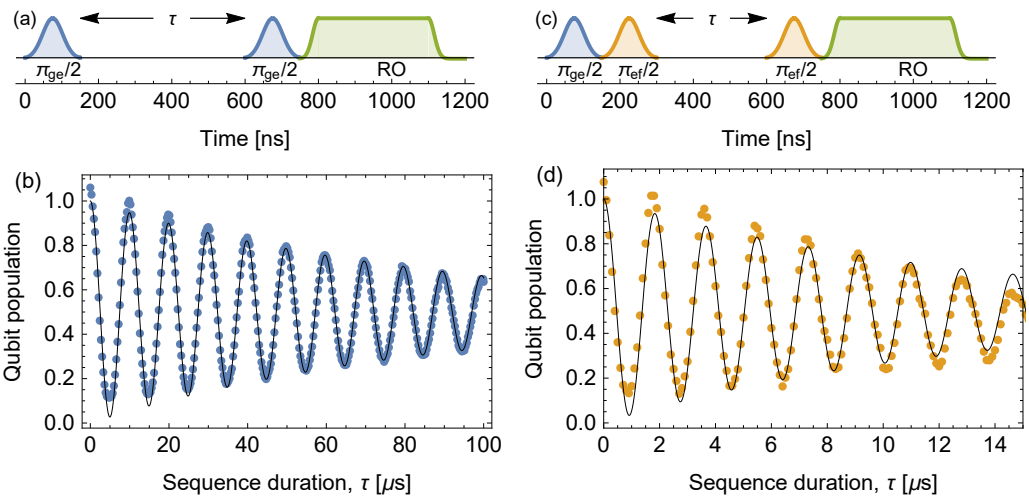

Figure B.4: *Ramsey sequence. (a) Pulse scheme. The first π/2-pulse prepares the qubit in $(|g\rangle + |e\rangle)/\sqrt{2}$, after a time τ of free evolution a second π/2-pulse is applied and the population measured. (b) Population in $|e\rangle$ as function of the sequence duration. (c) After the initial π_{ge}-pulse, we can apply the same sequence showed in (b). (d) Population of the qubit in $|f\rangle$.*

have an amplitude A_{ref} [see Fig. B.5(b)]. The sequence is repeated without preparing the qubit in the excited state. The Rabi oscillations reported in Fig. B.5(d) are due the residual population, and present a much smaller amplitude A_0.

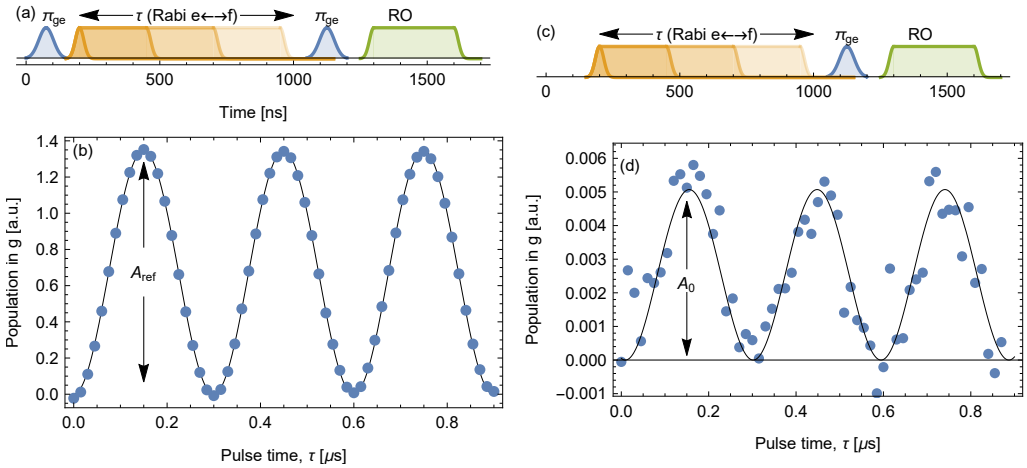

Figure B.5: *Measurement of the population of the first excited state. (a) Pulse scheme. After preparing the qubit in $|e\rangle$, we drive the oscillation between $|e\rangle$ and $|f\rangle$. After a another π_{ge} we readout the population in $|g\rangle$. (b) Population in $|g\rangle$ as function of the driving duration. (c) Same pulse scheme in (a) without the initial state preparation. (d) The population in $|g\rangle$ oscillates due to the residual population in $|e\rangle$.*

After obtaining the amplitudes A_{ref} and A_0 from the fits we can calculate the population in $|e\rangle$ as

$$P_e = \frac{A_0}{A_{\text{ref}} + A_0} \tag{B.8}$$

B.3 Attenuation calibration

The knowledge of the the total attenuation of a coaxial line in the cryogenic setup is necessary to extract the Rabi rate Ω used in the experiments. A linear cavity is not enough to extrapolate this information because its response is the same at different powers, while any nonlinear element can be used to measure the attenuation. In the experiments presented in this thesis we used two possible configurations to calibrate the field seen by the qubit. From this we can find the attenuation of the line.

B.3.1 Atom in open waveguide

In **Paper D** we see that for a particular driving strength, Ω_{m}, the reflection vanishes [see Fig. 2.4(b)]. If we neglect the photonic population, and in the case $\gamma_{\text{ph}} \ll E_{\text{C}}/\hbar$, Eq. (2.15) reads

$$1 = 4(\Omega/\gamma_{\text{ph}})^2. \tag{B.9}$$

Knowing the power emitted by the room temperature microwave source when this condition is verified, lets us calibrate the attenuation of the input line.

B.3.2 Atom in a cavity: Stark shift

Considering the Jaynes-Cumming Hamiltonian Eq. (1.67), the frequency of the atom is Stark shifted proportionally to the number of photons in the cavity, n. In order to calculate this quantity, we use Heisenberg equation with driving, Eq. (1.71). With these assumptions we obtain Eq. (1.72), that solved for the intra-cavity field becomes

$$\hat{b} = \frac{\sqrt{\kappa_{\mathrm{nr}}}}{1/2(\kappa_{\mathrm{r}} + \kappa_{\mathrm{nr}}) - i(\omega - \omega_0)} \hat{a}_{\mathrm{in}}. \tag{B.10}$$

Calculating the conjugate operator $\hat{b}^\dagger$, we can derive the average photons in the cavity

$$\hat{n} = \hat{b}^\dagger \hat{b} = \frac{\kappa_{\mathrm{r}}}{1/4\kappa_{\mathrm{tot}}^2 + \Delta^2} \hat{a}_{\mathrm{in}}^\dagger \hat{a}_{\mathrm{in}} = \frac{P_{\mathrm{in}}}{\hbar\omega} \frac{\kappa_{\mathrm{r}}}{1/4\kappa_{\mathrm{tot}}^2 + \Delta^2} \tag{B.11}$$

where the input power at the sample is

$$\frac{P_{\mathrm{in}}}{\hbar\omega} = \hat{a}_{\mathrm{in}}^\dagger \hat{a}_{\mathrm{in}}. \tag{B.12}$$

In the usual case of an overcoupled resonator where the radiative decay is much larger than the intrinsic one, $\kappa_{\mathrm{r}} \gg \kappa_{\mathrm{nr}}$, we can approximate the total number of photons in the linear cavity for a resonant driving to be

$$\hat{n} = \frac{P_{\mathrm{in}}}{\hbar\omega\kappa_{\mathrm{r}}}. \tag{B.13}$$

If we want to know the attenuation A at the sample, we measure the atom frequency ω_{q1} and ω_{q2}, while driving the cavity with two different calibrated powers (at room temperature), P_1 and P_2, respectively. According to Eq. (1.67), the Stark shift $\delta = \omega_{q2} - \omega_{q1}$ is

$$\delta = \chi \Delta n = \frac{(P_1 - P_2)}{A\hbar\omega\kappa_{\mathrm{r}}} \tag{B.14}$$

B.4 Mutual inductance matrix in two qubit experiments

It is difficult to shield magnetic field on chip. Therefore the magnetic flux generated by one flux line will couple to all the inductances on a device, including a squid loop that is far from it. Measuring the mutual inductance matrix is possible to compensate this effect with the proper flux line. In **Paper F** we applied this procedure.

–To infinity and beyond!

Buzz Lightyear, Toy Story (1995)

C

Design and fabrication

The experiments presented in this thesis are performed with devices fabricated on silicon or gallium arsenide, on chips with dimensions $5 \times 7\,\mathrm{mm}^2$ or $6.6 \times 6.6\,\mathrm{mm}^2$. The chips are wire bonded in an oxygen-free copper-free or aluminum sample box (see Fig. A.7). The devices have been designed and fabricated using the MyFab Chalmers cleanroom. This process usually consisted of five parts:

- design a prototype of a portion of the sample in Autocad;
- import the geometry in an electromagnetic solver to simulate Maxwell's equations and check the target parameters;
- design the full chip in Autocad, one layer for each lithography step;
- fabricate the design on a 2 inches wafer;
- dice or cleave the wafer into chips.

C.1 Design editing and simulation

Some of the devices realized in this thesis were designed "piece-wise", mainly concentrating on different parts of their geometry: capacitive (or inductive) coupling points, resonators or qubits, Josephson Junctions or SQUID.

C.1.1 Coupling and microwave ports

The radiative coupling rates are set by designing the capacitance (or inductance) that couples different elements (see Eq. (1.66) and (1.78)). We calculate these values with a

finite element solver in Microwave office (AWR). Fig. C.1(a) shows the usual geometry

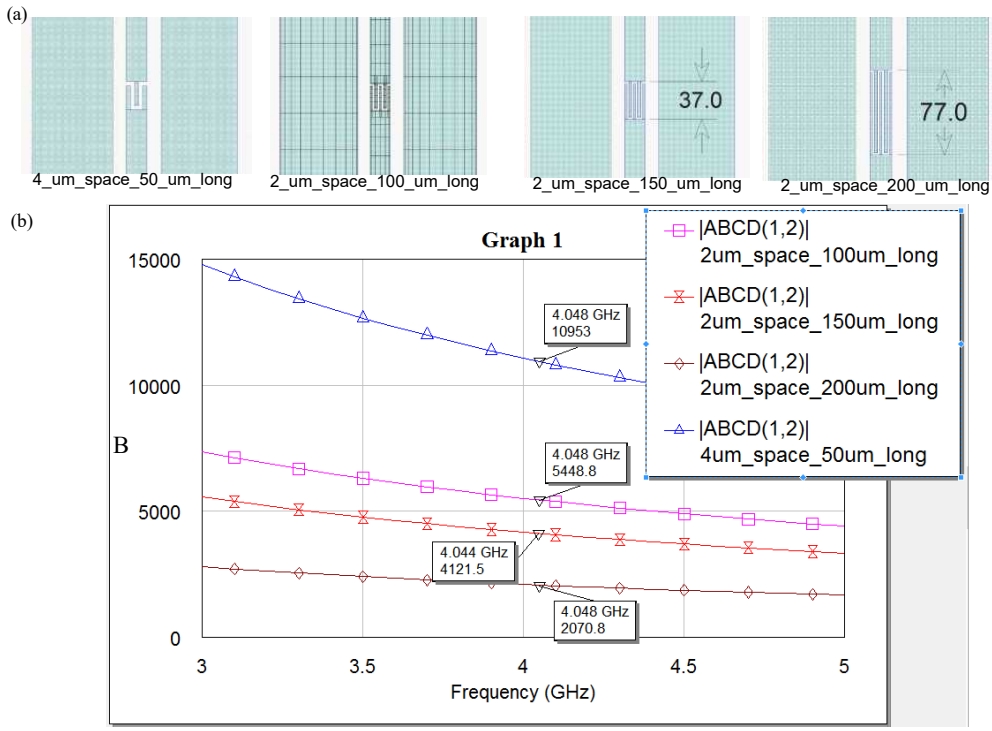

Figure C.1: *Numerical solution of the ABCD matrix for four different coupling geometries. (a) Capacitive coupling for a transmission line with progressively longer overlapping fingers (from left to right). (b) Absolute value of B element of the ABCD matrix as a function of frequency.*

of CPW coupling points. In the simulation we set the parameters of the substrate, the metal conductivity and finally the boundary conditions that implement a driving port. From the solution of the electromagnetic equations, we can calculate the value of the coupling capacitance C as

$$C = \frac{1}{2\pi f |B|}, \tag{C.1}$$

where B is the element of the ABCD transition matrix [35]. Remarkably, solving only the electrostatic equation (Poisson's equation), may not produce accurate results for the target frequency. In Fig. C.1(a) and (b) we show 4 different capacitor geometries and the correspondent value of B as function of frequency, simulated in AWR.

C.1.2 Qubits and resonators

For elements not directly connected to a transmission setup we used electrostatic simulation. Fig. C.2 shows the geometry simulated for **Paper F** with a finite element model

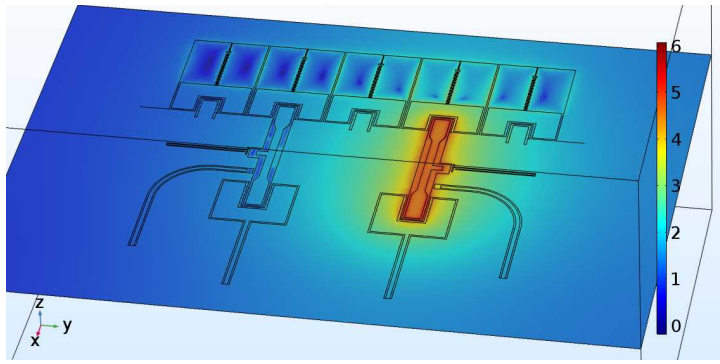

Figure C.2: *Numerical solution of the Poisson's equation with a terminal set to 1 V with respect to the ground plane, and the other terminals are left floating. The color scale represents the strength of the electric field.*

(FEM) solver. The device geometry is imported as a two dimensional layer of perfect conductor. By solving the Poisson's equation, we obtain the electric field and charge distribution. We use this result to calculate the capacitance matrix used in the Lagrangian of the circuit. The capacity matrices in **Paper F** and in section 1.4.2 are calculated with this method.

C.1.3 Flux line field simulation

The magnetic flux in a SQUID loop can be generated by a macroscopic superconducting coil (see Fig. A.7) or by an on chip flux line. For applications that require static tuning of a single qubit, the superconducting coil represents the best solution: its large inductance and mass makes it resilient to small current or thermal fluctuations. Moreover, the flux it produces is rather uniform over the full chip area. On the other hand, fast frequency tuning (as the one used in **Paper F**) requires an on-chip flux line.

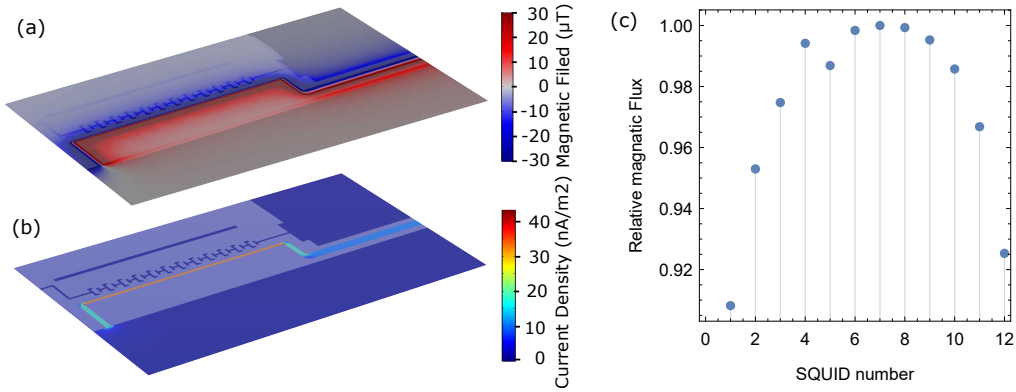

Figure C.3: *Design of on-chip flux lines. (a) Magnetic field perpendicular to the chip surface (b) Current density along the flux line. (c) Flux distribution in the SQUID array adjacent to the flux line.*

The design of the flux line is constrained by the possibility to produce at least half a flux quantum in the SQUID without exceeding the critical current density of the line. Fig. C.3 shows the results of a FEM simulation of the magnetic filed and current density produced by a current in a flux line. In Fig. C.3(a) the colorscale displays the magnetic flux component perpendicular to the chip surface. Numerically integrating this component in the SQUID area we can calculate the maximum flux we can inject.

Moreover, the numerical evaluation of the magnetic filed distribution can help improve the uniformity of the magnetic filed in complex geometries, such as for example a SQUID array [see Fig. C.3(c)].

C.2 Room temperature characterization

The normal state of the aluminum limits the possibility to test some parts of the devices, due to the large resistive losses. Nevertheless the JJs and SAW resonators can still provide useful information when probed at room temperature.

C.2.1 Test junction measurement

Performing a cool-down of a devide with not optimal parameters or, in the worst case, nonfunctional, delays the experiments. Importantly, the Josephson energy can be inferred by measurement at room temperature. Using the Ambegaokar-Baratoff relation [109, 110] we link the normal resistance R_N of a JJ to its critical current I_J:

$$R_N = \frac{\pi\Delta}{2eI_J} \tag{C.2}$$

Using Eq. (1.25), we can estimate the Josephson energy directly from the measurement of the normal resistance.

Fig. C.4(a) shows the parameter analyzer used for the 4-probes resistance measurement. We set a current sweep (often from -1 μA to 1 μA), and we use the machine software (Kyte) to automatically extract the resistance value from a linear fit of the measured IV-trace. We usually do not measure directly the JJ on the device, but we fabricate few test Junctions on the same chip [see Fig. C.4(b)].

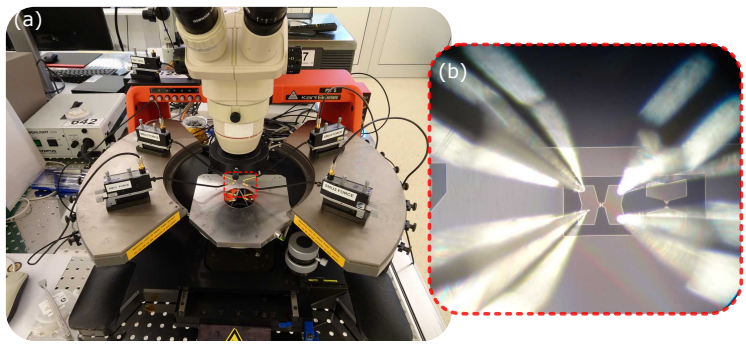

Figure C.4: *Measurement of JJ normal resistance. (a) Parameter analyzer used in the 4-probes measurements of the JJ test structures in (b).*

C.3 Samples fabrication recipes

In this sections we report the recipes used for the fabrication of the samples discussed in this thesis.

C.3.1 Qubits on silicon

Qubit and JJ resonators on silicon used for samples described in **Paper A**, **Paper D**, **Paper E** and **Paper F**. The recipe comprises three lithography steps, and with all tools available it can be completed in one week.

Removing Oxide Layer:

- Standard Cleaning 1 [111] for 10 min.
- Quick Dump Rinse (QDR).
- Dip the wafer in 2% HF solution for 1 min.
- QDR and blow dry with the nitrogen gun.

Metal deposition:

- Load in the load-lock of the evaporator (Plassys) as fast as possible and pump it.
- Heat the substrate to 300^o C for 10 min.
- Pump the load-lock for 12 hours (expected pressure $6 \cdot 10^{-8}$ mbar).
- Deposit aluminum to a thickness of 150 nm at a rate of 1 nm/s while rotating around the wafer axis.
- Static oxidation with pressure 10 mbar for 10 min

Aluminum Etching:

- Spin AZ1512HS at 4000 rpm for 50 s.
- Bake on hot-plate at 100^o C for 60s.
- Expose in Laser writer, Focus: 40, Intensity: 80, Transmission: 100.
- Develop AZ Developer:H2O 1:1 for 30s.
- Rinse in water for 2 mins.
- Blow dry with nitrogen gun.
- Ash in oxygen plasma with power 40 W for 30 s.
- Etch in Transene type at 100^o C for 1 min.
- Rinse in water.

Removing resists:

- Rinse in remover 1165 for 5 min at 85^o C.
- Ultrasound in remover 1165 at 35 kHz in sweep mode and 40% power for 5 min.
- Ultrasound in methanol at 35 kHz in sweep mode and 40% power for 5 min.
- Ultrasound isopropanol (IPA) at 35 kHz in sweep mode and 40% power for 5 min.
- Blow dry with nitrogen gun.

Josephson Junctions:

- Spin-coat the wafer with 400 nm of copolymer MMA/PMMA and bake it at 160^o C for 5 min.
- Spin-coat a second PMMA layer of 400 nm and bake it at 160^o C for 5 min.
- Expose the designed pattern with a 100 kV electron beam, with a base dose of 800 $\frac{\mu C}{\text{cm}^2}$, with 2 nA current (and proximity error correction for electron back-scattering).
- Develop with a 1 : 3 solution of MIBK:IPA for 90 s
- Blow dry with a nitrogen gun.
- Ash away 10 nm of resist and possible organic residue with an oxygen plasma generated at 25 W for 20 s.
- Load the wafer in the Plassys evaporator, and pump for 12 h.
- At the base pressure of $5 \cdot 10^{-8}$ mbar, deposit 50 nm of aluminum at 45^o with 1 nm/s rate (corresponding to 35 nm of metal thickness on the wafer).
- Oxidize the aluminum at 2 mbar of 99.99% pure oxygen for 20 min.
- Rotate the wafer 90^o around its axis.
- Deposit 110 nm of aluminum at 45^o with 1 nm/s rate (corresponding to 80 nm of metal thickness on the wafer).
- Oxidize the aluminum at 10 mbar of Oxygen for 10 min.
- Submerge the wafer in Remover1165 at 85^o C for 20 min, then leave it to lift-off for more than 12 hours.
- Pipette away the metal residue from lift-off.
- Insert the beaker containing the wafer in an ultrasonic bath at room temperature. Use low power ultrasound at 35 kHz in sweep mode for 5 min.
- Repeat the previous step with a beaker with methanol and again with IPA.
- Blow dry the wafer with a nitrogen gun.

Patches:

- Spin-coat the wafer with 400 nm of copolymer MMA/PMMA and bake it at 160^o C for 5 min.
- Spin-coat a second PMMA layer of 400 nm and bake it at 160^o C for 5 min.

- Expose the designed with a 100 kV electron beam, with a base dose of 700 $\frac{\mu C}{cm^2}$, with 35 nA current (and no proximity error correction).
- Develop with a 1 : 1 solution of MIBK:IPA for 90 s
- Dip in isopropanol for 10 s and blow it dry with a nitrogen gun.
- Ash away 10 nm of resist and possible organic residue with an oxygen plasma generated at 25 W for 20 s.
- Load the wafer in the Plassys evaporator, and pump for 12 h.
- At the base pressure of $5 \cdot 10^{-8}$ mbar, ion mill ca 15 nm of aluminum with 400 V and 20 mA for 3 min.
- Deposit 200 nm of aluminum with 1 nm/s rate while rotating around the wafer axis.
- Oxidize the aluminum at 10 mbar of 99.99% pure oxygen for 10 min.
- Submerge the wafer in Remover1165 at 85^o C for 20 min, then leave it to lift-off for more than 12 hours.
- Pipette away the metal residue from lift-off.
- Insert the beaker containing the wafer in an ultrasonic bath at room temperature. Use low power ultrasound at 35 kHz in sweep mode for 5 min.
- Repeat the previous step with a beaker with methanol and again with IPA.
- Blow dry the wafer with a nitrogen gun.

C.3.2 CPW resonator on GaAs

Etched aluminum resonators on GaAs realized for **Paper B**. This process only requires one lithography step and can be completed in few days.

Metal deposition:

- Open wafer package (GaAs epi-ready wafers, individually packaged in inert nitrogen atmosphere).
- Load in the Plassys evaporator as fast as possible and pump it.
- Heat the substrate to 300^o C for 10 min.
- Pump the load-lock for 12 hours (expected pressure $6 \cdot 10^{-8}$ mbar).
- Deposit aluminum to a thickness of150 nm qith a rate of 1 nm/s while rotating around the wafer axis.
- Static oxidation with pressure 10 mbar for 10 min

Aluminum Etching:

- Spin AZ1512HS at 4000 rpm for 60 s.
- Bake on hot-plate at 100^o C for 60s.
- Expose in HEIDELBERG DWL laser writer, Focus: 50, Intensity: 90, Transmission: 100.
- Develop in AZ Developer:H2O 1:1 for 30s.
- Rinse in water for 2 min.
- Blow dry with nitrogen gun.
- Spin AZ1512HS at 500 rpm for 120 s on the wafer back;
- Bake at 120^o C for 120s in oven;
- Ash in oxygen plasma with power 40 W for 30 s.
- Etch in Transene etchant type A at room temperature (until the large pads are

exposed).
- Stop etching by diping in water.
- Rinse with water;

Removing resists:

- Rinse in remover 1165 for 5 min at 85^o C.
- Ultrasound in remover 1165 at 35 kHz in sweep mode and 40% power for 5 min.
- Ultrasound in methanol at 35 kHz in sweep mode and 40% power for 5 min.
- Ultrasound isopropanol (IPA) at 35 kHz in sweep mode and 40% power for 5 min.
- Blow dry with nitrogen gun.

Cleaving:

- Spin AZ1512HS at 4000 rpm for 60 s.
- Bake on hot-plate at 100^o C for 60s.
- Cleave with diamond scriber in $5 \times 7\,\mathrm{mm}^2$ chips.

C.3.3 SAW device on GaAs

Surface acoustic waves devices on GaAs realized for **Paper C**. This recipe contains three or four lithography steps depending on the presence of the junction.
Interdigitate transducer (IDT):

- Spin-coat the wafer with 60 nm of copolymer MMA/PMMA and bake it at 180^o C for 5 min.
- Spin-coat a second PMMA layer of 100 nm and bake it at 180^o C for 5 min.
- Expose the designed biased −20 nm in the fingers width direction with a 100 kV electron beam, with a base dose of 250 $\frac{\mu C}{\mathrm{cm}^2}$ (and proximity error correction for electron back-scattering).
- Develop with a 1 : 1 solution of MIBK:IPA for 60 s, blow dry with a nitrogen gun
- Ash away 10 nm of resist and possible organic residue with an Oxygen plasma generated at 50 W for 10 s.
- When reaching the base pressure of $5 \cdot 10^{-8}$ mbar, evaporate 30 nm of aluminuim with planary rotation of the wafer.
- Oxidize the aluminum before breaking the vacuum with 10 mbar of 99.99% pure Oxygen for 20 min
- Submerge the wafer in Remover1165 at 85^o C for 20 min, then leave it to lift-off for more than 12 hours.
- Pipette away the metal residue from lift-off.
- Insert the beaker containing the wafer in an ultrasonic bath at room temperature. Use low power ultrasound at 35 kHz in sweep mode for 3 min.
- Repeat the previous step with a beaker with methanol and again with IPA.
- Blow dry the wafer with a nitrogen gun.

The IDT cannot be directly seen with an optical microscope, but they appear of lighter color compered with the bulk metal (see Fig. C.5).

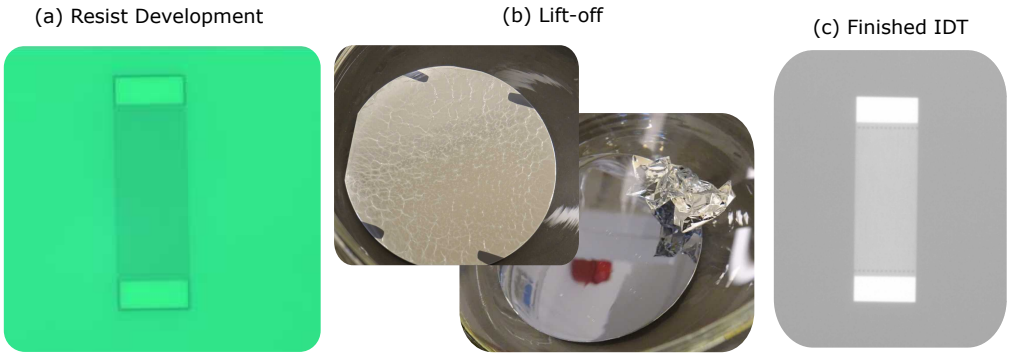

Figure C.5: *First lithography step. (a) Optical micrograph of the IDT on the 100 nm thick resist. The uniform shades implies a successful process even without resolving the individual fingers in an IDT. (b) After 3 h, a uniform sheet of metal detach from the wafer. (c) Micrograph of the IDT in aluminum (bright color) on GaAs (darker color) .*

Ground plane:

- Spin-coat the wafer with 400 nm of MCC LOR3A (6000 rpm for 5 min)
- Bake at 180^o C for 5 min.
- Spin-coat a second layer of S1805 resist of 1 μm and bake at 115^o C for 5 min.
- Expose in Laser writer, Focus: 50, Intensity: 90, Transmission: 100.
- Develop in MF319 for 60s.
- Rinse in water for 2 min.
- Blow dry with nitrogen gun.
- Ash 30 nm in oxygen plasma with power 50 W for 20 s.
- Load in the Plassys evaporator load-lock and pump for 12 h.
- When reaching the base pressure of $5 \cdot 10^{-8}$ mbar, evaporate 150 nm of aluminuim with planary rotation of the wafer.
- Oxidize the aluminum before breaking the vacuum with 10 mbar of 99.99% pure Oxygen for 10 min.
- Submerge the wafer in Remover1165 at 85^o C for 20 min then leave it to lift-off for more than 12 hours.
- Pipette away the metal residue from lift-off.
- Insert the beaker containing the wafer in an ultrasonic bath at room temperature. Use low power ultrasound at 35 kHz in sweep mode for 3 min.
- Repeat the previous step with a beaker with methanol and again with IPA.
- Blow dry the wafer with a nitrogen gun.

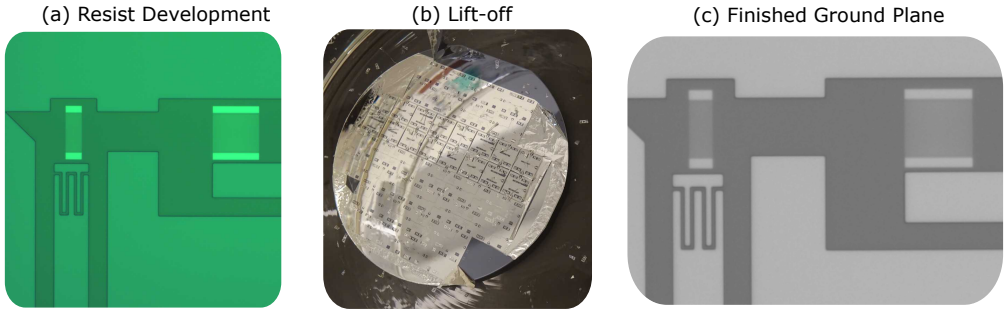

Figure C.6: *Second lithography step. (a) Optical micrograph of the ground plane exposed on the 1.5 µm thick resist. (b) After 12 h the free parts of metal detach from the wafer. (c) Micrograph of the ground plane in aluminum (light color) on GaAs (darker color).*

Josephson Junctions:

- Spin-coat the wafer with 400 nm of copolymer MMA/PMMA and bake it at 180^o C for 5 min.
- Spin-coat a second PMMA layer of 400 nm and bake it at 180^o C for 5 min.
- Expose the designed pattern with a 100 kV electron beam, with a base dose of $700\ \frac{\mu C}{cm^2}$, with 2 nA current (without proximity error correction).
- Develop with a 1 : 1 solution of MIBK:IPA for 60 s
- Blow dry with a nitrogen gun.
- Ash away 30 nm of resist and possible organic residue with an Oxygen plasma generated at 50 W for 20 s.
- Load the wafer in the Plassys evaporator, and pump for 12 h.
- At the base pressure of $5{\cdot}10^{-8}$ mbar, deposit 50 nm of aluminum at 45^o with 1 nm/s rate (corresponding to 35 nm of metal thickness on the wafer).
- Oxidize the aluminum 2 mbar of 99.99% pure Oxygen for 20 min.
- Rotate the wafer 90^o around its axis.
- Deposit 110 nm of aluminum at 45^o with 1 nm/s rate (corresponding to 80 nm of metal thickness on the wafer).
- Oxidize the aluminum at 10 mbar of Oxygen for 10 min.
- Submerge the wafer in Remover1165 at 85^o C for 20 min, then leave it to lift-off for more than 12 hours.
- Pipette away the metal residue from lift-off.
- Insert the beaker containing the wafer in an ultrasonic bath at room temperature. Use low power ultrasound at 35 kHz in sweep mode for 3 mins.
- Repeat the previous step with a beaker with methanol and again with IPA.
- Blow dry the wafer with a nitrogen gun.

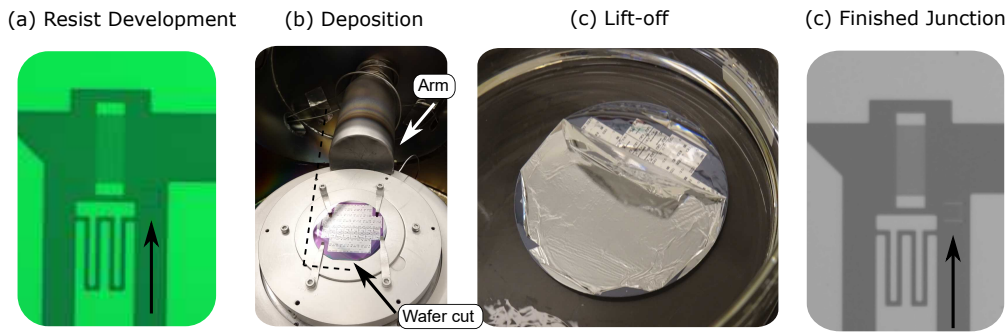

Figure C.7: *Third lithography step. (a) Optical micrograph of the SQUID geometry (indicated by the black arrow) exposed on the 800 nm thick resist. (b) The angle alignment for the junction depositions is performed placing the wafer cut perpendicular (or parallel) to plassys arm. (c) After 3 h the free parts of metal detach from the wafer. (d) The completed aluminum junction (pointed by the black arrow) on GaAs (darker color) .*

Patches:

- Spin-coat the wafer with 400 nm of copolymer MMA/PMMA and bake it at 180^o C for 5 min.
- Spin-coat a second PMMA layer of 400 nm and bake it at 180^o C for 5 min.
- Expose the designed pattern with a 100 kV electron beam, with a base dose of 700 $\frac{\mu C}{\text{cm}^2}$, with 2 nA current (without proximity error correction).
- Develop with a 1 : 1 solution of MIBK:IPA for 60 s
- Blow dry with a nitrogen gun.
- Ash away 30 nm of resist and possible organic residue with an oxygen plasma generated at 50 W for 20 s.
- Load the wafer in the Plassys evaporator, and pump for 12 h.
- At the base pressure of $5 \cdot 10^{-8}$ mbar, ion mill ca 15 nm of aluminum with 400 V and 20 mA for 1 min.
- Deposit 200 nm of aluminum with 1 nm/s rate while rotating around the wafer axis.
- Oxidize the aluminum at 10 mbar of oxygen for 10 min.
- Submerge the wafer in Remover1165 at 85^o C for 20 min, then leave it to lift-off for more than 12 hours.
- Pipette away the metal residue from lift-off.
- Insert the beaker containing the wafer in an ultrasonic bath at room temperature. Use low power ultrasound at 35 kHz in sweep mode for 3 mins.
- Repeat the previous step with a beaker with methanol and again with IPA.
- Blow dry the wafer with a nitrogen gun.

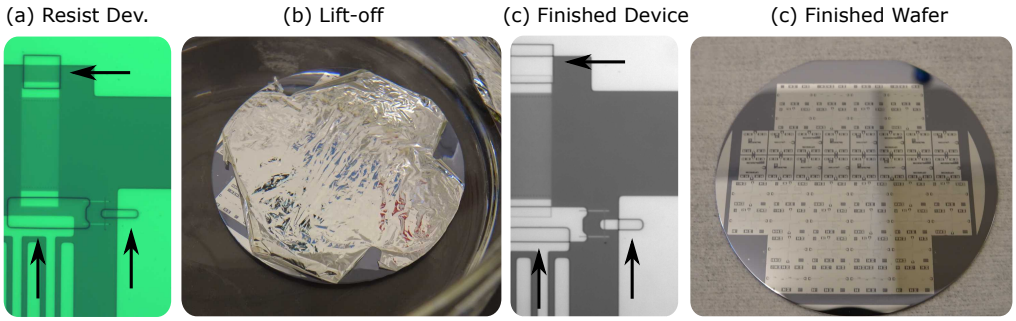

Figure C.8: *Forth lithography step. (a) Optical micrograph of the patches geometry (indicated by the black arrow) exposed on the 800 nm thick resist. (b) After 12 h the free parts of metal detach from the wafer. (c) The completed device with the added patches (pointed by the black arrow). (d) Final wafer.*

Cleaving:

- Spin S1805 resist at 3000 rpm for 60 s.
- Bake on a hot-plate at 115^{o} C for 5 min.
- Cleave with diamond tip scriber into $5 \times 7\,\mathrm{mm}^2$ chips.

In Figs. C.5, C.6, C.7 and C.8 we report the progress of this recipe.

C.4 Fabrication challenges

The fabrication of aluminum devices on gallium arsenide presents mainly two inconveniences compared to the one on silicon. On one hand, the contrast between aluminum and substrate, for electrons accelerated with 100 kV, is very small, making fail the automatic detection of marks in the Electron Beam Lithography (EBL) machine. On the other hand, the lower adhesion of the metal on gallium arsenide, make it difficult to realize IDT fingers with aspect ratios larger than 1000.

We realized test structures for the IDT geometry, that we tested with a parameter analyzer. The alignment during EBL exposure was realized "optically" with the SEM detector. In order to prevent deposition after a nonoptimal exposure, we measured the alignment error with a **Veriner scale** (see Fig. C.9).

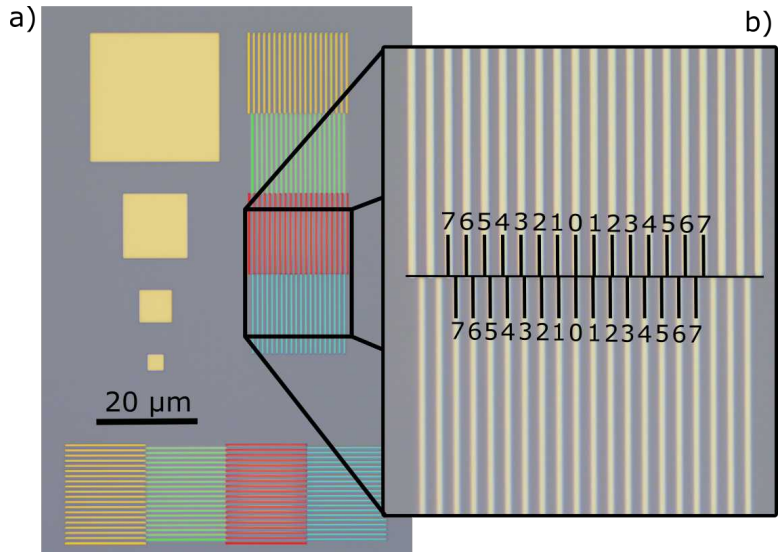

Figure C.9: *Micrograph of the Vernier marks used for measuring the alignment error in the four lithography steps (yellow, green, red, blue) of the fabrication on GaAs.*

The global error for a fabrication with four lithography steps, varied from 0.5 to 1 μm.

References

[1] F. Arute et al., "Quantum supremacy using a programmable superconducting processor", Nature **574**, 505–510 (2019).

[2] D. van Delft and P. Kes, "The discovery of superconductivity", Physics Today **63**, Publisher: American Institute of Physics, 38–43 (2010).

[3] E. Purcell, "Spontaneous emission probabilities at radio frequencies", Physical Review **69**, 681 (1946).

[4] S. Haroche and D. Kleppner, "Cavity quantum electrodynamics", Physics Today **42**, Publisher: American Institute of Physics, 24–30 (1989).

[5] A. Wallraff et al., "Strong coupling of a single photon to a superconducting qubit using circuit quantum electrodynamics", Nature **431**, 162–167 (2004).

[6] J. R. Waldram, *Superconductivity of metals and cuprates* (CRC Press, 1996).

[7] M. Tinkham, *Introduction to superconductivity* (McGraw Hill, 1996).

[8] A. Blais, A. L. Grimsmo, S. M. Girvin, and A. Wallraff, "Circuit quantum electrodynamics", Reviews of Modern Physics **93**, 025005 (2021).

[9] B. D. Josephson, "Possible new effects in superconductive tunnelling", Physics Letters **1**, 251–253 (1962).

[10] M. Pechal, "Microwave photonics in superconducting circuits", Doctoral Thesis (ETH Zurich, 2016).

[11] J. M. Martinis, M. H. Devoret, and J. Clarke, "Energy-level quantization in the zero-voltage state of a current-biased Josephson junction", Physical Review Letters **55**, 1543–1546 (1985).

[12] V. Bouchiat, D. Vion, P. Joyez, D. Esteve, and M. H. Devoret, "Quantum coherence with a single Cooper pair", Physica Scripta **1998** (1998).

[13] Y. Nakamura, Y. A. Pashkin, and J. S. Tsai, "Coherent control of macroscopic quantum states in a single-Cooper-pair box", Nature **398**, 786–788 (1999).

[14] K. W. Lehnert, K. Bladh, L. F. Spietz, D. Gunnarsson, D. I. Schuster, P. Delsing, and R. J. Schoelkopf, "Measurement of the excited-state lifetime of a microelectronic circuit", Physical Review Letters **90**, 027002 (2003).

[15] M. V. Gustafsson, T. Aref, A. F. Kockum, M. K. Ekström, G. Johansson, and P. Delsing, "Propagating phonons coupled to an artificial atom", Science **346**, 207–211 (2014).

[16] M. H. Devoret, "Quantum fluctuations in electrical circuits", Les Houches, ISBN 9780444825933, 351 (1997).

[17] S. M. Girvin, *Circuit QED: superconducting qubits coupled to microwave photons* (Oxford University Press, 2014).

[18] M. Peruzzo, A. Trioni, F. Hassani, M. Zemlicka, and J. M. Fink, "Surpassing the resistance quantum with a geometric superinductor", Physical Review Applied **14**, 044055 (2020).
[19] D. Niepce, J. Burnett, and J. Bylander, "High kinetic inductance nbn nanowire superinductors", Physical Review Applied **11**, 044014 (2019).
[20] N. A. Masluk, I. M. Pop, A. Kamal, Z. K. Minev, and M. H. Devoret, "Microwave characterization of Josephson junction arrays: implementing a low loss superinductance", Physical Review Letters **109**, 137002 (2012).
[21] C. K. Andersen and A. Blais, "Ultrastrong coupling dynamics with a transmon qubit", New Journal of Physics **19**, 023022 (2017).
[22] P. Arrangoiz-Arriola, E. A. Wollack, M. Pechal, J. D. Witmer, J. T. Hill, and A. H. Safavi-Naeini, "Coupling a superconducting quantum circuit to a phononic crystal defect cavity", Physical Review X **8**, 031007 (2018).
[23] A. D. Córcoles, E. Magesan, S. J. Srinivasan, A. W. Cross, M. Steffen, J. M. Gambetta, and J. M. Chow, "Demonstration of a quantum error detection code using a square lattice of four superconducting qubits", Nature Communications **6**, 6979 (2015).
[24] E. A. Sete, A. Q. Chen, R. Manenti, S. Kulshreshtha, and S. Poletto, "Floating Tunable Coupler for Scalable Quantum Computing Architectures", Physical Review Applied **15** (2021).
[25] J. Stehlik et al., "Tunable coupling architecture for fixed-frequency transmons", arXiv:2101.07746 [quant-ph] (2021).
[26] J. M. Martinis, S. Nam, J. Aumentado, and C. Urbina, "Rabi oscillations in a large Josephson-junction qubit", Physical Review Letters **89**, 117901 (2002).
[27] J. E. Mooij, T. P. Orlando, L. Levitov, L. Tian, C. H. v. d. Wal, and S. Lloyd, "Josephson persistent-current qubit", Science **285**, 1036–1039 (1999).
[28] J. Koch et al., "Charge-insensitive qubit design derived from the Cooper pair box", Physical Review A **76**, 042319 (2007).
[29] V. G. Veselago, "The electrodynamics of substances with simultaneously negative values of epsilon and mu", Soviet Physics Uspekhi **10**, 509–514 (1968).
[30] P. Lambropoulos, G. M. Nikolopoulos, T. R. Nielsen, and S. Bay, "Fundamental quantum optics in structured reservoirs", Reports on Progress in Physics **63**, 455–503 (2000).
[31] A. Lai, T. Itoh, and C. Caloz, "Composite right/left-handed transmission line metamaterials", IEEE Microwave Magazine **5**, 34–50 (2004).
[32] G. Andersson, B. Suri, L. Guo, T. Aref, and P. Delsing, "Non-exponential decay of a giant artificial atom", Nature Physics **15**, 1123–1127 (2019).
[33] G. S. MacCabe, H. Ren, J. Luo, J. D. Cohen, H. Zhou, A. Sipahigil, M. Mirhosseini, and O. Painter, "Phononic bandgap nano-acoustic cavity with ultralong phonon lifetime", Science **370**, 840–843 (2020).
[34] L. Rayleigh, "On waves propagated along the plane surface of an elastic solid", Proceedings of the London Mathematical Society **s1-17**, 4–11 (1885).
[35] D. M. Pozar, *Microwave engineering, 4th edition* (Wiley, 2011).

[36] J. M. Sage, V. Bolkhovsky, W. D. Oliver, B. Turek, and P. B. Welander, "Study of loss in superconducting coplanar waveguide resonators", Journal of Applied Physics **109**, 063915 (2011).
[37] M. Göppl et al., "Coplanar waveguide resonators for circuit quantum electrodynamics", Journal of Applied Physics **104**, 113904 (2008).
[38] A. Megrant et al., "Planar superconducting resonators with internal quality factors above one million", Applied Physics Letters **100**, 113510 (2012).
[39] C. M. Wilson, G. Johansson, A. Pourkabirian, M. Simoen, J. R. Johansson, T. Duty, F. Nori, and P. Delsing, "Observation of the dynamical Casimir effect in a superconducting circuit", Nature **479**, 376–379 (2011).
[40] I.-M. Svensson, A. Bengtsson, P. Krantz, J. Bylander, V. Shumeiko, and P. Delsing, "Period-tripling subharmonic oscillations in a driven superconducting resonator", Physical Review B **96**, 174503 (2017).
[41] M. Simoen, C. Chang, P. Krantz, J. Bylander, W. Wustmann, V. Shumeiko, P. Delsing, and C. Wilson, "Characterization of a multimode coplanar waveguide parametric amplifier", Journal of Applied Physics **118**, 154501 (2015).
[42] D. P. Morgan, *Surface acoustic wave filters: with applications to electronic communications and signal processing* (Academic Press, 2007).
[43] A. Perot and C. Fabry, "On the application of interference phenomena to the solution of various problems of spectroscopy and metrology", The Astrophysical Journal **9**, 87 (1899).
[44] R. Manenti, A. F. Kockum, A. Patterson, T. Behrle, J. Rahamim, G. Tancredi, F. Nori, and P. J. Leek, "Circuit quantum acoustodynamics with surface acoustic waves", Nature Communications **8**, 975 (2017).
[45] L. R. Sletten, B. A. Moores, J. J. Viennot, and K. W. Lehnert, "Resolving Phonon Fock States in a Multimode Cavity with a Double-Slit Qubit", Physical Review X **9** (2019).
[46] A. Noguchi, R. Yamazaki, Y. Tabuchi, and Y. Nakamura, "Single-photon quantum regime of artificial radiation pressure on a surface acoustic wave resonator", Nature Communications **11**, 1183 (2020).
[47] F. Bloch and A. Siegert, "Magnetic resonance for nonrotating fields", Physical Review **57**, 522–527 (1940).
[48] S. Haroche and J.-M. Raimond, *Exploring the quantum: atoms, cavities, and photons* (Oxford University Press, 2006).
[49] C. Gerry and P. Knight, *Introductory quantum optics* (Cambridge University Press, 2004).
[50] S. De Liberato, "Light-matter decoupling in the deep strong coupling regime: the breakdown of the Purcell effect", Physical Review Letters **112**, 016401 (2014).
[51] A. Frisk Kockum, A. Miranowicz, S. De Liberato, S. Savasta, and F. Nori, "Ultrastrong coupling between light and matter", Nature Reviews Physics **1**, 19–40 (2019).
[52] L. Morel, Z. Yao, P. Cladé, and S. Guellati-Khélifa, "Determination of the fine-structure constant with an accuracy of 81 parts per trillion", Nature **588**, 61–65 (2020).

[53] M. H. Devoret, S. Girvin, and R. Schoelkopf, "Circuit-QED: how strong can the coupling between a Josephson junction atom and a transmission line resonator be?", Annalen der Physik **16**, 767–779 (2007).
[54] I. I. Rabi, "Space quantization in a gyrating magnetic field", Physical Review **51**, 652–654 (1937).
[55] E. Jaynes and F. Cummings, "Comparison of quantum and semiclassical radiation theories with application to the beam maser", Proceedings of the IEEE **51**, 89–109 (1963).
[56] H.-P. Breuer, H.-P. Breuer, and F. Petruccione, *The theory of open quantum systems* (Oxford University Press, 2002).
[57] F. Binder, L. A. Correa, C. Gogolin, J. Anders, and G. Adesso, eds., *Thermodynamics in the quantum regime: fundamental aspects and new directions*, Fundamental Theories of Physics (Springer International Publishing, 2018).
[58] N. Cottet et al., "Observing a quantum Maxwell demon at work", Proceedings of the National Academy of Sciences **114**, 7561–7564 (2017).
[59] A. Ronzani, B. Karimi, J. Senior, Y.-C. Chang, J. T. Peltonen, C. Chen, and J. P. Pekola, "Tunable photonic heat transport in a quantum heat valve", Nature Physics **14**, 991–995 (2018).
[60] A. P. M. Place et al., "New material platform for superconducting transmon qubits with coherence times exceeding 0.3 milliseconds", Nature Communications **12**, 1779 (2021).
[61] R. Barends et al., "Minimizing quasiparticle generation from stray infrared light in superconducting quantum circuits", Applied Physics Letters **99**, 113507 (2011).
[62] R.-P. Riwar, A. Hosseinkhani, L. D. Burkhart, Y. Y. Gao, R. J. Schoelkopf, L. I. Glazman, and G. Catelani, "Normal-metal quasiparticle traps for superconducting qubits", Physical Review B **94**, 104516 (2016).
[63] S. Gustavsson et al., "Suppressing relaxation in superconducting qubits by quasiparticle pumping", Science **354**, 1573–1577 (2016).
[64] J.-H. Yeh, J. LeFebvre, S. Premaratne, F. C. Wellstood, and B. S. Palmer, "Microwave attenuators for use with quantum devices below 100 mK", Journal of Applied Physics **121**, 224501 (2017).
[65] E. M. Purcell, H. C. Torrey, and R. V. Pound, "Resonance absorption by nuclear magnetic moments in a solid", Physical Review **69**, 37–38 (1946).
[66] E. A. Sete, J. M. Martinis, and A. N. Korotkov, "Quantum theory of a bandpass Purcell filter for qubit readout", Physical Review A **92**, 012325 (2015).
[67] D. C. McKay, R. Naik, P. Reinhold, L. S. Bishop, and D. I. Schuster, "High-contrast qubit interactions using multimode cavity QED", Physical Review Letters **114**, 080501 (2015).
[68] J. Lisenfeld, G. J. Grabovskij, C. Müller, J. H. Cole, G. Weiss, and A. V. Ustinov, "Observation of directly interacting coherent two-level systems in an amorphous material", Nature Communications **6**, 6182 (2015).
[69] A. Bilmes, A. Megrant, P. Klimov, G. Weiss, J. M. Martinis, A. V. Ustinov, and J. Lisenfeld, "Resolving the positions of defects in superconducting quantum bits", Scientific Reports **10**, 3090 (2020).

[70] M. R. Vissers, J. Gao, D. S. Wisbey, D. A. Hite, C. C. Tsuei, A. D. Corcoles, M. Steffen, and D. P. Pappas, "Low loss superconducting titanium nitride coplanar waveguide resonators", Applied Physics Letters **97**, 232509 (2010).
[71] J. M. Sage, V. Bolkhovsky, W. D. Oliver, B. Turek, and P. B. Welander, "Study of loss in superconducting coplanar waveguide resonators", Journal of Applied Physics **109**, 063915 (2011).
[72] J. Burnett, L. Faoro, and T. Lindström, "Analysis of high quality superconducting resonators: consequences for TLS properties in amorphous oxides", Superconductor Science and Technology **29**, 044008 (2016).
[73] H. Wang et al., "Improving the coherence time of superconducting coplanar resonators", Applied Physics Letters **95**, 233508 (2009).
[74] A. Dunsworth et al., "Characterization and reduction of capacitive loss induced by sub-micron Josephson junction fabrication in superconducting qubits", Applied Physics Letters **111**, 022601 (2017).
[75] A. D. O'Connell et al., "Microwave dielectric loss at single photon energies and millikelvin temperatures", Applied Physics Letters **92**, 112903 (2008).
[76] J. Burnett et al., "Evidence for interacting two-level systems from the 1/f noise of a superconducting resonator", Nature Communications **5**, 4119 (2014).
[77] C. Müller, J. Lisenfeld, A. Shnirman, and S. Poletto, "Interacting two-level defects as sources of fluctuating high-frequency noise in superconducting circuits", Physical Review B **92**, 035442 (2015).
[78] P. Klimov et al., "Fluctuations of energy-relaxation times in superconducting qubits", Physical Review Letters **121**, 090502 (2018).
[79] C. M. Van Vliet and P. H. Handel, "A new transform theorem for stochastic processes with special application to counting statistics", Physica A: Statistical Mechanics and its Applications **113**, 261–276 (1982).
[80] C. Müller, J. H. Cole, and J. Lisenfeld, "Towards understanding two-level-systems in amorphous solids: insights from quantum circuits", Reports on Progress in Physics **82**, 124501 (2019).
[81] N. Kirsh, E. Svetitsky, A. L. Burin, M. Schechter, and N. Katz, "Revealing the nonlinear response of a tunneling two-level system ensemble using coupled modes", Physical Review Materials **1**, 012601 (2017).
[82] J. F. Nye, *Physical properties of crystals: their representation by tensors and matrices* (Oxford University Press, Oxford, New York, May 16, 1985).
[83] A. Arnau and D. Soares, "Fundamentals of piezoelectricity", in *Piezoelectric transducers and applications*, edited by A. A. Vives (Springer, Berlin, Heidelberg, 2008).
[84] A. A. Oliner, ed., *Acoustic surface waves*, Topics in Applied Physics (Springer-Verlag, Berlin Heidelberg, 1978).
[85] G. Andersson, "Quantum acoustics with superconducting circuits", PhD thesis (Chalmers University of Technology, 2020).
[86] C. Maruccio, M. Scigliuzzo, S. Rizzato, P. Scarlino, G. Quaranta, M. S. Chiriaco, A. G. Monteduro, and G. Maruccio, "Frequency and time domain analysis of surface acoustic wave propagation on a piezoelectric gallium arsenide substrate:

a computational insight", Journal of Intelligent Material Systems and Structures **30**, 801–812 (2019).
[87] Y. Liu and A. A. Houck, "Quantum electrodynamics near a photonic bandgap", Nature Physics **13**, 48–52 (2017).
[88] V. S. Ferreira, J. Banker, A. Sipahigil, M. H. Matheny, A. J. Keller, E. Kim, M. Mirhosseini, and O. Painter, "Collapse and Revival of an Artificial Atom Coupled to a Structured Photonic Reservoir", arXiv:2001.03240 (2020).
[89] H. Wang et al., "Mode structure in superconducting metamaterial transmission-line resonators", Physical Review Applied **11**, 054062 (2019).
[90] N. M. Sundaresan, R. Lundgren, G. Zhu, A. V. Gorshkov, and A. A. Houck, "Interacting Qubit-Photon Bound States with Superconducting Circuits", Physical Review X **9**, 011021 (2019).
[91] M. Mirhosseini, E. Kim, V. S. Ferreira, M. Kalaee, A. Sipahigil, A. J. Keller, and O. Painter, "Superconducting metamaterials for waveguide quantum electrodynamics", Nature communications **9**, 1–7 (2018).
[92] E. Kim et al., "Quantum electrodynamics in a topological waveguide", Physical Review X **11**, 011015 (2021).
[93] I. S. Besedin et al., "Topological excitations and bound photon pairs in a superconducting quantum metamaterial", Physical Review B **103**, 224520 (2021).
[94] S. John, "Strong localization of photons in certain disordered dielectric superlattices", Physical Review Letters **58**, 2486–2489 (1987).
[95] G. Calajó, F. Ciccarello, D. Chang, and P. Rabl, "Atom-field dressed states in slow-light waveguide QED", Phys. Rev. A **93**, 033833 (2016).
[96] S. John and J. Wang, "Quantum electrodynamics near a photonic band gap: photon bound states and dressed atoms", Physical Review Letters **64**, 2418–2421 (1990).
[97] P. Longo, P. Schmitteckert, and K. Busch, "Few-Photon Transport in Low-Dimensional Systems: Interaction-Induced Radiation Trapping", Phys. Rev. Lett. **104** (2010).
[98] S. Krinner et al., "Engineering cryogenic setups for 100-qubit scale superconducting circuit systems", EPJ Quantum Technology **6**, 1–29 (2019).
[99] S. W. Van Sciver, *Helium cryogenics* (Springer Science & Business Media, 2012).
[100] J. Wenner et al., "Wirebond crosstalk and cavity modes in large chip mounts for superconducting qubits", Superconductor Science and Technology **24**, 065001 (2011).
[101] A. Bengtsson, "Quantum information processing with tunable and low-loss superconducting circuits", PhD thesis (Chalmers University of Technology, 2020).
[102] M. A. Nielsen and I. Chuang, *Quantum computation and quantum information* (Cambridge University PressF, 2002).
[103] E. Jeffrey et al., "Fast accurate state measurement with superconducting qubits", Physical Review Letters **112**, 190504 (2014).
[104] A. Blais, R.-S. Huang, A. Wallraff, S. M. Girvin, and R. J. Schoelkopf, "Cavity quantum electrodynamics for superconducting electrical circuits: an architecture for quantum computation", Physical Review A **69**, 062320 (2004).

[105] S. Sheldon, L. S. Bishop, E. Magesan, S. Filipp, J. M. Chow, and J. M. Gambetta, "Characterizing errors on qubit operations via iterative randomized benchmarking", Physical Review A **93**, 012301 (2016).
[106] Z. Chen et al., "Measuring and suppressing quantum state leakage in a superconducting qubit", Physical Review Letters **116**, 020501 (2016).
[107] P. Krantz et al., "Investigation of nonlinear effects in Josephson parametric oscillators used in circuit quantum electrodynamics", New Journal of Physics **15**, 105002 (2013).
[108] X. Y. Jin et al., "Thermal and residual excited-state population in a 3d transmon qubit", Physical Review Letters **114**, 240501 (2015).
[109] V. Ambegaokar and A. Baratoff, "Tunneling between superconductors", Physical Review Letters **10**, 486–489 (1963).
[110] V. Ambegaokar and A. Baratoff, "Tunneling between superconductors (erratum)", Physical Review Letters **11**, 104 (1963).
[111] W. Kern, "The evolution of silicon wafer cleaning technology", Journal of The Electrochemical Society **137**, 1887 (1990).